**Title**

The architecture of the mouse trigeminal-facial brainstem : disynaptic circuitry, genomic organization, and follicle mechanics

**Permalink**

https://escholarship.org/uc/item/0vf6x967

**Authors**

Matthews, David William
Matthews, David William

**Publication Date**

2012

Peer reviewed|Thesis/dissertation

UNIVERSITY OF CALIFORNIA, SAN DIEGO

# The architecture of the mouse trigeminal-facial brainstem: Disynaptic circuitry, genomic organization, and follicle mechanics

A dissertation submitted in partial satisfaction of the
requirements for the degree
Doctor of Philosophy

in

Neurosciences
Specialization in Computational Neurosciences

by

David W. Matthews

Committee in charge:

Professor Charles F. Stevens, Chair
Professor David Kleinfeld, Co-Chair
Professor Edward M. Callaway
Professor Harvey J. Karten
Professor Terry J. Sejnowski

2012

The dissertation of David W. Matthews is approved, and it is acceptable in quality and form for publication on microfilm and electronically:

Co-Chair

Chair

University of California, San Diego

2012

# TABLE OF CONTENTS

Signature Page . . . . . iii

Table of Contents . . . . . iv

List of Figures . . . . . vii

List of Tables . . . . . ix

Acknowledgements . . . . . x

Vita . . . . . xii

Abstract of the Dissertation . . . . . xiii

Chapter 1 Introduction . . . . . 1

Chapter 2 An excitatory, disynaptic brainstem pathway for sensorimotor feedback in the control of whisking . . . . . 6
- 2.1 Abstract . . . . . 7
- 2.2 Introduction . . . . . 7
- 2.3 Methods . . . . . 9
  - 2.3.1 Animals . . . . . 9
  - 2.3.2 Stereotaxic injections of tracers and viruses . . . . . 9
  - 2.3.3 Perfusion and immunohistochemistry . . . . . 11
  - 2.3.4 *In situ* hybridization . . . . . 13
  - 2.3.5 Imaging and digitization . . . . . 13
- 2.4 Results . . . . . 14
  - 2.4.1 Morphological evidence for a partitioning zone in spinal trigeminal brainstem . . . . . 14
  - 2.4.2 Sensory afferents in SpVmu and surrounding nuclei . 16
  - 2.4.3 Premotor neurons in SpVmu and surrounding nuclei 20
  - 2.4.4 Monosynaptic connectivity of TG afferents to VIIm-projecting SpVmu interneurons . . . . . 30
  - 2.4.5 Neurochemical content of VIIm-projecting SpVmu interneurons . . . . . 36
- 2.5 Discussion . . . . . 38
  - 2.5.1 Trigeminal circuitry . . . . . 38
    - 2.5.1.1 Implications of label intensity . . . . . 38
    - 2.5.1.2 Comparison with substantia gelatinosa . . 40
    - 2.5.1.3 Organization of peripheral endings . . . . 40
    - 2.5.1.4 Relationship to blepharospasm . . . . . 40
    - 2.5.1.5 Physiology of the Vg-SpVmu-VIIm circuit 41

2.5.2 Virus-based anatomy for behavior and physiology . . 42
2.5.3 Computational considerations . . . . . . . . . . . . 42

Chapter 3 The genomic organization of trigeminal brainstem using a histological atlas and statistical learning . . . . . . . . . . . . . . . . . . 44
3.1 Abstract . . . . . . . . . . . . . . . . . . . . . . . . . . 45
3.2 Introduction . . . . . . . . . . . . . . . . . . . . . . . . 45
3.3 Methods . . . . . . . . . . . . . . . . . . . . . . . . . . 48
3.3.1 Gene expression data from Allen Brain Atlas . . . . 49
3.3.2 Development of histological data . . . . . . . . . . . 49
3.3.3 Imaging and digitization . . . . . . . . . . . . . . . 52
3.3.4 Co-registration of histological data with Allen Brain Atlas . . . . . . . . . . . . . . . . . . . . . . . 53
3.4 Results . . . . . . . . . . . . . . . . . . . . . . . . . . . 57
3.4.1 Projection versus regional gene expression . . . . . 57
3.4.1.1 Principal components analysis of brainstem and trigeminal EEMs . . . . . . . . . . . 57
3.4.1.2 Non-negative matrix factorization of trigeminal EEM . . . . . . . . . . . . . . . . . . 58
3.4.1.3 Highly explanatory genes from unsupervised learning methods . . . . . . . . . . 59
3.4.2 A sparse genetic code may underlie trigeminal organization . . . . . . . . . . . . . . . . . . . . . . . 60
3.4.2.1 Decision tree learning with individual genes 60
3.4.2.2 Feature selection using conservative criteria 61
3.4.2.3 Classification of nuclei by decision tree learning . . . . . . . . . . . . . . . . . . . . . 62
3.4.2.4 Classification of terminal regions by decision tree learning . . . . . . . . . . . . . . 63
3.4.3 Independent validation: GENSAT BAC image database 64
3.5 Discussion . . . . . . . . . . . . . . . . . . . . . . . . . 65
3.5.1 Trigeminal projection database . . . . . . . . . . . 65
3.5.2 Statistical considerations . . . . . . . . . . . . . . . 67
3.5.2.1 Quantification with amplified, non-isotopic ISH and probe quality . . . . . . . . . . . 67
3.5.2.2 Problems in high dimensions . . . . . . . 68
3.5.3 Future directions . . . . . . . . . . . . . . . . . . . 70

Chapter 4 Imaging the mechanics of follicle receptors with two photon microscopy . . . . . . . . . . . . . . . . . . . . . . . . . . 83
4.1 Abstract . . . . . . . . . . . . . . . . . . . . . . . . . . 84
4.2 Introduction . . . . . . . . . . . . . . . . . . . . . . . . 84
4.3 Methods . . . . . . . . . . . . . . . . . . . . . . . . . . 86

    - 4.3.1 Surgical extraction and preparation of follicle . . . . 86
    - 4.3.2 Imaging and analysis . . . . . . . . . . . . . . . . . 87
  - 4.4 Results . . . . . . . . . . . . . . . . . . . . . . . . . 89
    - 4.4.1 Follicle imaging . . . . . . . . . . . . . . . . . . . 89
    - 4.4.2 Vibrissa displacement effects receptor location . . . 92
  - 4.5 Discussion and Future Directions . . . . . . . . . . . . . . 96

Chapter 5 Conclusion . . . . . . . . . . . . . . . . . . . . . . . . . 99

Appendix A Automatic identification of fluorescently labeled brain cells for rapid functional imaging . . . . . . . . . . . . . . . . . . . . . . . 101
  - A.1 Abstract . . . . . . . . . . . . . . . . . . . . . . . . . . 102
  - A.2 Introduction . . . . . . . . . . . . . . . . . . . . . . . . 102
  - A.3 Methods . . . . . . . . . . . . . . . . . . . . . . . . . . 103
    - A.3.1 Experimental methods . . . . . . . . . . . . . . . . . 103
      - A.3.1.1 Animal preparation . . . . . . . . . . . . . 103
      - A.3.1.2 Somatosensory cortex mapping . . . . . . 104
      - A.3.1.3 Calcium dye injection and imaging . . . . 105
    - A.3.2 Computational methods . . . . . . . . . . . . . . . . 105
      - A.3.2.1 Implementation of the cell segmentation algorithm . . . . . . . . . . . . . . . . . . 105
      - A.3.2.2 Optimized Scan Algorithm . . . . . . . . 107
      - A.3.2.3 Scan Path Considerations . . . . . . . . . 108
  - A.4 Results . . . . . . . . . . . . . . . . . . . . . . . . . . . 111
    - A.4.1 Implementation . . . . . . . . . . . . . . . . . . . . 111
    - A.4.2 Application . . . . . . . . . . . . . . . . . . . . . . 115
  - A.5 Discussion . . . . . . . . . . . . . . . . . . . . . . . . . 121

Appendix B Table of abbreviations . . . . . . . . . . . . . . . . . . . 123

Bibliography . . . . . . . . . . . . . . . . . . . . . . . . . . . . . 127

# LIST OF FIGURES

Figure 2.1: *Schematic and spatial arrangement of trigeminal nuclei.* . . . . . . 17
Figure 2.2: *Morphology of spinal trigeminal brainstem.* . . . . . . . . . . . . . 18
Figure 2.3: *Sensory afferent projections to trigeminal nuclei after ganglion injection with CTb.* . . . . . . . . . . . . . . . . . . . . . . . . . 19
Figure 2.4: *Sensory afferents terminate locally in SpVmu after vibrissa pad injection with CTb.* . . . . . . . . . . . . . . . . . . . . . . . . . 21
Figure 2.5: *Volumetric reconstruction of sensory afferent terminal zones following focal vibrissa pad injection.* . . . . . . . . . . . . . . . . . . . 22
Figure 2.6: *Central afferents to SpVmu originate only from the maxillary branch.* 23
Figure 2.7: *Retrograde labeling by pseudorabies virus.* . . . . . . . . . . . . . 24
Figure 2.8: *Timing of transsynaptic transduction of pseudorabies-infected neurons.* . . . . . . . . . . . . . . . . . . . . . . . . . . . . . . . . 25
Figure 2.9: *Retrograde transport of PRV from VIIm robustly labels SpVmu neurons.* . . . . . . . . . . . . . . . . . . . . . . . . . . . . . . . . 27
Figure 2.10: *Comparison of retrogradely labeled SpVmu and non-SpVmu neurons.* 28
Figure 2.11: *Retrograde transport of fluorogold from VIIm labels SpVmu neurons.* 29
Figure 2.12: *Monosynaptic labeling strategy using modified rabies in a transgenic animal.* . . . . . . . . . . . . . . . . . . . . . . . . . . . . 31
Figure 2.13: *Modified rabies labeling of premotor neurons in SpVmu.* . . . . . . 32
Figure 2.14: *Strategy for dual labeling of primary afferents and VIIm-projecting cells in SpVmu.* . . . . . . . . . . . . . . . . . . . . . . . . . . . 34
Figure 2.15: *Dual labeling of primary afferents and VIIm-projecting cells in SpVmu.* 35
Figure 2.16: *Combined WGA-Cre and Flex virus labeling of SpVmu neurons.* . . . 37
Figure 2.17: In situ *hybridization of retrogradely labeled SpVmu neurons.* . . . . . 39

Figure 3.1: *Expression energy matrix and voxel representation.* . . . . . . . . . 50
Figure 3.2: *Semi-automatic tracing in Neurolucida.* . . . . . . . . . . . . . . . 54
Figure 3.3: *Reconstructed volumes of trigeminal branch afferents.* . . . . . . . 55
Figure 3.4: *Semi-automatic co-registration with Allen database.* . . . . . . . . . 56
Figure 3.5: *Trigeminal nuclei-based clustering of brainstem voxels in principal component space.* . . . . . . . . . . . . . . . . . . . . . . . . . . . 72
Figure 3.6: *Trigeminal projection-based clustering of brainstem voxels in principal component space.* . . . . . . . . . . . . . . . . . . . . . . . 73
Figure 3.7: *Similarity index for trigeminal brainstem groups.* . . . . . . . . . . 74
Figure 3.8: *Non-negative matrix factorization of trigeminal EEM* . . . . . . . . 75
Figure 3.9: *Gene contributions from dominant basis vectors of NMF and PCA.* 76
Figure 3.10: *Feature selection by preprocessing metrics* . . . . . . . . . . . . 77
Figure 3.11: *Visualized decision trees for membership in trigeminal nuclei* . . . 78
Figure 3.12: *Sample gene expression from training on nuclei:* Hoxa5 . . . . . . 79
Figure 3.13: *Schematic decision trees of the three trigeminal branch inputs.* . . . 80

Figure 3.14: *Classification performance for maxillary decision tree superimposed on the voxelized brain.* . . . . . . . . . . . . . . . . . . . . . . . . . 81
Figure 3.15: *Comparison with BAC database.* . . . . . . . . . . . . . . . . . . . . 82

Figure 4.1: *Schematic of follicle preparation for two photon imaging.* . . . . . . 88
Figure 4.2: *Global registration of DAPI-labeled bodies across follicle experiments.* . . . . . . . . . . . . . . . . . . . . . . . . . . . . . . 90
Figure 4.3: *Bleaching of 5-hexadecanoylamino-fluorescein.* . . . . . . . . . . . . 91
Figure 4.4: *Labeled follicle receptors in PvCre-TdTomato and TN-XXL mouse lines.* . . . . . . . . . . . . . . . . . . . . . . . . . . . . . . . . 93
Figure 4.5: *FM1-43 and DAPI label many receptors in the follicle.* . . . . . . . . 94
Figure 4.6: *Axial displacement of vibrissa.* . . . . . . . . . . . . . . . . . . . . . 95
Figure 4.7: *Rostral and caudal displacement of vibrissa.* . . . . . . . . . . . . . 96

Figure A.1: *Illustration of line scan speeds and error in the measurement of blood flow.* . . . . . . . . . . . . . . . . . . . . . . . . . . . . . 110
Figure A.2: *Feature map of time-series image data* . . . . . . . . . . . . . . . . 112
Figure A.3: *Feature map of intermediate cluster data* . . . . . . . . . . . . . . 113
Figure A.4: *Examples of annotations used to generate the two classifiers.* . . . . 114
Figure A.5: *Example of segmentation of a test data set.* . . . . . . . . . . . . . 116
Figure A.6: *Validation statistics for the classifiers.* . . . . . . . . . . . . . . . . 117
Figure A.7: *Illustration of cell bodies identified using a single classifier.* . . . . 119
Figure A.8: *Two examples of cell segmentation and fast scanning for functional imaging of neurons and astrocytes in rat parietal cortex* . . . . . . 120

# LIST OF TABLES

Table 2.1: *Virus-based and traditional labeling strategies employed*. . . . . . . 15

# ACKNOWLEDGEMENTS

It is my honor to thank the many people who have helped to make this dissertation a reality.

I am grateful to Dr. David Kleinfeld, my Ph.D. supervisor, for his generous support of my research. His emphasis on making the highest quality measurements has helped to shape me into the scientist I am today. He provided me with great latitude to pursue varied and risky projects; I report here only a fraction of the techniques I learned, developed, and used in his exceptionally diverse lab.

I also thank Dr. Harvey Karten, whose breadth of neuroanatomical knowledge and enthusiasm for extending the technologies available to neuroanatomy helped to inspire much of my work.

I am indebted to my thesis committee members, Dr. Chuck Stevens, Dr. Ed Callaway, and Dr. Terry Sejnowski, for their encouragement, vision, and advice as I traversed risky scientific paths.

The unique and broad community of computational neuroscientists at UCSD and the Salk both resulted in and was fostered by the Computational Neurobiology Ph.D. Program, which recruited me to pursue my dissertation here. I am grateful to Drs. E.J. Chichilnisky, Bill Kristan, and Terry Sejnowski for their vision in creating and sustaining one of the strongest computational neuroscience centers in the world.

I am humbled to have worked closely and argued heatedly with many talented scientists and thinkers during my time in the laboratory; in particular, I thank Pablo Blinder, John Curtis, Jonathan Driscoll, Dan Hill, Per Knutsen, Céline Matéo, Ben Migliori, Jeff Moore, Quoc Nguyen, Lee Schroeder, Al Schweitzer, Andy Shih, and Phil Tsai.

To my many friends and colleagues in San Diego and beyond, too numerous to name, I thank you.

Last, I acknowledge my parents, Dr. Ronald Matthews and Pamela Matthews, for instilling in me an insatiable curiosity and a deep desire to excel; my brother, Andrew Matthews, for our shared weltanschauung; and all three, along with my grandmother, Elva Matthews, for their unconditional love and support.

Chapter 2, in full, is a manuscript in preparation for submission. The dissertation author is the first author of this paper; though the full co-authorships have not yet been determined, they will likely include Takahiro Furuta, Fan Wang, Martin Deschênes, Harvey J. Karten, and David Kleinfeld.

Chapter 3, in part, is a manuscript in preparation for likely submission. The dissertation author will be the first author of this paper; though the full co-authorships have not yet been determined, they will include Harvey J. Karten, and David Kleinfeld.

Chapter 4, in part, is a manuscript in preparation for likely submission. The dissertation author will be a first author of this paper; though the full co-authorships have not yet been determined, they will include Samuel Whiteley, Per M. Knutsen, and David Kleinfeld.

Appendix chapter A, in full, is a reprint of the material as it appears in The Journal of Neurophysiology, 104 (3), 1803-1811, Valmianski, I.; Shih, A.Y.; Driscoll, J.D.; Matthews, D.W.; Freund, Y.; & Kleinfeld, D. (2010). The dissertation author was a coauthor of this paper.

# VITA

| | |
|---|---|
| 2012 | Ph.D., Neurosciences, Specialization in Computational Neuroscience<br>University of California, San Diego |
| 2005-2008 | National Science Foundation Graduate Research Fellow |
| 2007-2008 | NSF Center for Theoretical Biological Physics Fellow |
| 2005 | A.B. Molecular Biology *cum laude*, Certificates in Neuroscience and Biological Engineering<br>Princeton University |
| 2004 | Howard Hughes Medical Institute Summer Research Fellow |
| 2003 | National Science Foundation Summer Research Fellow |

ABSTRACT OF THE DISSERTATION

# The architecture of the mouse trigeminal-facial brainstem: Disynaptic circuitry, genomic organization, and follicle mechanics

by

David W. Matthews

Doctor of Philosophy in Neurosciences
Specialization in Computational Neurosciences

University of California, San Diego, 2012

Professor Charles F. Stevens, Chair
Professor David Kleinfeld, Co-Chair

Neural circuits are the fundamental substrate for brain computations and, ultimately, behavior. The sensorimotor processing that mediates sensory-driven behaviors relies on inputs from the environment, transduced by specialized receptors, and transformations of these inputs into motor outputs, constrained by circuit architecture. The trigeminal-facial brainstem system, which exercises the lowest level of control over vibrissa behavior, provides an ideal framework for understanding the neural circuitry underlying sensorimotor processing. While the anatomy of trigeminal inputs and facial outputs has been studied for over a century, the organization of circuits instantiating such processing remains obscure. Here, I explore this organization with three related studies on mouse trigeminal and facial brainstem circuitry. First, I delineate a complete disynaptic circuit from mechanosensory trigeminal inputs to facial motor outputs using single and dual labeling with traditional tracers, engineered viruses, and transgenic animals. I show that a morphologically distinct set of interneurons receives monosynaptic inputs from peripheral trigeminal afferents, and projects monosynaptically to the division of facial nucleus controlling vibrissa movement. These interneurons are primarily glutamatergic, suggesting that this circuit may mediate the fast, positive feedback employed in vibrissa-based active sensation. Second, I examine the large scale genetic organization of inputs and nuclei within the trigeminal brainstem. Using targeted microinjections to the face, I generate a micrometer-resolution inventory of central trigeminal afferent projections. I develop a method to register this inventory with a genome-wide gene expression database of the mouse brain. With these co-registered datasets, I use statistical learning approaches to explore both the relationship between connectivity and regionalization and the role of sparse sets of genes in determining trigeminal organization. Finally, I evaluate the specialized receptors that encode vibrissa sensory information. I develop a preparation for two photon imaging of sensory endings, then characterize the reliable mechanical deformations of different receptor types that result from vibrissa deflections. Altogether, this work provides novel insights into the architecture of low level sensorimotor processing, from peripheral sensory transduction, through individual circuits, to overarching organization.

# Chapter 1

# Introduction

One of the grand challenges of neuroscience is to understand the connectivity of the brain. To contextualize the electrochemical information flowing between neurons, we must understand the precise architecture of the underlying physical substrate. While the analysis of neuronal structural began well over a century ago [Golgi, 1873, Ramon y Cajal, 1905], it is currently experiencing a renaissance, due to the development of novel imaging technologies, targeted molecular and viral techniques, and scalable computational resources. This dissertation is motivated by my conviction that the principles of neuronal connectivity subserve and constrain the algorithms available for computation, and are therefore essential to understanding how the brain works.

In pursuit of understanding the organization of neural circuitry, I have focused on the mouse trigeminal-facial brainstem that underlies the control of vibrissae, the mobile whiskers of the face. Briefly, sensory receptors that transduce touch, positioned in vibrissa follicles, are connected to the trigeminal brainstem nuclei by sensory afferents coursing through the fifth cranial nerve. Trigeminal neurons project directly and indirectly to the facial nucleus, whose motoneurons send efferents to the musculature controlling vibrissa position. This system provides an ideal framework for many levels of anatomical investigation, due to (1) the diversity and spatial segregation of its inputs and outputs, (2) the known interconnectivity of its nuclei, (3) its use as a model system for developmental genetics, and (4) the large volume of murine brainstem that it occupies. Additionally, the system is amenable to a broad range of techniques that we employ here, including each of the tools listed above and responsible for restoring interest in brain architecture.

Here, I focus on three related studies of trigeminal-facial anatomy, at the levels of input-output circuitry in small sets of neurons, large scale connectivity of nuclei and afferent bundles, and receptor mechanics in the follicle.

One of the primary circuit architectures employed by neural systems involves hierarchical synaptic loops that connect sensory receptors to muscle outputs. Strong selective pressure for fast, context-relevant behavior suggests that circuits minimize the number of synapses necessary to respond to stimuli in the environment. In the vibrissa system, contact with a stimulus increases the amplitude of subsequent movement of the vibrissa with very short latency [Sachdev et al., 2003, Nguyen and Kleinfeld, 2005], suggesting that an excitatory feedback loop underlies low level control from the sensory to the motor system. In chapter 2, I describe experiments that reveal the putative circuit for this sensorimotor behavior. We apply traditional tracers to identify the discrete sets of neurons and terminals involved in transmitting the sensory signal and conveying the motor output. We then use molecular and viral methods to characterize the disynaptic connectivity between these sensory afferents and motoneuron efferents, and find that the interneurons in the circuit are primarily excitatory.

Identifying the structure of synaptic loops is important for constraining possible circuit computations and for establishing the underlying substrates for behavior. But because the brain is replete with such putative loops, larger scale informatics approaches can serve as a powerful complementary tool to determine the organizational principles that govern regionalization, the grouping of many neurons into functional sets, and connectivity, the projections among these groups of neurons. Critical data for this strategy include the local expression of genes. Gene products generate gradients and local cues important for axon guidance and synapse formation [Polleux et al., 2007, Chédotal and Richards, 2010], and transcription factors and morphogens prompt neuronal and regional differentiation [Bishop, 2000, Inan and Crair, 2007]. The recent introduction of genome-wide, spatially-registered genetic expression atlases of the mouse brain [Richardson et al., 2010, Lein et al., 2007] provide an unprecedented opportunity to evaluate brain organization; however, to put gene expression patterns in the context of neural circuitry, the production of similarly large scale data on regional connectivity is necessary. Currently, no connectivity databases exist at the spatial scale of available genomics atlases. I address this paucity of connectivity data and analyze the genomic architecture of trigeminal brainstem in chapter 3. To solve the problem of connectivity data, we generate a histological library of the projections from sensory afferents of the face to distinct central terminal zones in the trigeminal brainstem. To compare trigeminal connectivity data with genetic expression profiles, we develop a method for co-registering the two databases, then use statistical learning approaches to evaluate the genetic parcellation of the trigeminal brainstem and to identify candidate genes or gene sets that strongly influence organization.

From individual disynaptic circuits to large scale afferent projections, inputs matter to the trigeminal brainstem. The macroscopic organization of central trigeminal afferents determines which sensory signals are available for local modulation within trigeminal nuclei, further processing via trigemino-thalamic and other efferent connections, filtering by cortical and subcortical centers, and feedback with relevant motor systems [Kleinfeld et al., 1999]. But the nature of the signals processed within and beyond brainstem are dictated by the repertoire of stimulus responses generated by the peripheral sensory organs, particularly the vibrissa follicle. The microanatomy of the vibrissa follicle has been studied extensively with traditional histological techniques (e.g. [Rice et al., 1993, Rice et al., 1997]). Additionally, the mechanical properties of vibrissae [Hartmann et al., 2003, Neimark et al., 2003] and the range of variables encoded by primary afferents [Lichtenstein et al., 1990, Jones et al., 2004, Khatri et al., 2009] have been explored. However, the relationship between the morphological specializations of follicle receptors and the movement of a vibrissa is not known. The key challenge to understanding this relationship is the fact that an optically and physically dense protective capsule ensheathes follicle receptors, which prevents traditional imaging and electrophysiology methods. Therefore, in chapter 4, I introduce a novel surgical preparation that allows for two photon imaging of the movements of sensory receptors in the intact follicle. I present results on receptor class-specific and global receptor movements in response to behaviorally-matched deflections of the vibrissa. Though still preliminary, this preparation of the intact follicle is likely to be fruitful both anatomically and physiologically.

Finally, one of the projects on which I worked extensively, though do not present in this dissertation, involved two photon imaging of calcium transients in trigeminal ganglion neurons. The properties of these cells have been studied in culture with light microscopy, but have only yielded to electrophysiological recording *in vivo*. We developed a novel *ex vivo* preparation of the vibrissae pad, trigeminal nerve, and trigeminal brainstem. Briefly, we surgically extracted this primary circuitry from the mouse or postnatal rat; introduced calcium indicators into trigeminal ganglion cells using several techniques, including targeted brainstem injections of Oregon-Green BAPTA1 (OGB-1)-AM [Stosiek et al., 2003, Ohki et al., 2005], somatic optoporation [Rau et al., 2006, Lei et al., 2008, Schinkel et al., 2008] of OGB-1-AM, and transgenic expression of troponin-based calcium sensors in Thy1-CerTN-L15 and TN-XXL mice [Heim and Griesbeck, 2004, Heim et al., 2007, Mank et al., 2008]; and imaged calcium activity in response to mechanical stimulation of vibrissa and pharmacological manipulations. In the process of analyzing the large population of cells from individual experiments, I began writing a cell detection algorithm for two photon images. We published an extension of this work, which I include in chapter A. In addition to the work's origins in experiments on the trigeminal system, this chapter is thematically related to chapter 3 in its use of statistical learning to uncover important, yet sometimes subtle, features in data.

*Because of the disparate fields addressed, I introduce the literature relevant for each of these topics in their respective chapters. In keeping with the style of scientific prose, I use first person plural pronouns in the substantive chapters of this dissertation.*

# Chapter 2

# An excitatory, disynaptic brainstem pathway for sensorimotor feedback in the control of whisking

## 2.1 Abstract

Sensorimotor processing relies on hierarchical circuits of increasing complexity to mediate sensory-driven behaviors; yet, synaptically connected control circuits from sensor to muscle have been only inferred from the physiology of reflexes or the tracing of afferents or efferents independently. Here, we demonstrate a complete disynaptic brainstem circuit for vibrissal somatosensation and motor control. The interneurons in this pathway are morphologically distinct from those in neighboring regions. They receive localized input from vibrissa sensory afferents, and project to lateral facial nucleus motoneurons that directly innervate vibrissa musculature. We use dual labeling strategies with complementary viruses and transgenic animals to show that connections with trigeminal ganglion afferents and facial nucleus motoneurons are monosynaptic. Further, we demonstrate that these neurons are primarily glutamatergic. These results fully outline a previously unknown disynaptic trigeminal reflex arc that is reminiscent of spinal cord laminar circuitry. Because it employs just two excitatory synapses, this circuit suggests a general architecture for the fast, positive feedback seen in active sensing systems, and likely mediates particular sensory-driven motor behaviors observed in the vibrissa system.

## 2.2 Introduction

Behavior is the purposeful and reactive motor output of an organism in response to sensory input [Skinner, 1938, Powers, 1973]. In mammalian systems, behavior results from the coordinated activity of hierarchical, parallel, nested synaptic loops in the brain and spinal cord [Squire et al., 2008]. For most sensory modalities, the brainstem provides the first neural substrate for active sensation, in which closed-loop dynamics guide motor output to update selectable sensory inputs optimally for perception during behavior [Gibson, 1962, Kleinfeld et al., 2006, Schroeder et al., 2010]. Given selective pressure for fast, context-relevant behavior, brainstem sensorimotor circuits minimize the number of synaptic relays between sensors and effectors. These loops are ensconced in a dense and non-laminar three-dimensional structure that restricts anatomical access to interrogate putative circuits with traditional tracers. Thus, the full reconstruction and characterization of individual closed-loop brainstem circuits from sensory transduction to muscle output has eluded clear demonstration.

The mouse trigemino-facial brainstem, which mediates active sensation in vibrissa sensorimotor behavior, boasts an anatomy well suited for characterizing low-level control circuits [Kleinfeld et al., 1999, Kleinfeld et al., 2006]. Trigeminal ganglion (Vg) cells receive sensory signals from afferents innervating vibrissae on the face [Rice et al., 1993, Rice et al., 1997] and terminate throughout the trigeminal brainstem (Vbs) [Ramon y Cajal, 1905, Åström, 1953, Kerr, 1963, Marfurt, 1981, Arvidsson, 1982]. Vbs is composed of four nuclei situated discretely throughout the pons and medulla [Olszewski, 1950], and contains both excitatory and inhibitory interneurons [Li et al., 1997, Avendaño et al., 2005, Furuta et al., 2008] that project within and among trigeminal nuclei [Falls, 1984, Jacquin et al., 1989, Hallas and Jacquin, 1990, Bellavance et al., 2010]. Many of these nuclei project directly or indirectly to lateral facial nucleus (VIIm), which controls vibrissa musculature [Courville, 1966, Komiyama et al., 1984, Klein and Rhoades, 1985], completing the shortest potential series of closed sensorimotor loops. However, the origin, extent, and terminal zones of trigeminal afferents and trigeminofacial projections are disputed [Erzurumlu and Killackey, 1979, Takeuchi et al., 1979, Panneton and Martin, 1983, Travers and Norgren, 1983, Holstege et al., 1986, Isokawa-Akesson and Komisaruk, 1987, Pellegrini et al., 1995, van Ham and Yeo, 1996, Hattox et al., 2002]. Several physiological preparations probing Vbs connections with VIIm suggest a net excitatory, disynaptic circuit, possibly to improve muscle tone and sensory acuity during whisking [Sachdev et al., 2003, Nguyen and Kleinfeld, 2005]. In light of disagreements about trigeminal microanatomy and limitations in trigeminofacial physiology, the precise circuit architecture that underlies the phenomenology of fast trigeminofacial feedback remains unknown.

Here, we identify and characterize a trigeminofacial sensorimotor brainstem loop. We use a repertoire of tract tracing tools that enable discrete study of neuron subpopulations along pathways in which the fewest number of synapses is necessary to proceed from sensory input to motor output. We take advantage of the fact that trigeminal afferents and facial efferents can be labeled discretely by their distinct terminations with non-neural organs, skin and muscle respectively. We also exploit and extend several novel molecular and viral tools [Wickersham et al., 2007, Gradinaru et al., 2010, Wall et al., 2010] (Takatoh et al., under review) and confirm these with both anterograde and retrograde, single- and double-labeling experiments with traditional tracers. Last, we evaluate the neurotransmitter content of the interneurons within this disynaptic pathway with *in situ* hybridization.

## 2.3 Methods

### 2.3.1 Animals

Sixty-three C57Bl/6 adult male mice (24 ± 2 g, age at perfusion of 66 ± 7 d) and 10 transgenic mice (varying age, adult and postnatal) were used for all anatomical labeling experiments. Animals were anaesthetized with inhalation isoflurane (0.5-2% in $O_2$, depending on weight and response), in some cases after an initial dosage of ketamine and xylazine (0.13 and 0.01 mg/g body weight, respectively), and body temperature was maintained at 37°C using a servo-controlled heating blanket. Animal care and treatment conformed to the National Institutes of Health Guidelines and were approved by the Institutional Animal Care and Use at University of California, San Diego. The researcher performing injections, the author of this dissertation, was properly vaccinated against rabies, and experiments were performed exclusively in a Biosafety 2 laboratory.

### 2.3.2 Stereotaxic injections of tracers and viruses

We use several tracers and viruses for different experiments; the details of each tracer are included in Table 2.1. For peripheral sensory nerve labeling experiments, $\sim 1.0-2.0$ $\mu$L of 1% Cholera toxin subunit B (CTb; List laboratories, #103B; Campbell, CA) [Angelucci et al., 1996] was injected subcutaneously and unilaterally on the left hemi-section of the face into one of maxillary, mandibular, or ophthalmic nerve terminal branching zones of trigeminal ganglion (Vg) afferents. Injections were made with a 10 $\mu$L Hamilton syringe (Hamilton Company, Reno, NV) coupled to tubing and a 30-gauge injection needle. For full trigeminal ganglion labeling, the mouse was positioned in a stereotaxic instrument (M900, Kopf), and a $2 \times 2$ mm craniotomy was centered at 1.5 mm rostral to bregma and 1.7 mm left of the midline. In most cases (8 of 15), vibrissa-responsive cells in Vg were located by manual mechanical stimulation of the ipsilateral vibrissae while extracellular recording in Vg with a thin tip diameter ($\sim 10\ \mu$m) quartz pipette filled with 0.5 M NaCl, amplified (Axoclamp 900A; Molecular Devices, Sunnyvale, CA) and observed on an oscilloscope (Tektronix TDS 224) and audio speaker. Vg vibrissa-responsive cell locations in the maxillary branch were consistent relative to stereotaxic coordinates, precluding the need to record in all animals. A thin quartz injection pipette (0.6 mm ID, 1.0 mm OD, pulled to $\sim 20\ \mu$m tip on P-2000, Sutter Instrument, Novato, CA) was advanced to $5.7-6.0$ mm below the surface, or the precise location of maximal vibrissa responses, with a micrometer-resolution manipulator (MPC-200, Sutter Instrument), and $\sim 80-400$ nL of 0.5 or 1% CTb was injected by pressure using a custom circuit triggered by a pulse generator (Grass S48 stimulator). Animals were allowed to survive for $3-10$ d to maximize afferent labeling in brainstem.

For disynaptic motor projection labeling experiments with virus, a 10 $\mu$L Hamilton syringe was passed through a $\sim 2-3$ mm incision dorsal to the A-row vibrissae of the left face, and advanced into the vibrissa pad musculature. Several focal injections of the 152 Bartha strain of Pseudorabies virus (PRV; titer: $1\times10^9$; L. Enquist, Princeton University) were made along the dorsoventral axis of the pad with a total injected volume of $5.0-7.0\ \mu$L. After suturing the incision, the virus incubated in the live animal for $48-72$ h, to determine optimal transsynaptic labeling protocol.

For identifying facial nucleus (VIIm) motoneurons projecting to vibrissae musculature, a tungsten single channel electrode (0.5 M$\Omega$, WE30030.5A10; MicroProbes) was advanced just caudal to the transverse sinus, through a cranial window centered 5.5 mm caudal to bregma and 1.5 mm left of the midline. To improve access to the rostral portion of lateral VIIm without damaging the sinus, the head was rotated/pitched such that the bregma-lambda horizontal of the skull was 6° below parallel. A microstimulation protocol of $100-200\ \mu$s pulses at 10 ms intervals for 100 ms, over a range of 500 nA to 20 $\mu$A, was used to identify exclusively or primarily vibrissa-controlling motoneurons (Isolated Pulse Stimulator 2100, A-M Systems). When sufficient whisker movement was elicited from minimal stimulation intensity, generally $< 2\ \mu$A, at $4.8-5.2$ mm below brain surface, the stimulation electrode was replaced with a quartz injection electrode with $6-25$ $\mu$m tip diameter, depending on the reagent. For fluorogold (2% w/v in 0.1 M cacodylic acid; company) injections, the reagent was iontophoresed using positive current pulses from an Axoclamp 900A amplifier of 150 - 400 nA at 2 Hz half duty cycle for 20 m. The animals were allowed to recover for 2-3 d. For rabies virus injections, glycoprotein-deleted rabies (ΔG-RV; pSAD-dG-GFP-M0; titer: $4.1 \times 10^9$ units/mL; E. Callaway, Salk Institute) was pressure-injected over 5 min, followed by 5 min delay before removing the pipette. In both cases, we used a separate pipette for stimulation and injection to avoid, in the case of fluorogold, pre-injection leakage of the charged tracer, and, in the case of virus, possible spread to local regions.

The ChAT-mediated rabies injection and molecular strategy has been described elsewhere (Takatoh et al., under review). In brief, we used a knock-in mouse line in which CAG-loxP-STOP-loxP-rabiesG-IRES-TVA was inserted into the intron of the ROSA26 locus, then crossed with a Chat::Cre knock-in driver line, such that rabies-G was expressed in all motor neurons, which are ChAT-positive. ΔG-RV was injected into the facial pad of RΦGT at age P1, and at P8 the mice were euthanized.

For dual-label adeno-associated virus (AAV) injections, injections were made as described above, except that $\sim$ 280 - 750 nL AAV6-EF1a-mCherry-IRES-WGA-Cre (titer: $2 \times 10^{12}$ Vg/mL; University of North Carolina Vector Core) was pressure injected in Vg, and 350-500 nL AAV2/1-CAG-FLEX-EGFP-WPRE-bGH (titer: $9.02 \times 10^{12}$ GC/mL; University of Pennsylvania Vector Core) was pressure injected into lateral VIIm following electrical stimulation to isolate the lateral VIIm. For Vg labeling, we chose the AAV5 serotype for its optimal transduction in sensory ganglion cells [Mason et al., 2010]; for retrograde labeling from VIIm, we chose AAV1, though AAV6 may have improved efficiency if it were readily available [Burger et al., 2004, Hollis et al., 2008].

### 2.3.3 Perfusion and immunohistochemistry

In all cases, mice were deeply anesthetized with inhalation isoflurane ($3-4$%) followed by intraperitoneal injection of $100-200$ $\mu$L of pentobarbital (Fatal Plus), transcardially perfused with phosphate-buffered saline followed by 4% paraformaldehyde in 0.1 M phosphate-buffered saline (PBS), pH 7.4. After removal from the skull and at least three hours of 4% PFA exposure, the brain, trigeminal ganglia and nerves, and facial skin were each cryoprotected in 30% w/v sucrose in 0.1 M PBS, and sectioned on a freezing microtome. Brain and upper cervical spinal cord were serially sectioned at 30 $\mu$m (CTb and some light microscopy tissue) or 60 $\mu$m (all other tissue) in one of three standard stereotaxic planes (sagittal, transverse, and horizontal). For dark product reactions of CTb cases, sequential sections were treated with Nissl stain (Cresyl violet acetate, Sigma C 5042), Giemsa (Original Azure Stain, WVR 15204-144), and Goat anti-cholera toxin primary antibody (1:12,000, List laboratories, Cat. #703) followed by rabbit anti-goat IgG (1:200, Vector Company #BA-5000) and 0.025 mg/mL DAB solution (Sigma D-5637). Face and ganglion sections, where treated, were prepared similarly. Sections were mounted, dehydrated in ascending alcohols, delipidized in xylenes, and cover-slipped with Cytoseal 60 (Fisher Scientific NC952739). For all other dark reaction product experiments, sequential sections were immunoblocked (0.1 M PBS containing 2% normal horse serum, NHS, with 0.25% Triton-X), treated with the relevant primary antibody for GFP-tagged pseudorabies (anti-PRV, Abcam Ab3534, 1:1000; anti-GFP, Novus Biologicals NB600-308, 1:1000) or fluorogold (anti-fluorogold 1:4000, AB153 Millipore) in immunoblocking solution for $12-18$ h, washed with 0.1 M PBS, incubated in cytochrome oxidase, containing cytochrome C (300 $\mu$g/mL) and 3,3'-diaminobenzidine (DAB, 500 $\mu$g/mL) for 30 min to 2 h at 37°C, washed with 0.1 M PBS, incubated in ABC Elite kit (Vector Labs, CA) for 3 h, revealed with SG Immpact kit (Vector), mounted, dehydrated, delipidized, and cover-slipped (Permount, Electron Microscopy Sciences).

For fluorescence experiments, sections were sliced at 30 $\mu$m, mounted on gelatin-coated slides, air-dried, rinsed with 0.1 M PBS, incubated for at least 20 min at room temperature in blocking buffer (0.1 M PBS containing 2% NHS with 0.25% Triton-X), then incubated $12-18$ h in the same blocking buffer with a primary antibody to the virus or tracer (rabbit anti-PRV, Abcam Ab3534, 1:1000; anti-GFP, Novus Biologicals NB600-308, 1:1000; goat anti-CTb, List 703, 1:3000). Intrinsic GFP fluorescence of Rabies-GFP was sufficiently strong to preclude antibody labeling. After rinsing with 0.1 M PBS, sections were incubated for 2 h with appropriate secondary antibodies (Alexa Fluor 594 anti-goat, 1:200) for 2 h, rinsed, dried, and exposed to a fluorescent Nissl stain, Neurotrace (1:200; Invitrogen N-21479 blue, N-21482 red), for 40 min, and cover-slipped (Fluoromount G, EMS).

### 2.3.4 *In situ* hybridization

The *in situ* hybridization procedure has been described elsewhere [Furuta et al., 2008], but briefly, following fixation, cryoprotection in DEPC-treated sucrose, and sectioning at 50 $\mu$m, sections were washed in PBS for 5 min, acetylated in freshly prepared 0.25% (v/v) acetic anhydride in 0.1 M Triethanolamine for 10 min, rinsed in 30 mM NaCl and 30 mM sodium citrate (2× SSC), and hybridized with 1.0 g/mL digoxigenin-labeled sense or antisense RNA probes for GAD67, VIAAT, VGluT1, and VGluT2 in 50% (v/v) formamide, 5× SSC, 2% blocking reagent (Roche Diagnostics), 0.1% N-Lauroylsarcosine (NLS), and 0.1% SDS for 20 h at 70°C. After 2× wash in 50% formamide, 2× SSC, and 0.1% NLS for 20 min at 70°C, sections were incubated with 20 g/mL RNase A for 30 min at 37°C, washed in 2× SSC and 0.1% NLS for 20 min at 37°C, then in 0.2× SSC and 0.1% NLS for 20 min at 37°C. Finally, sections were incubated with 1:3000 peroxidase-conjugated sheep anti-digoxigenin antibody Fab fragment (Roche Diagnostics), amplified with biotinyl tyramide reagent, and incubated with Alexa 488-conjugated streptavidin (10 $\mu$g/ $\mu$L; Invitrogen) in PBS with 0.3% Triton X-100 for 1 h.

### 2.3.5 Imaging and digitization

Slides were imaged serially and automatically using a whole-slide imaging scanner (NanoZoomer 2.0-HT, Hamamatsu Photonics, Japan) at 0.453 $\mu$m/pixel resolution under a 20× (0.75 NA) objective (Olympus) under illumination from a 200 W mercury lamp. This system uses line scanning of a 3-channel time-delay integrated sensor to resolve both fluorescent and brightfield images at $\sim 8$ (brightfield) to $\sim 25$ (fluorescent) min per slide for our tissue. Fluorescent images were collected using a 3-filter cube for red, green, and blue spectral separation. Images were evaluated and converted from NDPI format to TIFF or JPEG formats using ImageScope (Aperio) and leveled and downsampled in Photoshop (Adobe).

Confocal imaging was performed on an Olympus FV1000 and a Leica SP5 upright microscope, using 20× air, 100× oil, and 60× glycerol objectives, with an automatically set objective-matched pinhole size appropriate for thin optical slices. Images were converted and leveled in Fiji (an open source ImageJ distribution).

For volumetric reconstructions, full-slide images were automatically or manually sectioned according to the position of the tissue slices. Each slice was then traced either manually or semi-automatically, and tracer locations were identified and traced according to intensity of the dark product reaction against the tracer or virus of interest using Neurolucida (MicroBrightField Inc., Williston, VT). Brain traces were oriented in the z-axis, registered, and projected to three dimensions. For cell counting, individual cells in subsequent sections were manually identified using size range and morphology criteria, then assembled as above using Neurolucida, imported to Matlab, and distances quantified automatically using custom software.

## 2.4 Results

To determine the existence and connectivity of putative disynaptic circuits in trigeminofacial brainstem, we employed a series of histological preparations, traditional tracers, and virus labeling in wild type and transgenic mice (summarized in Table 2.1). Since gross morphology often recapitulates connectivity, we begin by assessing the cytology of spinal trigeminal brainstem (SpV).

### 2.4.1 Morphological evidence for a partitioning zone in spinal trigeminal brainstem

The four primary divisions of the mouse trigeminal brainstem (Vbs) are differentiable by gross cytological and chemoarchitectural [Olszewski, 1950, Kerr, 1970, Ma, 1991, Avendaño et al., 2005]; these nuclei are the principalis (PrV), oralis (SpVo), interpolaris (SpVi), and caudalis (SpVc) divisions (Figs. 2.1 for schematics and 2.2 for example sections). The caudal boundary of SpVi terminates near caudalis SpVc at the beginning of substantia gelatinosa (SG), located obliquely but near to the transverse plane of the obex. Caudal SpVi has large cells dorsally and medium-sized cells ventrally, SpVc has smaller, denser Nissl bodies. Interestingly, the interface between SpVi

**Table 2.1**: *Virus-based and traditional labeling strategies employed.*

| **Virus or Tracer** | **Directionality** | **Synaptic count** | **Injection** |
|---|---|---|---|
| CTb | Antero- & retrograde† | Monosynaptic | Vg Face |
| FG | Retrograde | Monosynaptic | VIIm |
| PRV | Retrograde | Transsynaptic | Face |
| ΔG-RV | Retrograde | Mono- & Disynaptic§ | VIIm |
| AAV5-WGA-Cre* | Anterograde | Transsynaptic | Vg |
| AAV1-Flex-GFP* | Retrograde | Monosynaptic | VIIm |

†We exploit the anterograde labeling of CTb for all experiments here, except those in figure 2.17.

§ΔG-RV is used in two contexts. In the experiments shown in figures 2.14 and 2.15, it is used as a monosynaptic retrograde tracer, unable to proceed transsynaptically because it lacks the glycoprotein necessary for transduction. In the experiments shown in figures 2.12 and 2.13, it is used in a transgenic animal (RΦGT, in which the glycoprotein is expressed only in ChAT-expressing cells). In this scheme, when both ΔG-RV and ChAT are present, a fully functional rabies virus is transduced and can infect monosynaptically connected cells. Transduction is no longer possible when cells infected with ΔG-RV do not express ChAT (i.e., in pre-motor neurons).

*Preliminary, see text.

and SpVc has smaller, oblong Nissl bodies and lower cell density (Fig. 2.2). These cytological features extend around the edge of SG, medially abutting parvocellular reticular formation (PCRt), extending laterally to the external fibers of the trigeminal nerve (Vn), and intermingling with SG along the lateral edge of SpVc caudally (Fig. 2.2).

Hereafter, we refer to this morphologically distinct zone as the spinal trigeminal muralis nucleus (SpVmu).

### 2.4.2 Sensory afferents in SpVmu and surrounding nuclei

We next asked whether this morphologically distinct region receives primary afferent input from peripheral trigeminal endings. We injected a large bolus of the anterograde tracer cholera toxin subunit B (CTb) directly into the trigeminal ganglion (Fig. 2.3A). Central afferents terminate robustly throughout all four major divisions of Vbs, in addition to trigeminal motor nucleus (Vm) and lightly in parts of reticular formation (Fig. 2.3B-C). The arborization pattern in SpVi is dense and robust; in SpVc is diffuse rostrolaterally, and increasingly robust caudally and medially towards spinal cord; and at the interface are thick and elongated in the dorsoventral axis (Fig. 2.3B-C).

Single vibrissal afferents are known to terminate throughout the trigeminal axis, and particularly in both caudal SpVi and rostral SpVc [Hayashi, 1985a,Hayashi, 1985b], with a distinct terminal morphology [Jacquin et al., 1984] at the interface of SpVi and SpVc at the level of the obex [Hayashi, 1980] (see his figure 1a) and an emphatic change in collateral distribution at this level [Hayashi, 1980] (see his figure 2), though the extent of these differences is disputed [Shortland et al., 1995]. In light of these single axon results, and the fact that the above morphological and gross connectional features suggest a nuclear distinction among the three spinal regions SpVi, SpVmu, and SpVc, we focally injected CTb directly into the vibrissa pad to label one or a few follicles and assess their spinal trigeminal arborization patterns (Fig. 2.4A). A small subset of barrelettes, the cytologically distinct functional brainstem units corresponding to individual vibrissae [Ma, 1991], were labeled as expected in SpVi and SpVc, but, strikingly, well-isolated axonal terminals filled SpVmu (Fig. 2.4B-C). The afferents are organized discretely according to each nucleus of termination: SpVi and SpVmu terminals abut one another at caudal SpVi but do not intermingle, and SpVc terminals are strongest

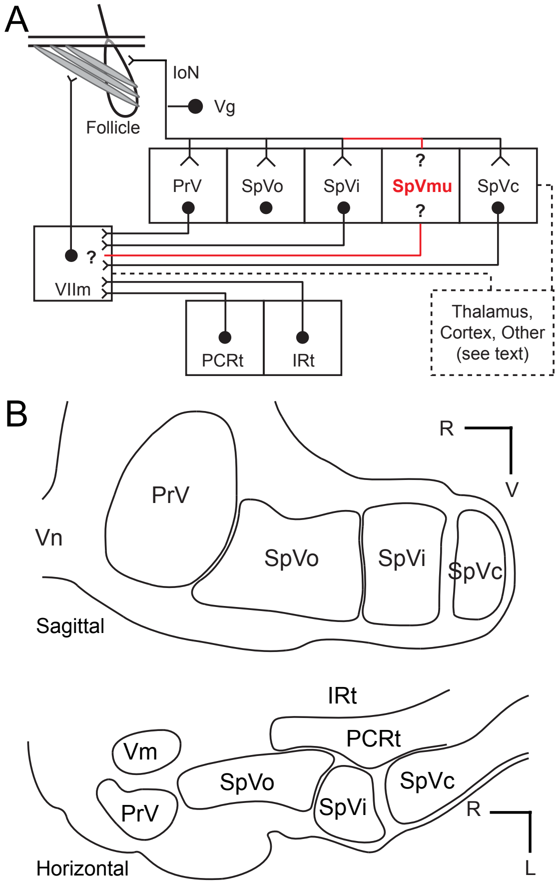

**Figure 2.1**: *Schematic and spatial arrangement of trigeminal nuclei.* (A) Schematic of trigeminal brainstem nuclei. Sensory afferents transmit signal from the whisker pad via the infraorbital (IoN) division of the maxillary branch of the trigeminal nerve (Vn) and terminate throughout the trigeminal brainstem (Vbs), including principal trigeminal nucleus (PrV), and oralis (SpVo), interpolaris (SpVi), and caudalis (SpVc), the spinal trigeminal nuclei (SpV). Secondary neurons in PrV and SpV project within and among Vbs, to facial motor nucleus (VIIm), and to thalamus, cerebellum, superior colliculus. VIIm motoneurons also receive input from disparate cortical and subcortical nuclei, and project to extrinsic and intrinsic musculature of the face for vibrissa motor control. In this chapter, we are concerned with the connections (red) in a putative new area, spinal trigeminal muralis (SpVmu). (B) Outlines of the four major trigeminal nuclei, the entrance of Vn, and other relevant brainstem nuclei, including motor trigeminal nucleus (Vm), intermediate reticular formation (IRt), and parvocellular reticular formation (PCRt). Shown in sagittal and horizontal sections.

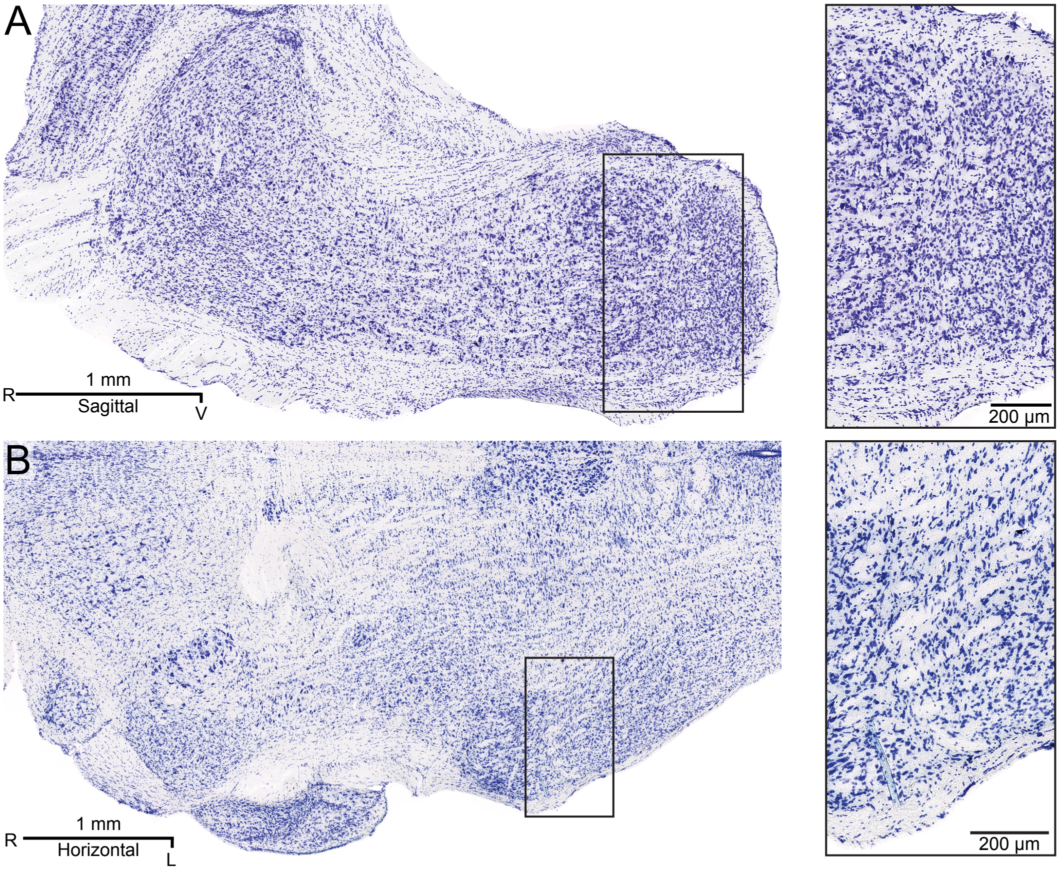

**Figure 2.2**: *Morphology of spinal trigeminal brainstem.*
(A) Nissl stained section in the sagittal plane matching the schematic in figure 2.1B, showing the distinct gross morphology of each of the four nuclei. Magnified image details the morphological differences at the border between SpVi and SpVc. (B) As in A, in the horizontal plane.

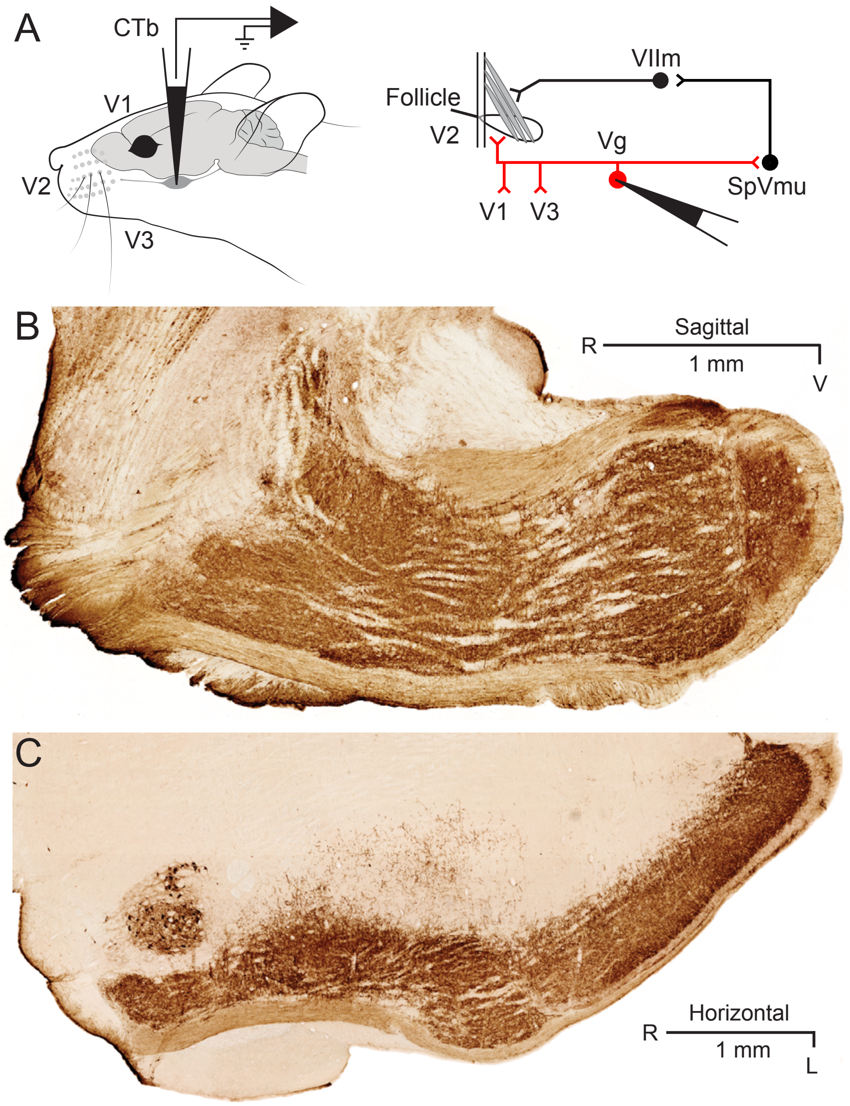

**Figure 2.3**: *Sensory afferent projections to trigeminal nuclei after ganglion injection with CTb.*

(A) CTb injection into the trigeminal ganglion, shown schematically in the mouse brain and in the putative trigeminal circuit. In most cases, vibrissa responses were recorded in Vg before injection. V1, V2, V3 are branches of Vn. (B) Representative sagittal section of trigeminal brainstem on DAB-prepared slice after bolus injection of CTb into Vg, showing dense axonal terminations throughout Vbs. though by comparison with other, part of the dorsal principal nucleus was unlabeled in this case, possibly due to incomplete ganglion labeling. (C) As in B, for a representative horizontal section. This section also shows labeling in Vm and PCRt, medial to sensory trigeminal brainstem.

$\sim 200\ \mu$m caudal to the rostral edge of SpVc. A volumetric reconstruction of this case, derived from DAB-treated slices adjacent to those shown in figure 2.4B-C, shows the three dimensional relationships of the regions labeled in the spinal trigeminal regions (Fig. 2.5).

To determine whether this confined terminal zone was exclusive to vibrissal inputs, we injected into portions of the face known to be innervated by each of the three branches of trigeminal nerve, ophthalmic (V1), maxillary (V2), and mandibular (V3) (Fig. 2.6A), and processed sections with DAB to visualize all arbors. Injections of CTb into the facial regions innervated by V1 and V3 branches of Vn show no labeling in SpVmu (Fig. 2.6, V1 and V3). Meanwhile, injections in maxillary-innervated face are seen robustly (Fig. 2.6, V2), shown here in a different case from Giemsa-processed tissue in figure 2.4. Together, these results suggest that SpVmu receives a distinct set of peripheral trigeminal afferent endings originating exclusively from the vibrissae.

### 2.4.3 Premotor neurons in SpVmu and surrounding nuclei

Motivated by the discrete termination of peripheral afferents in SpVmu, we next asked whether neurons in SpVmu are involved in vibrissa pad-specific motor output. We injected a transsynaptic, retrograde herpesvirus, pseudorabies-GFP, unilaterally into the intrinsic and extrinsic musculature of the vibrissa pad (Fig. 2.7A). Lateral facial nucleus (VIIm) motoneurons, which control both vibrissae protraction and retraction [Courville, 1966,Komiyama et al., 1984,Klein and Rhoades, 1985], were labeled within 48 hours of the initial injection while premotor neurons were not, and the number and degree of cell labeling increased with incubation time (Fig. 2.8). By 72 hours, lateral VIIm motoneurons were fully labeled and possibly apoptotic (Fig. 2.7B), while premotor neurons innervating VIIm were robustly labeled, primarily in ipsilateral brainstem (Fig. 2.7C). The greatest density of labeled neurons was in SpVmu, followed by both IRt and PCRt (Figs. 2.7C and 2.9). There were few labeled Vbs neurons outside of SpVmu (Fig. 2.7C). Labeling was essentially absent from contralateral SpVmu neurons, though there were a few neurons in contralateral reticular formation (Figs. 2.7C and 2.10A reconstruction).

In addition to a difference in density, the cells in SpVmu differed cytologically from those in IRt and PCRt; in particular, SpVmu were smaller and less golgi-like

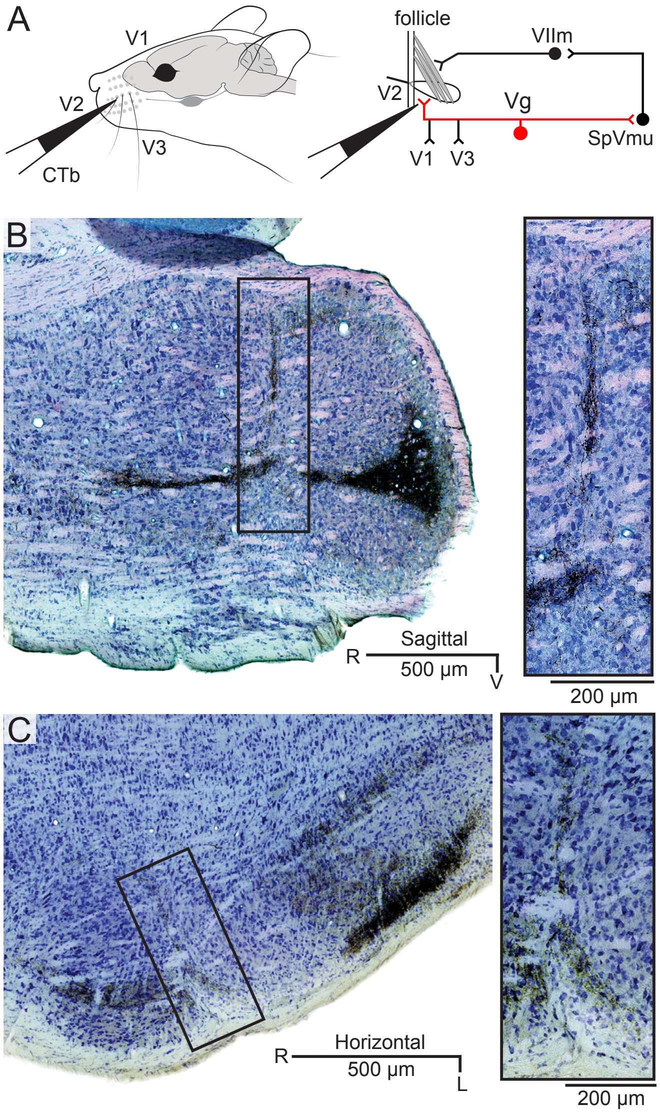

**Figure 2.4**: *Sensory afferents terminate locally in SpVmu after vibrissa pad injection with CTb.*

(A) Focal injection of CTb into a subset of follicles of the vibrissa pad (innervated by V2), shown both schematically in the mouse brain and in the putative trigeminal circuit. V1, V2, V3 are the branches of Vn. (B) Representative sagittal section of trigeminal brainstem. SpVmu, located between SpVi and SpVc, shows dense local terminal fields. Giemsa preparation was used to visualize both cell bodies and CTb labeling. (C) Horizontal section, as in C. Constrained arborization at the border between SpVi and SpVc is visible, as are the laminar divisions of SpVc, similar to spinal cord, and the mediolateral location of SpVi barrelettes.

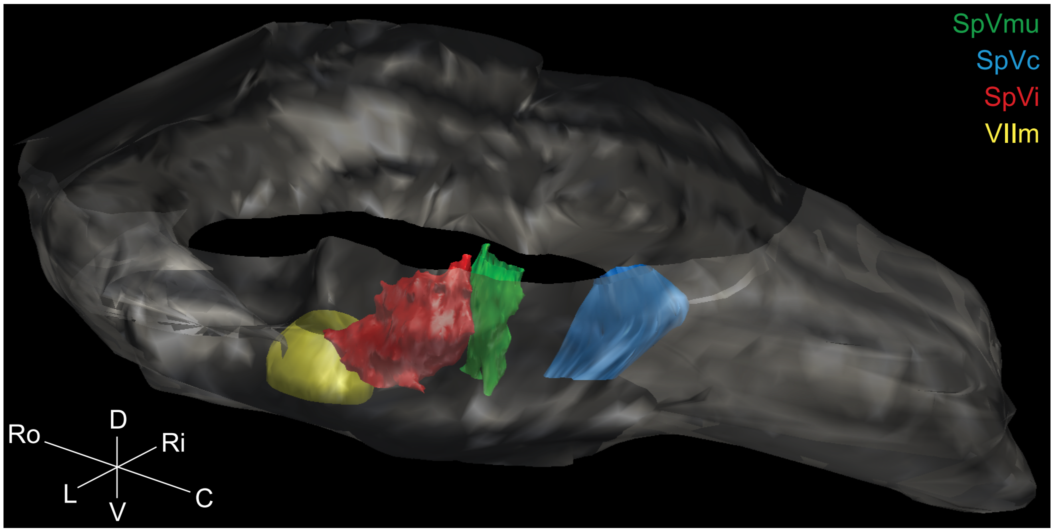

**Figure 2.5**: *Volumetric reconstruction of sensory afferent terminal zones following focal vibrissa pad injection.*

SpVmu shows a well confined terminal volume along the edge of SpVi and SpVc. Data are from DAB preparations on alternating slices of data shown in C. The view is from the left, caudal to and above bregma. For clarity, terminations rostral to interpolaris are not shown.

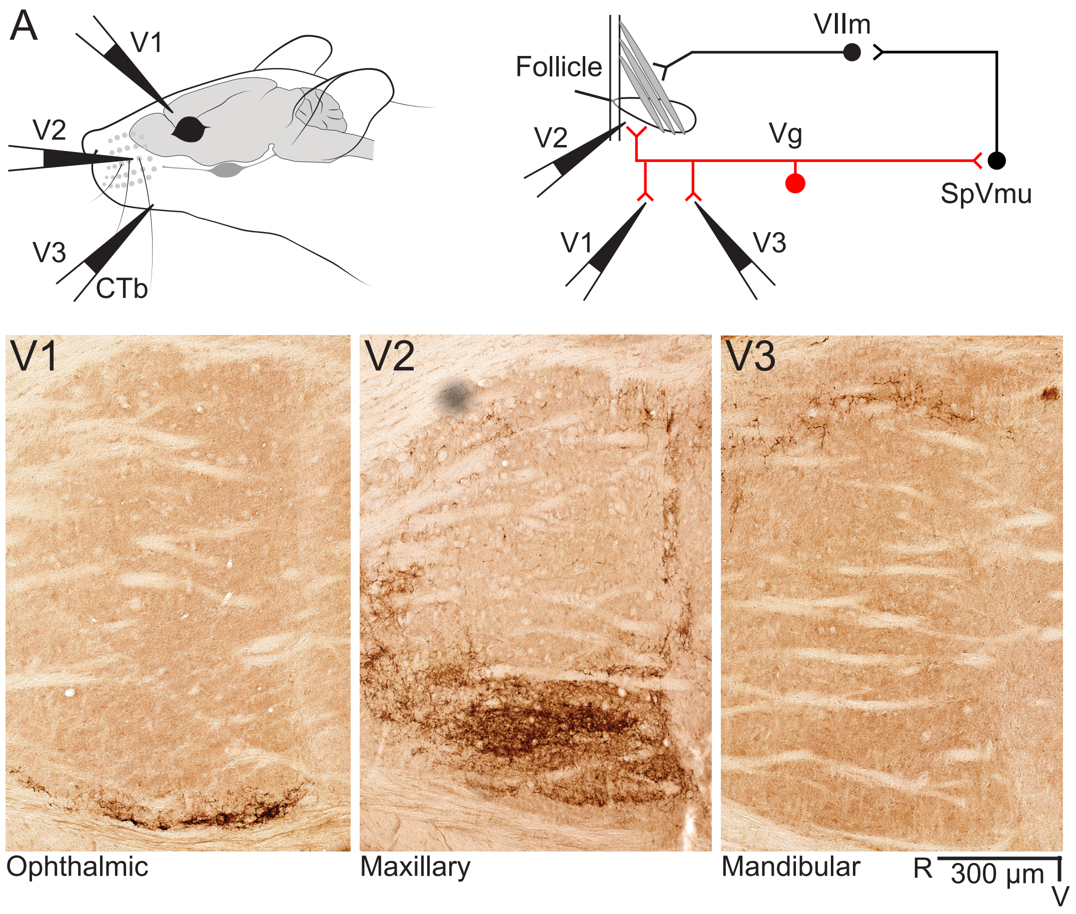

**Figure 2.6**: *Central afferents to SpVmu originate only from the maxillary branch.* Comparison of central afferents in SpVi and SpVmu following focal injections of CTb to the regions of the face containing peripheral endings for each of the three trigeminal nerve branches, ophthalmic (V1), maxillary (V2), and mandibular (V3). SpVmu is labeled only in vibrissa pad injections, which label the V2 branch, and not from labeling other branches.

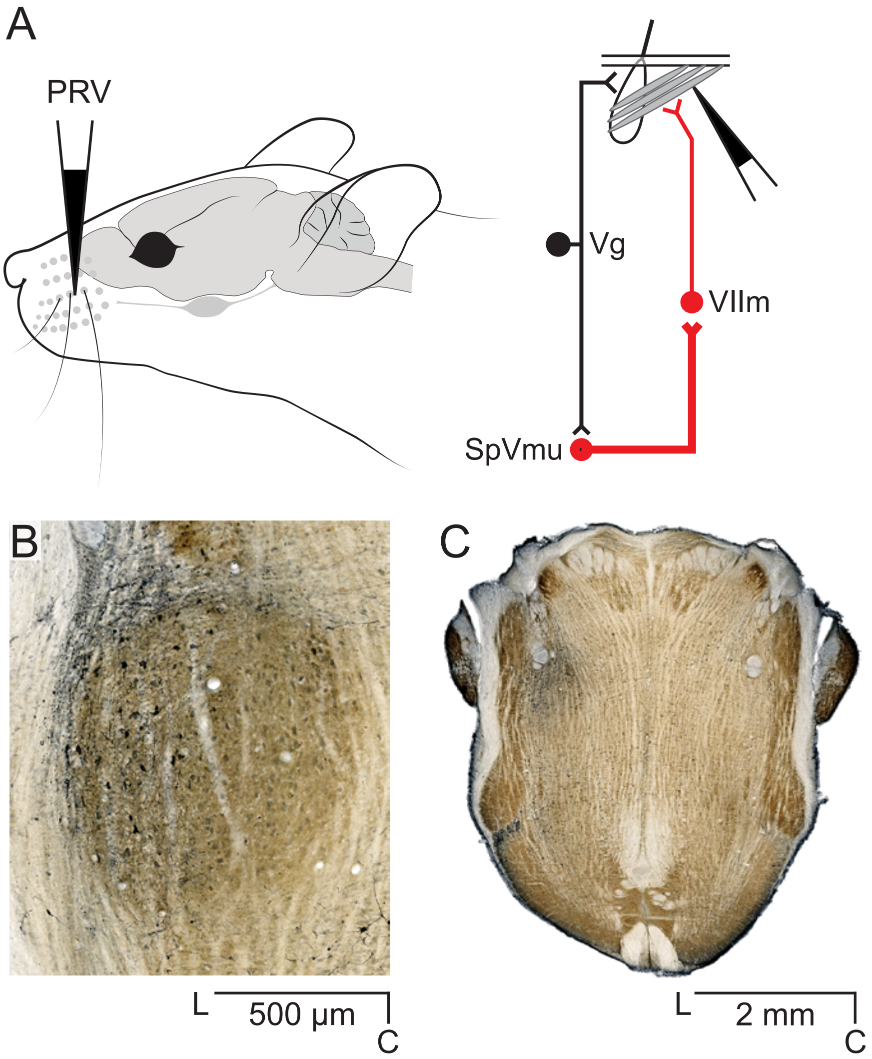

**Figure 2.7**: *Retrograde labeling by pseudorabies virus.*

(A) Injection strategy. PRV was injected into the intrinsic and extrinsic musculature of the left face. (B) PRV-positive labeling in lateral VIIm ipsilateral to injection, horizontal slice (60 $\mu m$ thickness). Large motoneurons are robustly labeled, as are parts of sphenopalatine nucleus, rostral to VIIm. Medial divisions of VIIm are unlabeled. (C) Representative brainstem slice showing PRV-positive cell labeling. The most robust and dense labeling is in ipsilateral SpVmu, though PRV is also visible in the genu of VII at this level, dorsal to VIIm. Contralateral SpVmu contains little or no staining.

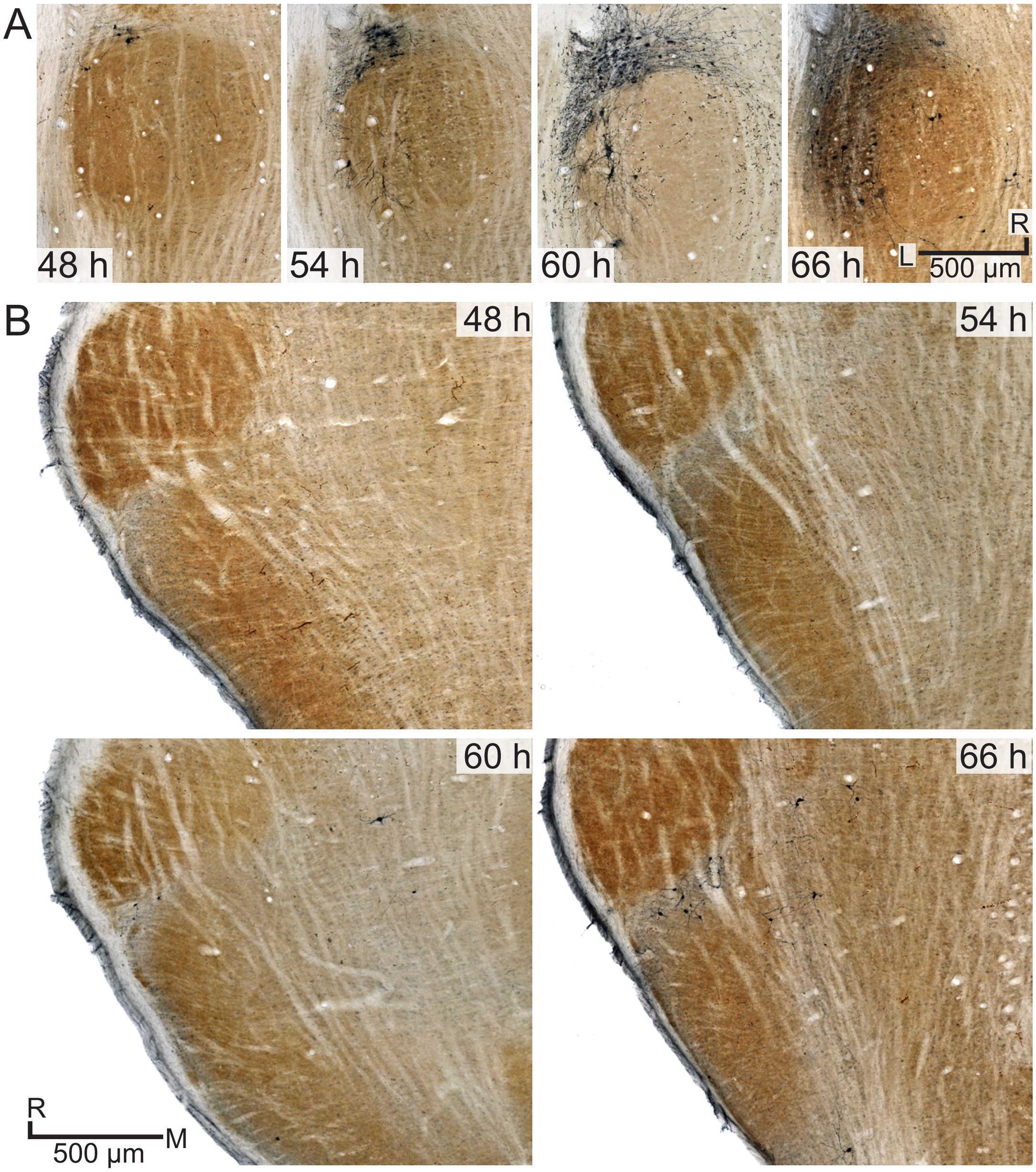

**Figure 2.8**: *Timing of transsynaptic transduction of pseudorabies-infected neurons.* Labeling of synaptically-connected cells progresses with time in lateral VIIm motoneurons (A) and SpVmu and reticular formation neurons (B). Time point shown are 48, 54, 60, and 66 hours.

(Fig. 2.9). To quantify both the density and distinct cytology among premotor neuron pools, we manually counted and grouped neurons according to their proximity to SpVmu (Fig. 2.10). Of all labeled neurons in sections with a clearly defined SpVmu, 646 (of 1942, 33%) had a small neuron morphology, while the remainder had a golgi-like appearance. Small neurons are overwhelmingly concentrated within SpVmu, with 92% of all SpVmu neurons within 100 $\mu m$ of the surface of the border between SpVi and SpVc (Fig. 2.10B). To visualize the three-dimensional location of all labeled neurons and compare with axonal arborization from CTb injections, we generated a volumetric reconstruction of positively labeled neurons for serial sections of the case in figures 2.7 and 2.9. In total, SpVmu contains the highest density of morphologically distinct neurons that project to VIIm motor neurons terminating on the vibrissae musculature.

PRV is a powerful tool to assess the polysynaptic connectivity of premotor neurons. However, its results must be confirmed because (1) it is replication competent, and timing alone cannot precisely distinguish the number of synapses in a circuit [Fay and Norgren, 1997], and (2) its tropism could effect which pre-motor cell populations are effectively labeled, due to the possibility of high false negative rates. In order to confirm that projections from SpVmu to lateral VIIm are not an artifact of PRV, we used a classical retrograde tracer, fluorogold [Schmued and Fallon, 1986], to confirm the connection. We microstimulated lateral VIIm with low current (typically $< 1\ \mu A$) to evoke one or few vibrissa(e) movements without activating non-vibrissal muscle fibers; we then returned to this location to inject the retrograde tracer fluorogold (Fig. 2.11A). Lateral VIIm motoneurons were robustly labeled (Fig. 2.11B). Within Vbs, retrogradely labeled cells were again most prominently seen in SpVmu, but were also visible in caudal SpVi and SpVc (Fig. 2.11C-D), and there were some contralateral connections down to C1 (data not shown). Cells in ipsilateral RF, and, less so, contralateral RF, were also labeled (Fig. 2.11C-D).

Despite the consistency between PRV and classical labeling results, there is a remote possibility that PRV in the vibrissa pad could have infected an unknown second population of brainstem neurons in addition to VIIm motoneurons that also received input from SpVmu, and that fluorogold labeled axons terminating in such a nucleus, which passed near or through VIIm. Therefore, we used a third strategy to confirm the

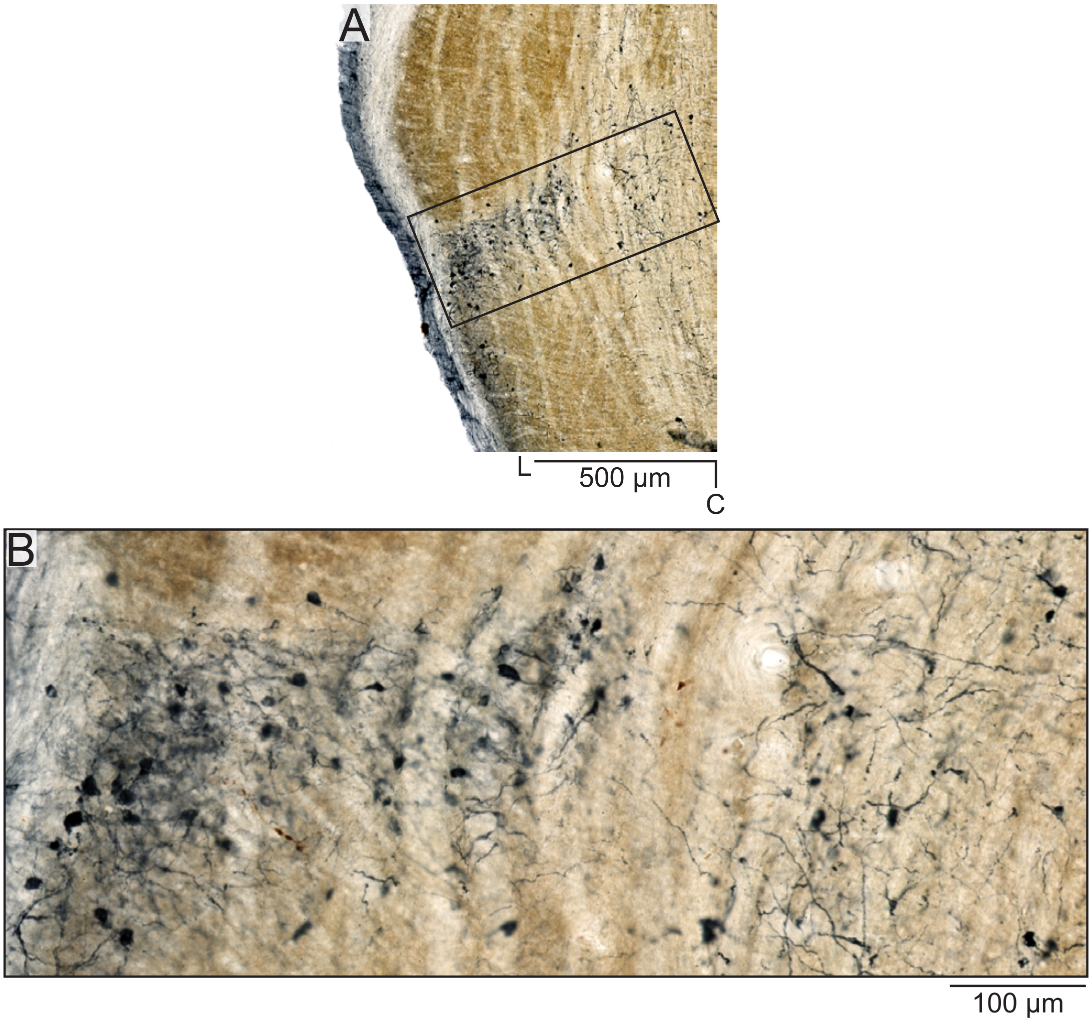

**Figure 2.9**: *Retrograde transport of PRV from VIIm robustly labels SpVmu neurons.* (A) Ipsilateral SpVmu and PCRt are robustly labeled. SpVmu is contained primarily within the bounding box. (B) Magnified image from A: VIIm-projecting SpVmu cells (left) are smaller and have more confined dendrites than the golgi-like labeled cells in PCRt (right).

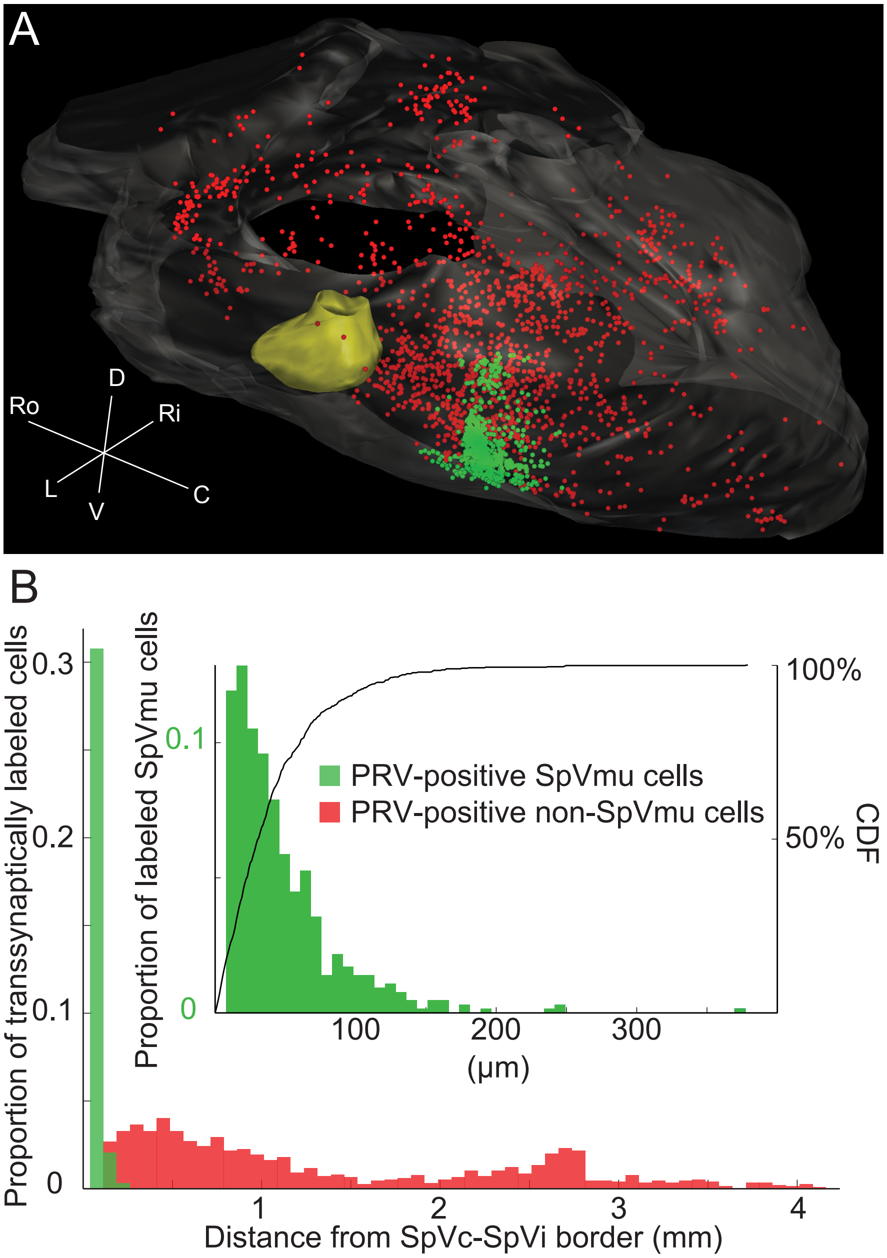

**Figure 2.10**: *Comparison of retrogradely labeled SpVmu and non-SpVmu neurons.* (A) Volumetric reconstruction of brainstem from serial sections of PRV, showing the locations of 2251 PRV-positive neurons: 646 SpVmu (green) and 1605 non-SpVmu neurons (red), primarily in reticular formation. (B) Comparison of cell distances from the interface of SpVi and SpVc, defined anatomically by cytochrome oxidase stain on each slice. Inset, proportion of SpVmu cells only as a function of distance from SpVc-SpVi border, with cumulative distribution function (CDF).

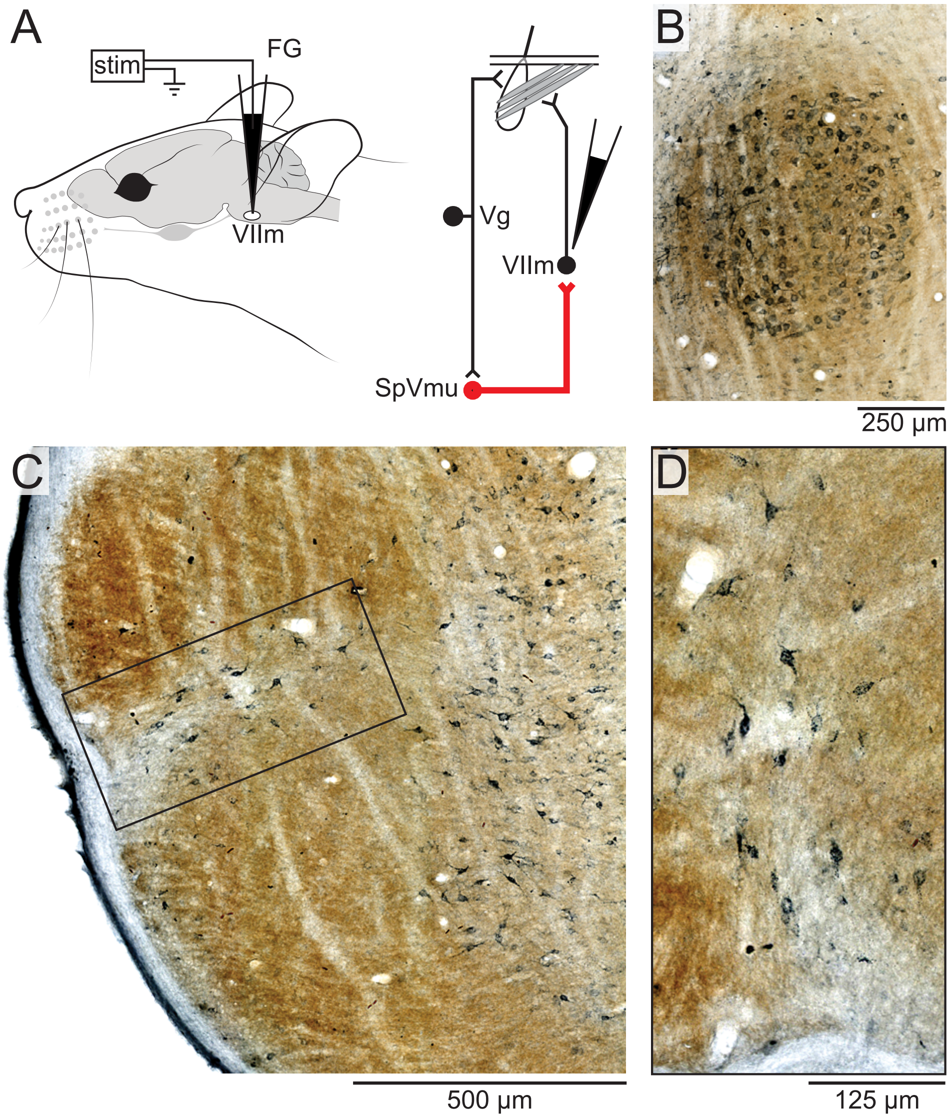

**Figure 2.11**: *Retrograde transport of fluorogold from VIIm labels SpVmu neurons.* (A) Fluorogold injection strategy. After targeting lateral VIIm by eliciting vibrissa movement in response to microstimulation with a tungsten electrode, tracer was iontophoresed over 20 minutes into VIIm. (B) Fluorogold labeling in VIIm motoneurons. Lateral VIIm is most strongly labeled, though some cells in medial VIIm were also labeled. (C) Fluorogold labeling of SpVmu, PCRt, and IRt. SpVmu is contained primarily within the bounding box, magnified in D. (D) Magnified image of SpVmu, showing individual SpVmu neurons at the border between SpVi and SpVc.

presynaptic status of SpVmu cells to lateral VIIm. We used a glycoprotein-G deleted mutant rabies virus coupled to GFP (ΔG-RV) in a mouse line conditionally expressing rabies glycoprotein G only in the presence of choline-acetyl-transferase (RΦGT) using a Chat::Cre knock-in driver (Fig. 4D and Methods; Takatoh et al., Neuron, in review). Under this strategy, only cells that are both retrogradely infected with ΔG-RV and are ChAT-positive are competent to generate rabies virus with the necessary glycoprotein for retrograde infection (Fig. 2.12B). Because VIIm is the only ChAT-positive brainstem nucleus that projects directly to vibrissa musculature (Takatoh et al., Neuron, in review), any GFP-positive cells outside of VIIm are necessarily monosynaptically connected to vibrissa-muscle projecting VIIm motoneurons. We injected ΔG-RV the vibrissae musculature of RΦGT mice at P1 and sacrificed at P8 according to this strategy (Fig. 2.12A). VIIm motoneurons are positively labeled, indicating successful transduction of the virus to the target from the peripheral musculature (Fig. 2.12C). Monosynaptically-connected premotor neurons are visible in parts of SpVo, SpVi and, notably, in the identical location of SpVmu that is seen in the PRV and FG experiments, at the border where cell density changes (Fig. 2.13). While fluorogold does not typically label dendritic arborization after retrograde transport along the axon to the soma, the robustly labeled rabies-positive dendrites are morphologically similar to those seen in SpVmu cells transsynaptically labeled with PRV (Figs. 2.9 and 2.13B-C).

The confluence of evidence from retrograde tracing results using fluorogold, pseudorabies virus, and ChAT-mediated rabies virus expression strongly suggests that SpVmu neurons project monosynaptically to VIIm motoneurons.

### 2.4.4 Monosynaptic connectivity of TG afferents to VIIm-projecting SpVmu interneurons

SpVmu receives peripheral sensory afferents and projects to motoneurons, but do inputs to SpVmu terminate near enough to somata or dendrites of premotor neurons to suggest putative synaptic contact? To address this question, we used a dual-label strategy in which CTb was injected into the whisker pad and ΔG-RV into the lateral division of ipsilateral VIIm (Fig. 2.14A). ΔG-RV is an ideal choice for identifying putative synaptic contacts because it (1) exclusively traverses chemical synapses, (2) strictly

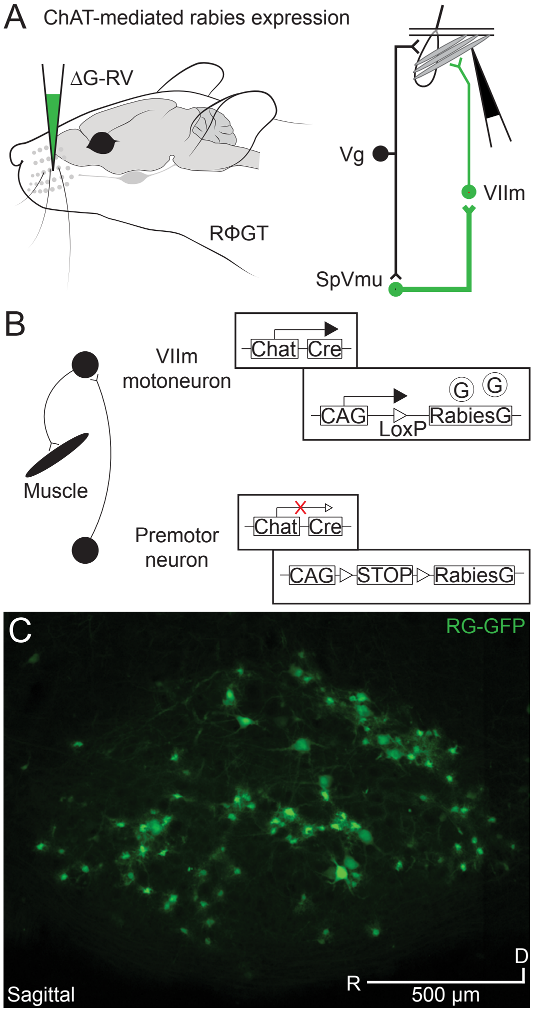

**Figure 2.12**: *Monosynaptic labeling strategy using modified rabies in a transgenic animal.*

(A) Injection strategy for pre-motor neuron labeling. ΔG-RV was injected into the facial musculature of RΦGT P1 mice, which were sacrificed at P8. (B) Molecular strategy for selective rabies labeling. Rabies glycoprotein is only expressed in the presence of ChAT, which is in VIIm motoneurons but not in premotor neurons, using the Cre-Lox system. In RΦGT mice, the presence of ChAT initiates transcription of Cre, which results in the expression of RabiesG; when (ΔG-RV) is also present, the rabies virus is competent to pass transsynaptically to connected targets. Thus, glycoprotein-deleted rabies in VIIm can monosynaptically and retrogradely pass to pre-motor neurons. (C) Rabies-labeled (green) motoneurons are robustly labeled in VIIm after injection into the periphery.

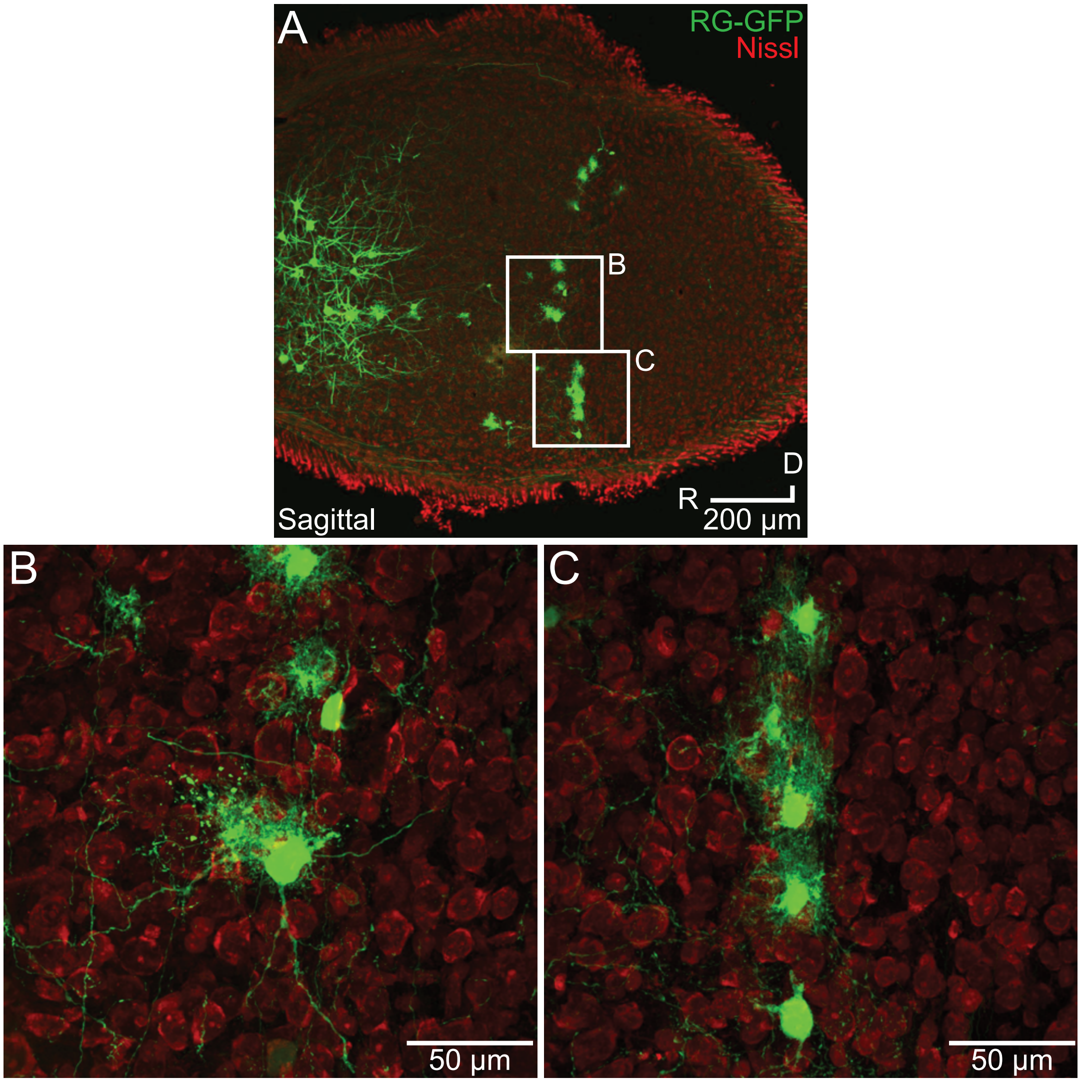

**Figure 2.13**: *Modified rabies labeling of premotor neurons in SpVmu.* (A) After injection of ΔG-RV into the periphery of RΦGT mice, spinal trigeminal neurons are labeled. In particular, monosynaptically-connected premotor neurons in SpVo, SpVi, and SpVmu are successfully labeled from VIIm motoneurons (green) and counterstained with a fluorescent Nissl (Neurotrace red). (B-C) Magnified images of two sets of SpVmu cells, showing dendritic arborization.

travels retrogradely and monosynaptically [Ugolini, 2010], and (3) contains intrinsic fluorescence sufficient to visualize dense dendritic arborization [López et al., 2010]. Lateral VIIm, the site of injection, was strongly labeled with ΔG-RV (Fig. 2.14B). Consistent with single-label experiments (Fig. 2.4), the punctate terminals of sensory afferents are labeled throughout SpVmu, as well as in parts of SpVi and SpVc (Fig. 2.15B-C). Also consistent with results from PRV (Fig. 2.9), FG (Fig. 2.11), and ΔG-RV in RΦGT (Fig. 2.13), SpVmu premotor neuron somata and neurites are robustly labeled (Fig. 2.15B-C); in fact, the dendritic trees were more densely labeled than in any of the previous retrograde labeling experiments (Figs. 2.9 and 2.13). We see putative axosomatic, trigeminal afferent axons to SpVmu somata (Fig. 2.15D-E), and axodendritic, trigeminal afferent axons to SpVmu dendrites (Fig. 2.15F-G), connections in this region. These results suggest that afferents to SpVmu interneurons are sufficiently proximal to generate synaptic contacts.

To further confirm that these putative synaptic contacts are in fact classical synapses, we employed a dual-label viral strategy (Fig. 2.16A-C). We used adeno-associated virus (AAV) in which wheat germ agglutinin (WGA), a classical tracer known to act transsynaptically in the periphery and brainstem when it is present in downstream cells [Kinoshita et al., 2002, Yoshihara, 2002, Damak et al., 2008], was fused with Cre recombinase (Cre), causing monosynaptically connected cells to contain Cre (Fig. 2.16A) [Gradinaru et al., 2010]. Second, we used AAV-Flex-GFP as a reporter virus: when Cre is present, the LoxP sites flanking a stop codon upstream of the GFP transcript are cleaved, allowing expression of GFP. For interrogation of this circuit, we injected AAV5-WGA-Cre into Vg and AAV1-Flex-GFP into VIIm; thus, only neurons that both receive direct input from Vg and project directly to VIIm will express GFP (Fig. 2.16B).

Preliminary data from this approach demonstrate the connection between Vg afferents and VIIm-projecting SpVmu neurons. Vg somata were strongly labeled following injection of AAV5-WGA-Cre (data not shown). Axons terminating in VIIm were very sparsely labeled by Cre-induced GFP expression (Fig. 2.16D), suggesting that some cells receiving input from Vg project directly to VIIm. Throughout the brainstem, very few neurons were labeled, but those that were labeled were primarily in trigeminal nuclei, including SpVmu (Fig. 2.16E). While preliminary (controls are in progress), these

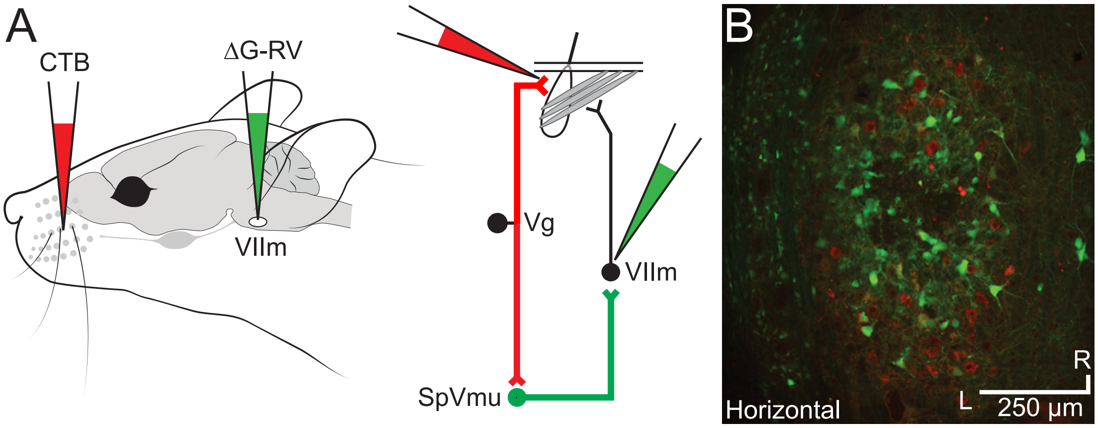

**Figure 2.14**: *Strategy for dual labeling of primary afferents and VIIm-projecting cells in SpVmu.*

(A) Injection strategy for dual labeling. CTb was injected into the whisker pad to label peripheral sensory afferents (red). ΔG-RV was injected into VIIm to retrogradely label monosynaptically connected premotor neurons. (B) VIIm motoneurons were labeled throughout VIIm, including lateral VIIm. CTb (red) is also present, as CTb travels both anterogradely and retrogradely from peripheral targets. We did not transect VII nerve, which would have prevented retrograde CTb labeling, but also compromised VIIm motoneuron viability and, thus, rabies transduction. There are no known axonal arbors of VIIm motoneurons extending to non-muscular targets, and CTb is monosynaptic, so there is no danger of spurious CTb labeling from VIIm.

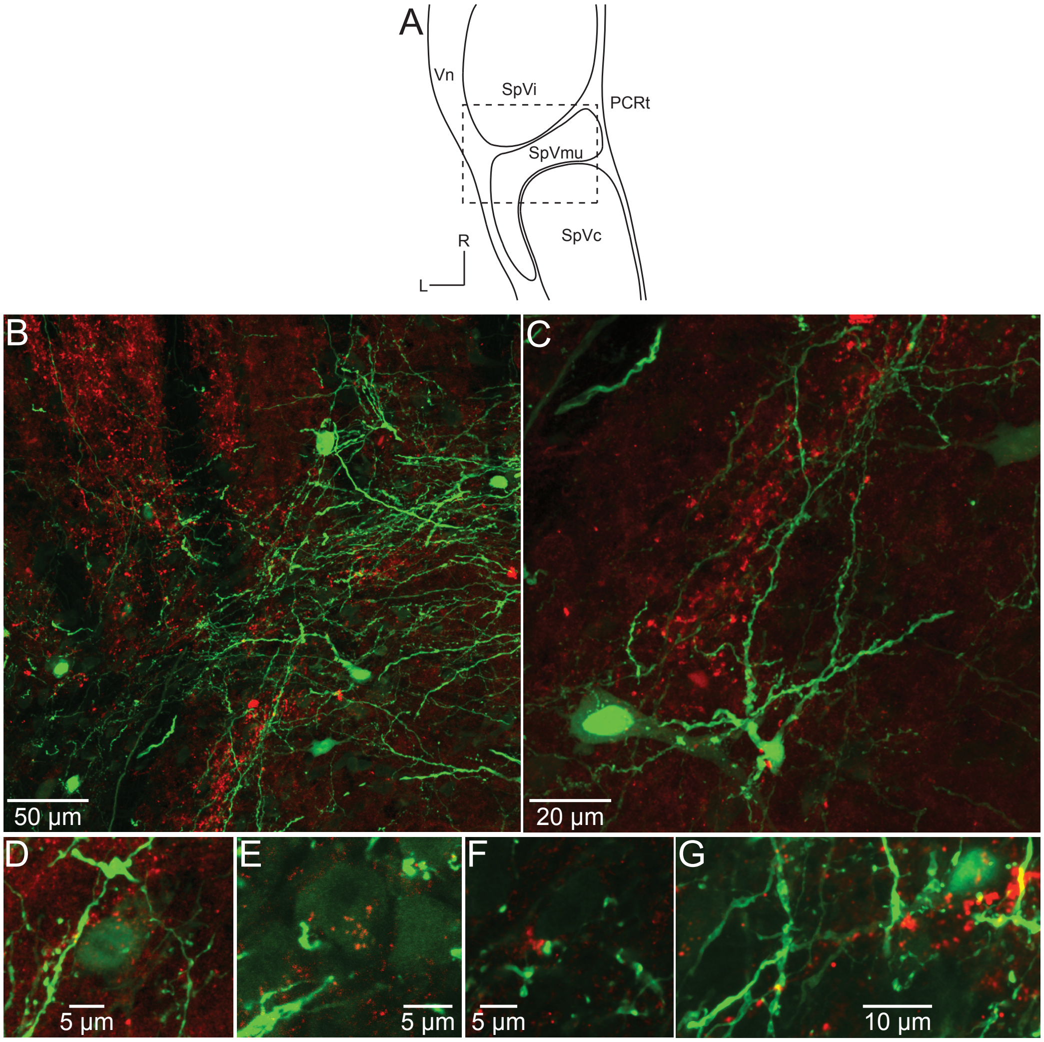

**Figure 2.15**: *Dual labeling of primary afferents and VIIm-projecting cells in SpVmu.* (A) For reference, organization of trigeminal nuclei within imaged regions. (B-C) CTb-labeled axons (red) and rabies-infected neurons (green). Dendritic trees of rabies-positive cells in SpVmu are abundant. Axons from the trigeminal periphery terminate throughout the SpVmu region of Vbs, particularly along portions of the region that contain dendritic arbors. (D-E) Putative axodendritic synaptic contacts, showing two cases of terminals across SpVmu soma. (F-G) Putative axosomatic synaptic contacts, showing close proximity to SpVmu and morphological features consistent with synapses.

data suggest that SpVmu neurons are synaptically connected both to Vg afferents and to VIIm motoneurons.

### 2.4.5 Neurochemical content of VIIm-projecting SpVmu interneurons

We have shown that SpVmu neurons are one set of interneurons monosynaptically connecting sensory afferents with motor efferents, but what is the sign of this connection? Both Vg sensory afferents [Zucker and Welker, 1969, Lo et al., 1999, Minnery and Simons, 2003] and VIIm motoneurons projecting to vibrissae musculature are excitatory, but the neurochemical content of SpVmu neurons has not been characterized. Evidence from physiology [Nguyen and Kleinfeld, 2005] and behavior [Sachdev et al., 2003] suggests that a positive feedback loop exists within trigeminal nuclei, but the neurochemical signatures of cells in neighboring SpVi and SpVc vary. PrV-projecting caudal SpVi neurons are almost exclusively GABAergic while PrV-projecting SpVc cells are glutamatergic [Furuta et al., 2008]; thalamic-projecting SpVi neurons are glutamatergic [Lavallée et al., 2005]; SpVi has the same proportion of glycinergic cells as SpVc, but has twice the proportion of GABAergic cells [Avendaño et al., 2005]; and VIIm-projecting Vbs cells are both GABAergic and glycinergic [Li et al., 1997], though excitatory cells were not assessed in that study. To determine the role of SpVmu interneurons in this disynaptic sensorimotor loop, we used *in situ* hybridization (ISH) for excitatory and inhibitory transcripts following injection of a retrograde tracer in VIIm, as before (Fig. 2.17A). We use *in situ* hybridization for vesicular glutamate transporter type 2 (VGluT2) to label glutamate-positive cells and vesicular inhibitory amino acid transporter (VIAAT) to label GABAergic and glycinergic cells. Preliminary data in morphologically similar SpVmu of rat (mouse data are in preparation), in which CTb was injected into VIIm and followed by ISH for VGluT2 and VIAAT, is shown in figure 2.17. Focusing on cells in SpVmu, there are many neurons co-labeled for CTb and VGluT2 (Fig. 2.17C); meanwhile, there are minimal numbers of cells co-labeled with VIAAT (Fig. 2.17D). Though we are currently completing analogous experiments in mouse and will quantify the co-labeling ratios, these preliminary results suggest that neurons of this region are excitatory, consistent with an overall fast feedforward description of the

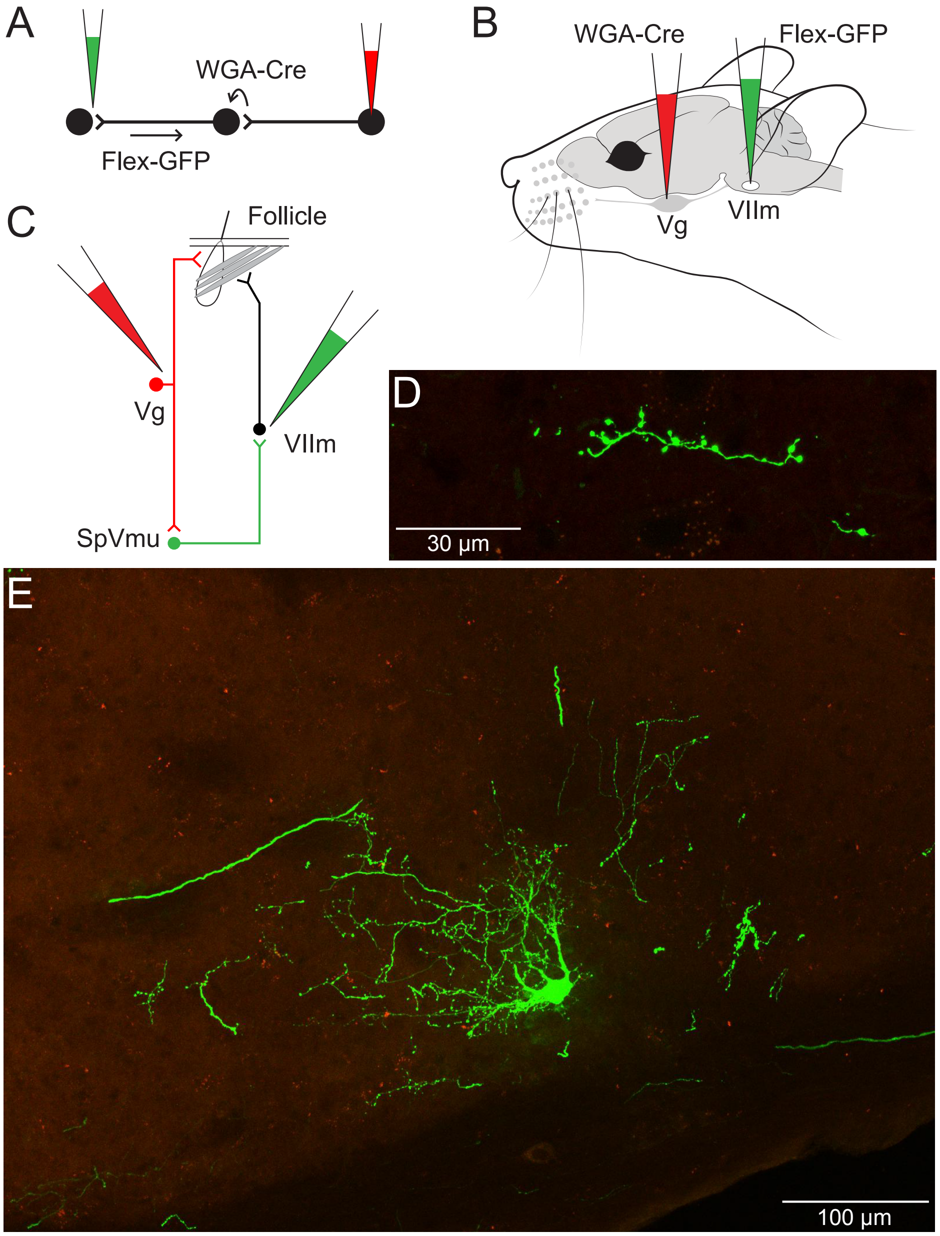

**Figure 2.16**: *Combined WGA-Cre and Flex virus labeling of SpVmu neurons.* (A) Viral strategy. WGA-Cre (red) is transported to synaptically connected neurons, and Flex-GFP (green) is retrogradely transported to the soma after uptake. Note that the RFP is only present in neurons directly infected with AAV, not in (B-C) AAV-WGA-Cre was injected into Vg and AAV-Flex-GFP into VIIm. (D) Labeled axonal terminal in VIIm. (E) A single labeled neuron in SpVmu.

behavioral and physiological results this circuit could underlie.

## 2.5 Discussion

We demonstrate a disynaptic sensorimotor circuit in the vibrissa system, specifically showing that (1) SpVmu is morphologically distinct from neighboring trigeminal nuclei SpVi and SpVc in both cell morphology and density; (2) vibrissa pad afferents terminate discretely in SpVmu; (3) SpVmu neurons receive direct synaptic input from vibrissal sensory afferents; (4) SpVmu interneurons project directly to lateral VIIm, which controls vibrissa movement; and (5) VIIm-projecting SpVmu neurons are primarily excitatory. While recent studies have elegantly characterized portions of sensorimotor circuits, such as premotor pools in spinal cord [Stepien et al., 2010] and brainstem (Takatoh et al., Neuron, in review), we are not aware of a study demonstrating connectivity throughout an entire circuit before the present work. Given the importance of low-level loops for fast sensorimotor behaviors [Kleinfeld et al., 1999], the results here are critical to constrain models of vibrissa sensory processing, circuit modulation, and motor output, and to drive studies of developmental sensorimotor circuit formation.

### 2.5.1 Trigeminal circuitry

#### 2.5.1.1 Implications of label intensity

The retrograde labeling of SpVmu cells from pseudorabies injections to the face was significantly stronger than that of other cells throughout the trigeminal brainstem. One possibility is that the tropism of the Bartha strain of PRV preferentially infects these synapses. However, retrograde labeling with FG confirmed stronger labeling in SpVmu than in other parts of Vbs (Fig. 2.11. The intensity of FG labeling may correlate with the density of terminal endings [Müller and Mestres, 2002], raising the intriguing possibility that SpVmu interneurons exert a strong influence on the activity of VIIm motoneurons relative to other trigeminal nuclei.

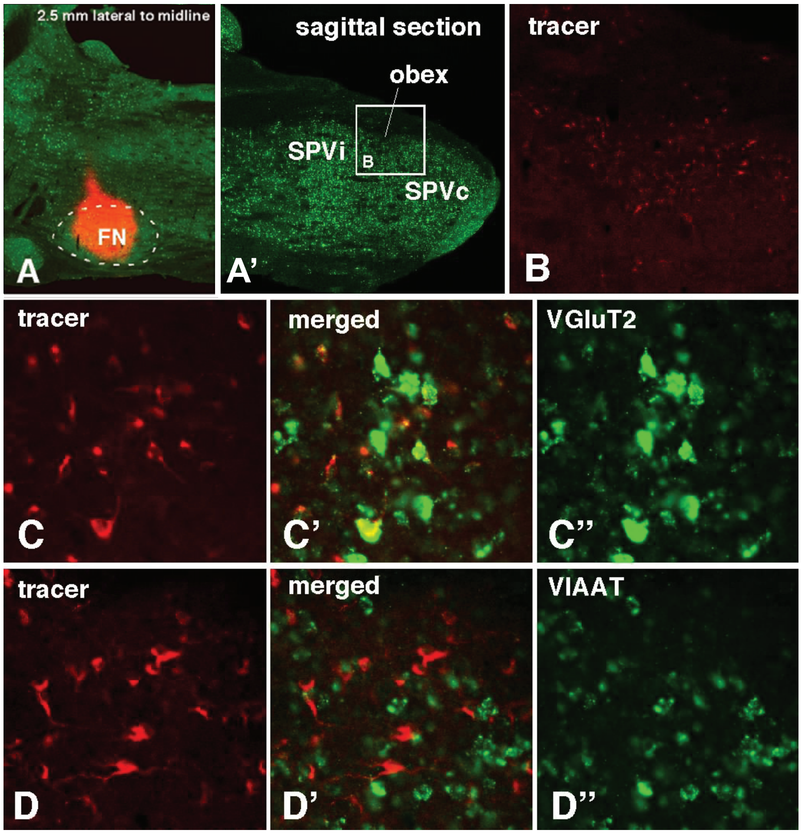

**Figure 2.17**: In situ *hybridization of retrogradely labeled SpVmu neurons.* (A) CTb was injected into rat VIIm for retrograde transport. (A') ISH probes labeled many cells throughout Vbs, but we focus our attention to the cells in SpVmu. (B) The tracer successfully labeled neurons retrogradely in SpVmu. Shown is the region in which we focus for the remaining panels. (C,C',C'') Results for VGluT2 probe. Many of the VIIm-projecting neurons were VGluT2 positive in SpVmu. (D,D',D'') Results for VIAAT probe. Most of the VIIm-projecting neurons we observed were VIAAT negative in SpVmu.

#### 2.5.1.2 Comparison with substantia gelatinosa

Substantia gelatinosa (SG), or Rexed lamina II, sits on the posterior edge of spinal cord. Some anatomical similarities between SpVc and SC have been described [Gobel et al., 1981] prompting some to adopt the term medullary dorsal horn in place of SpVc. In this scheme, the analog of spinal posterior laminae sits on the lateral edge of SpVc, and wrap medially toward PCRt as SpVc abuts SpVi. Two lines of evidence suggest that SpVmu is distinct from a putative SG analog. First, the cytoarchitecture of SpVmu does not show a gelatinous texture, due in part to the fact that there are still a large number of myelinated fibers in this region (see tissue refractility in Fig. 2.2). Second, the vast majority of Vg afferent endings and VIIm-projecting cells lie only in the rostral-most portion of SpVc (Figs. 2.9 and 2.10), demonstrating that, independent of morphological considerations, SpVmu does not explicitly fit the laminar structure of the proposed medullary dorsal horn schema.

#### 2.5.1.3 Organization of peripheral endings

Peripheral Vg endings include a multiplicity of receptor subtypes [Rice et al., 1997], send afferents to distinct locations in Vbs [Waite and Jacquin, 1992], and must convey different types of information to the larger vibrissa system, including vibrissa contact, phase, and possibly set point to be either received or computed downstream [Curtis and Kleinfeld, 2009]. Here, we do not distinguish between subpopulations of afferents as they terminate in SpVmu. However, it would be interesting to isolate discrete Vg subpopulations by adapting existing molecular tools [Hodge et al., 2007, Luo et al., 2009]. For example, one could express WGA-Cre in Merkel cell neurites and a Flex-XFP in VIIm motoneurons [Gradinaru et al., 2010] to ask whether synaptic specificity of Vg afferents in SpVmu constrains the type of sensory information used for fast sensorimotor behaviors.

#### 2.5.1.4 Relationship to blepharospasm

Eyeblink reflex circuitry mimics vibrissal trigeminofacial circuitry, where the maxillary inputs from vibrissae are exchanged for ophthalmic inputs from the eye [Holstege et al., 1986]. The fast positive feedback that has been demonstrated physiologically [Nguyen and Kleinfeld, 2005], and for which we now provide a circuit, is reminiscent of blepharospasm, a focal dystonia involving involuntary contraction of ocular musculature. From past evidence for eyeblink reflex anatomy [Schicatano et al., 1997] and because supraorbital injections do not terminate in SpVmu (Fig. 2.6, V1) this particular circuit can not mediate blepharospasm. However, the fast positive feedback circuitry demonstrated here and the matching time scales of blepharospasm and involuntary whisking [Dumitru, 1995, Filipkowski et al., 2001, Nguyen and Kleinfeld, 2005] raise the tantalizing possibility that a generic disynaptic architecture could mediate both normal and abnormally overactive trigeminofacial behaviors. It would be interesting to use the same approach here to evaluate the interneuronal pools that receive supraorbital Vg afferents, and project to VIIm motoneurons that control the orbicularis oculi muscle, with the aim of identifying the neurons potentially responsible for overdriving the eyeblink reflex in blepharospasm.

#### 2.5.1.5 Physiology of the Vg-SpVmu-VIIm circuit

The control of vibrissa movement during active, exploratory whisking involves a triphasic motor sequence with contributions from several muscles of the face, each innervated by VIIm motoneurons [Hill et al., 2008]; however, the upstream motor control of VIIm by premotor pools to generate such involved movements is not fully understood. The role that SpVmu neurons could play in low-level control of VIIm would be interesting to pursue [Nguyen and Kleinfeld, 2005]. For example, one could stimulate groups of SpVmu neurons extracellularly or single SpVmu neurons juxtacellularly and observe the effects on vibrissa movement. Because the region is small, we have shown that one could also label SpVmu neurons with a XFP-expressing retrograde virus, then record from SpVmu neurons targeted by fluorescence with a light-electrode probe [LeChasseur et al., 2011], or stimulate directly after locating SpVmu neurons. Stimulation experiments in anesthetized animals could reveal potential control over subsets of vibrissa musculature, and in awake animals could suggest insights for the control of active sensing.

### 2.5.2 Virus-based anatomy for behavior and physiology

Circuit tracing with molecular and viral strategies not only demonstrates monosynaptic connectivity between Vg afferents and SpVmu, but also provides data on the ratios of neurons in this pathway. This strategy thus not only circumvents the need for electron microscopy–in which double-label contrast agents and large spatial extent render scanning laborious–to confirm synaptic connectivity, but also improves on it, by providing long range, circuit-level data on the relative position and number of cells. In addition, viral circuit tracing makes functional studies possible on discrete neuronal subpopulations with known connectivity. This is especially important in the murine brainstem, where nuclear proximity and cellular diversity stymie efforts for well-controlled electrical or optogenetic manipulation. In the double-label AAV experiment we use, for example, replacing the Flex-reporter with a Flex-opsin would generate light-manipulable SpVmu neurons that necessarily receive peripheral sensory input and project directly to VIIm motoneurons. Interrogating the physiological and behavioral consequences of activating and silencing this discrete interneuronal population is therefore immediately accessible as a consequence of virus based circuit anatomy.

Interrogating the physiological and behavioral consequences of activating and silencing this discrete interneuronal population is therefore immediately accessible as a consequence of virus based circuit anatomy. Such manipulations would help to decipher the functional role of SpVmu neurons in the modulation of behavior.

### 2.5.3 Computational considerations

Anatomy constrains the computations that neural circuits can instantiate [Denk et al., 2012]. We demonstrate that the Vg-SpVmu-VIIm circuit has a feedforward architecture, whose range of computational properties are known [Rosenblatt, 1957]. However, we do not distinguish the connectivity of individually identified neurons. Renewed interest in large scale circuit reconstruction by electron and super-resolution microscopy has provided detailed wiring diagrams of complex circuits like the retina [Briggman et al., 2011], and may provide wiring diagrams of much larger brain systems [Lichtman and Sanes, 2008]. However, most mammalian nervous systems are still prohibitively large for reconstruction of all circuit elements by current methods [Denk et al., 2012]. The mono- and transsynaptic labeling that we image near the diffraction limit provides an intermediate solution: a wiring diagram at the sub-nuclear spatial scale, with confirmed synaptic connectivity, that surpasses the limitations of inferences made by classical point-to-point anatomy using traditional tracers. This delineation of a full sensorimotor circuit identifies a spatially tractable region of brainstem to prioritize for high resolution reconstruction.

*We thank Edward Callaway (The Salk Institute, CA) for the gift of glycoprotein-deleted rabies virus, Lynn Enquist (Princeton University, NJ) for the gift of pseudorabies virus, Karl Deisseroth (Stanford University, CA) for the gift of AAV-WGA-Cre, Agnieszka Brzozowska-Prechtl and Rodolfo Figueroa for help with histological processing, and Céline Matéo, Jeffrey Moore, and Andy Shih for helpful discussions. We acknowledge use of the UCSD Neuroscience Microscopy Shared Facility (Grant P30 NS047101). This chapter, in full, is a manuscript in preparation for submission. The dissertation author is the first author of this paper; though the full co-authorships have not yet been determined, they will likely include Takahiro Furuta, Fan Wang, Martin Deschênes, Harvey J. Karten, and David Kleinfeld.*

# Chapter 3

# The genomic organization of trigeminal brainstem using a histological atlas and statistical learning

## 3.1 Abstract

Brain development, organization, and function depend critically on the spatial localization of gene products. Many genes implicated in establishing and maintaining neuronal circuitry have been studied with molecular and developmental techniques, but the number of genes potentially involved in both regionalization and connectivity is enormous. The recent development of large-scale, spatially-registered gene expression databases now allows for the genome-wide evaluation of candidate genes important to regionalization. However, the development of digitized and registered projection data has lagged behind large-scale genomic projects, precluding analysis of the essential link between gene expression and connectivity in the brain. Here, we address the need for registered connectivity data by developing a micrometer-resolution brain image atlas for a subset of projections in the brainstem. We focus on connections between receptors in the facial skin and terminals in the trigeminal brainstem, because of the diversity and spatial segregation of inputs and the importance of this system as a developmental model. We next develop a method for co-registering this image database with a standardized, anatomical coordinate system used for spatially registered genomic data. Using this registered database, we apply statistical learning methods to identify individual and sets of genes that dominate expression in these well-defined regions of connectivity. We use unsupervised, dimensionality reduction techniques to determine whether gene expression correlates more with connectivity or with morphologically defined regions, and sparse supervised methods to identify particular genes that most strongly influence regional organization.

## 3.2 Introduction

Gene expression is essential to the structure and organization of the brain. During development, spatially distributed gene expression generates protein gradients and local cues that drive axon guidance and synapse formation [Polleux et al., 2007, Chédotal and Richards, 2010]. These gradients provide a molecular architecture within which long-range connectivity and local circuitry mature. Similarly, transcription factor and morphogen expression drives neuronal differentiation and the development of uniquely defined anatomical brain regions [Inan and Crair, 2007, Bishop, 2000]. Sensory experience further refines synaptic development and plasticity by way of gene regulation [Ressler et al., 2002], and the continued expression of proteins, such as Wnt receptors, into adulthood is required for neuronal survival even after development is complete [Liu et al., 2008]. Thus, gene expression remains critical for the continued maintenance of both circuits and regionalization in the brain throughout life.

Historically, study of the relationship between gene expression and brain connectivity and regionalization has focused on individual genes or gene sets using the tools of molecular biology. This work has provided important insights into the mechanisms of circuit formation [Polleux et al., 2007] and regional differentiation [Mallamaci et al., 2000, Shimogori et al., 2004]; however, the techniques limit research to a small fraction of the possible number of genes available for organization. Recently, several independent, large-scale efforts have been undertaken to quantitatively describe and digitally represent brain anatomy, genome-wide expression patterns, and, to a lesser extent, large-scale projection patterns, using the mouse as a model system. With respect to brain anatomy, mouse brain atlases have been generated using developments in automated imaging, computational, and registration techniques [MacKenzie-Graham et al., 2004, Hawrylycz et al., 2011]. With respect to genetic expression, several spatially-registered, genome-wide atlases are now publicly available, which map images of serially scanned brain sections prepared using *in situ* hybridization (ISH) to, for example, a canonical embryonic mouse atlas (Edinburgh Mouse Atlas of Gene Expression; EMAGE) [Christiansen et al., 2006, Richardson et al., 2010, Armit et al., 2012], or an adult mouse atlas (Allen Gene Expression Atlas; AGEA) [Lein et al., 2007, Jones et al., 2009]. Finally, there is deep interest in identifying the set of all gross projection patterns within the brain and incorporating them into a standardized mouse brain atlas [Kasthuri and Lichtman, 2007, Bohland et al., 2009]; however, the industry-scale undertaking of defining a whole mouse brain connectivity map, with at least the resolution used in genome-wide expression studies, has not yet been realized.

The combination of gene expression, connectivity, and morphological data provide a novel opportunity to evaluate the genetic and anatomical structure of the brain at a genome-wide level. Past work has circumvented the paucity of available connectivity data in mouse with both computational and anatomical approaches. Computationally, ontological data has been culled from publicly available connectivity databases, e.g. [Bota et al., 2005]. While this strategy has been fruitful [Wolf et al., 2011, French et al., 2011, French and Pavlidis, 2011], the databases are (1) typically text-based, thus providing only high-level associations between regions rather than detailed, image-based connectivity maps, and (2) not fully populated, requiring researchers to use different model systems for analysis across data sets, e.g. rat connectivity with mouse genomics data. The second approach has focused on anatomically related portions of the brain with the goal of inferring connectivity from genomic analysis; this strategy has been applied, in particular, to the study of the hippocampus, in which subdomains of CA1 and CA3 are genetically distinct, and correlate with known cell-specific differences in connectivity [Thompson et al., 2008, Dong et al., 2009]. However, in these studies, results from connectivity are used *ex post facto* as confirmation of the area differences found by genomic analysis, rather than to uncover genetic structure directly from connectivity.

Additionally, most studies using spatially registered transcription data of the mouse brain have focused on spatial correlations across many genes. Such work has revealed potential brain-wide parcellation schemes that fit with a comparative anatomical understanding of neural organization [Bohland et al., 2010]; region-specific parcellations of functional domains with unique genetic and anatomical features [Dong et al., 2009]; divisions of thalamic development [Price et al., 2012]; and association-rule based expression patterns [Hemert and Baldock, 2007]. However, in one case, statistical methods that focus on small sets of genes have been developed [Grange and Mitra, 2011]. Despite the theoretical focus on large sets of genes to evaluate brain region differences, analysis and predictions regarding sparse numbers of genes influencing organization would both fit with past molecular studies and provide biologically tractable experiments for validation.

The availability of large-scale genomic data and the possibility that individual or small sets of genes may be important to local brain organization underscore the importance of developing databases of connections for direct comparison with genomic expression data. But with so many connections in the brain, where does one begin? The brainstem is a powerful model system for analyzing long range connectivity and gene expression because much of its volume is dominated by primary sensory afferents that innervate peripheral target organs and motor efferents that innervate peripheral musculature. The trigeminal brainstem, in particular, is an ideal starting point for evaluating genetic organization because it (1) covers a large relative spatial extent in mouse, (2) contains discrete afferents from multiple nerve branches that project to many regions of the face, and (3) has a well-defined set of nuclei in which central terminations end [Erzurumlu et al., 2010]. Additionally, trigeminal brainstem has an organized set of somatotopic maps corresponding to the vibrissae of the face [Ma, 1991], which has renewed interest in its use as a developmental genetics model system [Hodge et al., 2007, Erzurumlu et al., 2010]. The overlapping but independent maps of projections and anatomy provide an excellent anatomical framework for understanding genetic organization.

Here, we use the trigeminal brainstem as a model for local genetic organization of projections and nuclei. Using targeted microinjections of an axonal tracer, we first develop a micrometer-resolution brain image atlas showing the many connections between receptors in the facial skin and the trigeminal brainstem. We next develop a method for registering this image database with a standardized coordinate system used for spatially registered genomic data. Finally, we apply unsupervised and supervised machine learning methods to identify individual and sets of genes that uniquely dominate expression in these well-defined regions. In particular, we ask whether gene expression correlates more with projections or with anatomically defined regions of the trigeminal brainstem, and whether particular genes strongly influence the organization of these regions.

## 3.3 Methods

For this study, we use two large mouse brain data sets: (1) a publicly available set of registered gene transcript profiles, and (2) a histological database of central trigeminal projection patterns that we collected from age- and sex-matched mice.

### 3.3.1 Gene expression data from Allen Brain Atlas

The first data set, the Allen Brain Atlas (ABA; http://mouse.brain-map.org/) is a database of three dimensional expression profiles for ~20,000 genes throughout the brain of 56-day old male C57BL/6 mice [Lein et al., 2007]. Briefly, the data are derived from automated application of non-isotopic *in situ* hybridization (ISH) [Visel et al., 2004] with custom designed probes, on average 800 nucleotides long, on sequential brain slices, which are imaged with cellular-resolution image scanners and evaluated for spatially localized signal intensity with informatics and image processing techniques [Ng et al., 2007]. The genome-wide data are from non-consecutive sagittal slices of 25 $\mu m$ thickness for a given probe. Image data for each probe was co-registered in three dimensions using an anatomical atlas of Nissl stained sections, called the Allen Reference Atlas (ARA) [Dong, 2008]. This atlas also includes 232 annotations of brain regions, to one of which each voxel is assigned according to the coregistration process. The registered image data were divided into uniform 200 $\mu m$ voxels, of which the expression for a given probe was assigned from the average ISH signal intensity, or *smoothed expression energy* [Lein et al., 2007], in the relevant unprocessed ISH image and interpolated where necessary. The resulting, registered, 200 $\mu m$ voxel resolution set of expression values across primarily one hemisphere of the brain is a $67 \times 41 \times 58$ (rostrocaudal, dorsoventral, and left-right) voxel three dimensional space, where each voxel contains a $\sim 20,000$ dimensional vector of expression values (Fig. 3.1). We organized these final registered values from $\sim 30,000$ text files representing individual genes, accessed through the ABA application programming interface (API) using a custom written Python script (kindly provided by B. Shanks, Salk Institute).

### 3.3.2 Development of histological data

The second data set is derived from a library of peripheral injections we generated. Twenty-five C57BL/6 adult male mice (aged 56 days or more) were anesthetized with inhalation isoflurane (0.5-2% in $O_2$, depending on weight and response). Cholera toxin subunit B (0.5-1% CTb; List laboratories, #103B; Campbell, CA) [Angelucci et al., 1996] was injected in the skin and in trigeminal ganglion using different methods.

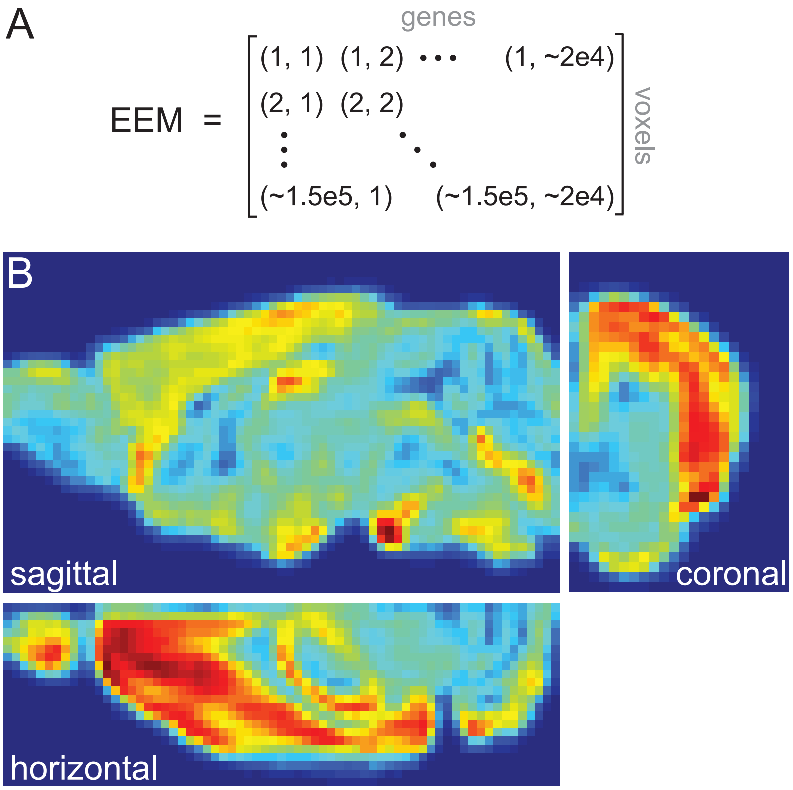

**Figure 3.1**: *Expression energy matrix and voxel representation.*
(A) Expression energies (see 3.3.1) are organized by voxel and gene, in a matrix of values for all analysis. (B) An example set of sections in the three standard histological frames. Expression has been summed across 100 random genes, and shows different intensities according to regional boundaries, particularly in cortex and pons.

For peripheral nerve labeling, CTb was injected subcutaneously and unilaterally on the left hemisection of the face into one or more known terminal branching zones of one of the three branches of the trigeminal nerve. Injections were made with a 10 $\mu$L Hamilton syringe (Hamilton Company, Reno, NV) coupled to tubing and a 30-gauge injection needle. For full trigeminal ganglion labeling, the mouse was positioned in a stereotaxic instrument (M900, Kopf), and a $\sim 2 \times 2$ mm craniotomy was centered at 1.5 mm rostral to bregma and 1.7 mm left of the midline. In some cases (8 of 15), vibrissa-responsive cells in trigeminal ganglion (Vg) were located by manual mechanical stimulation of the ipsilateral vibrissae while extracellular recording in Vg with a thin tip diameter ($\sim$10 $\mu$m) quartz pipette filled with 0.5 M NaCl, amplified (Axoclamp 900A; Molecular Devices, Sunnyvale, CA) and observed on an oscilloscope (Tektronix TDS 224) and audio speaker. Vg vibrissa-responsive cell locations in the maxillary branch were consistent relative to stereotaxic coordinates, precluding the need to record in all animals. A thin quartz injection pipette (0.6 mm ID, 1.0 mm OD, pulled to $\sim$20 $\mu$m tip on P-2000, Sutter Instrument, Novato, CA) was advanced to 5.7 - 6.0 mm below the surface, or the precise location of maximal vibrissa responses, with a micrometer-resolution manipulator (MPC-200, Sutter Instrument), and $\sim$80-400 nL of 0.5 or 1% CTb was injected by pressure using a custom circuit triggered by a pulse generator (Grass S48 stimulator). In another series of injections, a larger ($\sim 4 \times 4$ mm) craniotomy was performed, the dura across the entire exposed extent of the brain was removed with a dural hook, and a crystal of sodium nitrate ($AgNO_3$) was gently pressed into the cortex and subcortical white matter and allowed to solubilize for 10-15 min to effectively cauterize the tissue. The cortical and subcortical tissue overlaying the left Vg was carefully excavated with vacuum pressure to reveal the Vg. For the tissue below the volume effected by sodium nitrate treatment, excess bleeding was inhibited then eliminated using gelfoam and repeated saline bath. A quartz electrode was lowered into the Vg and 100 - 300 nL of CTB was injected in stages, followed by a waiting period of 5-30 min. Animals were supplemented with up to 1 mm of lactated ringer before recovering from the anesthetic state.

Following a survival time of 3 - 10 d, mice were deeply anesthetized with inhalation isoflurane (3-4%) followed by intraperitoneal injection of 100-200 $\mu$L pentobarbital (Fatal Plus), transcardially perfused with phosphate-buffered saline followed by 4% paraformaldehyde in 0.1 M phosphate-buffered saline (PBS), pH 7.4. After removal from the skull and at least three hours of 4% PFA exposure, the brain, trigeminal ganglion and nerve, and facial skin were each cryoprotected in 30% w/v sucrose in 0.1 M PBS, and sectioned on a freezing microtome. Brain and upper cervical spinal cord were serially sectioned at 30 $\mu$m in one of three standard stereotaxic planes (sagittal, transverse, and horizontal). Sequential brain sections were treated with Nissl stain (Cresyl violet acetate, Sigma C 5042), Giemsa (Original Azure Stain, WVR 15204-144), and Goat anti-cholera toxin primary antibody (1:12,000, List laboratories, Cat. #703) followed by rabbit anti-goat IgG (1:200, Vector Company #BA-5000) and 0.025 mg/mL DAB solution (Sigma D-5637). Face and ganglion sections, where treated, were prepared similarly. Sections were mounted, dehydrated in ascending alcohols, delipidized in xylenes, and cover-slipped with Cytoseal 60 (Fisher Scientific NC952739). Animal care and treatment conformed to the National Institutes of Health Guidelines and were approved by the Institutional Animal Care and Use at University of California, San Diego. Some of these data were also used in chapter 2 on disynaptic circuitry in trigeminal brainstem; we focus on peripheral injections in this chapter.

### 3.3.3 Imaging and digitization

Slides were imaged serially and automatically using a whole-slide imaging scanner (NanoZoomer 2.0-HT, Hamamatsu Photonics, Japan) at 0.453 $\mu\mathrm{m/pixel}$ resolution under a 20× objective (0.75 NA, Olympus) under illumination from a 200 W mercury lamp. This system uses line scanning of a 3-channel time-delay integrated sensor to resolve brightfield images at $\sim 5-20$ min per slide. The file format, Hamamatsu Nanozoomer Digital Pathology Image (NDPI), is proprietary. The encoded JPG files were extracted per section, either manually or automatically using custom software (NDPIchop, Steve Lamont, NCMIR) and downsampled for ease of processing. Each slice was then traced either manually or semi-automatically, and CTb labeling was identified and traced using Neurolucida (MicroBrightField, Inc., Williston, VT) according to the intensity of the DAB reaction against anti-CTb. Brain traces were oriented in the z-axis, and coarsely registered in Neurolucida, then exported as XML files for image analysis (Fig. 3.2). Reconstructed volumes, showing the relative positions of the three divisions of trigeminal branch afferents, were generated for each test case before subsequent co-registration stages (Fig. 3.3).

### 3.3.4 Co-registration of histological data with Allen Brain Atlas

Registration and alignment are necessary steps for generating a voxel-based training set from different sections and different subjects (AGEA, INCF), due to individual variation, experimental differences, and tissue warpage. There are many approaches to the automated or semi-automated registration of histological sections to a three dimensional reference framework or canonical atlas space. Also, the tools for registration are developing rapidly, but these are often designed for particular animals, such as P7 mice [Ju et al., 2006,Carson et al., 2010] or require substantial computational processing and parameter exploration [Ng et al., 2007].

After assessing existing software, we built a custom suite of tools in MATLAB (Mathworks; Natick, MA) for aligning all brain slices to the Allen Brain Atlas (ABA) database. We aimed to generate software that minimized computational processing and dependence on tunable parameters, with the tradeoff that more anatomical expert knowledge was expected of the end user. The software parses Neurolucida XML files and generates contours representing the whole brain, lightly-stained, and darkly-stained region boundaries, or any other contour definitions used in tracing the original data. The software prompts the user to compare against the Allen Reference Atlas (ARA), using knowledge of anatomical landmarks, to identify the matching Z dimensions (e.g. in sagittal, the Z dimension is the mediolateral axis), then provides a tool for per-section affine transformation–that is, individual rotation, translation, and dilation–to best match the ARA, with primary emphasis on registration of the brainstem. When the user has completed per-section transformations, the software converts all contours to solid masks of labeled regions fit to the voxel-based ABA data (Fig. 3.4). The software is applicable generally for registration of any Neurolucida output files, can be used for non-brainstem alignment, and is currently maintained in an online subversion repository and freely available by contacting the author.

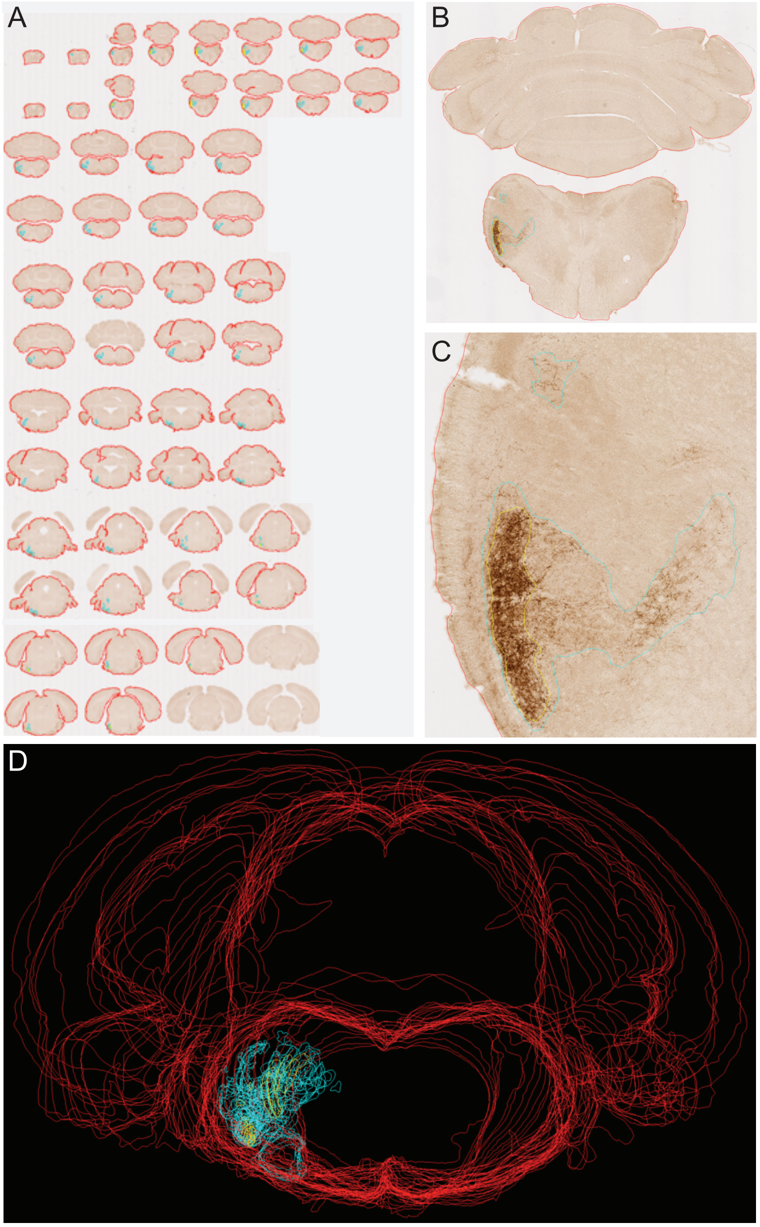

**Figure 3.2**: *Semi-automatic tracing in Neurolucida.*
(A-C) Serially sectioned and imaged brain tissue is manually or automatically contoured, and the DAB reaction product is manually outlined per section. (D) Sections are arranged in three dimensions and manually co-registered.

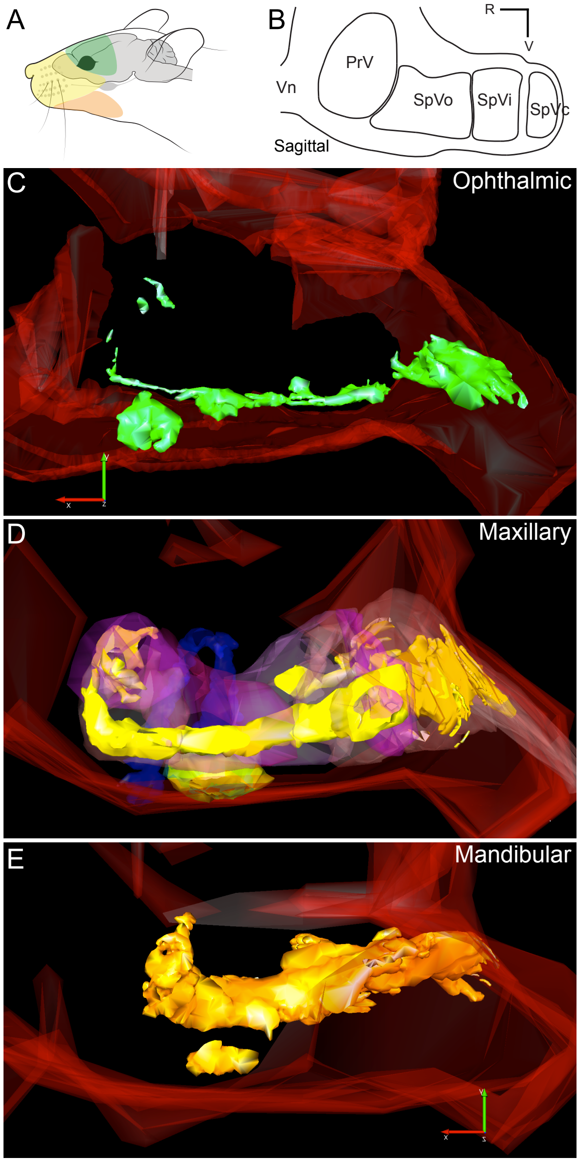

**Figure 3.3**: *Reconstructed volumes of trigeminal branch afferents.*
(A) Schematic of peripheral innervation zones for each of the trigeminal branches (ophthalmic, green; maxillary, yellow; mandibular, orange). (B) Schematic of the trigeminal brainstem nuclei in a sagittal orientation, showing the primary nuclei, principalis (PrV), oralis (SpVo), interpolaris (SpVi), and caudalis (SpVc), as in figure 2.1. (C-E) Representative reconstructed volumes of maxillary (C), ophthalmic (D), and mandibular (E) projection locations in trigeminal brainstem. Trigeminal nuclei boundaries are superimposed in panel D (magenta); brain outlines are in red.

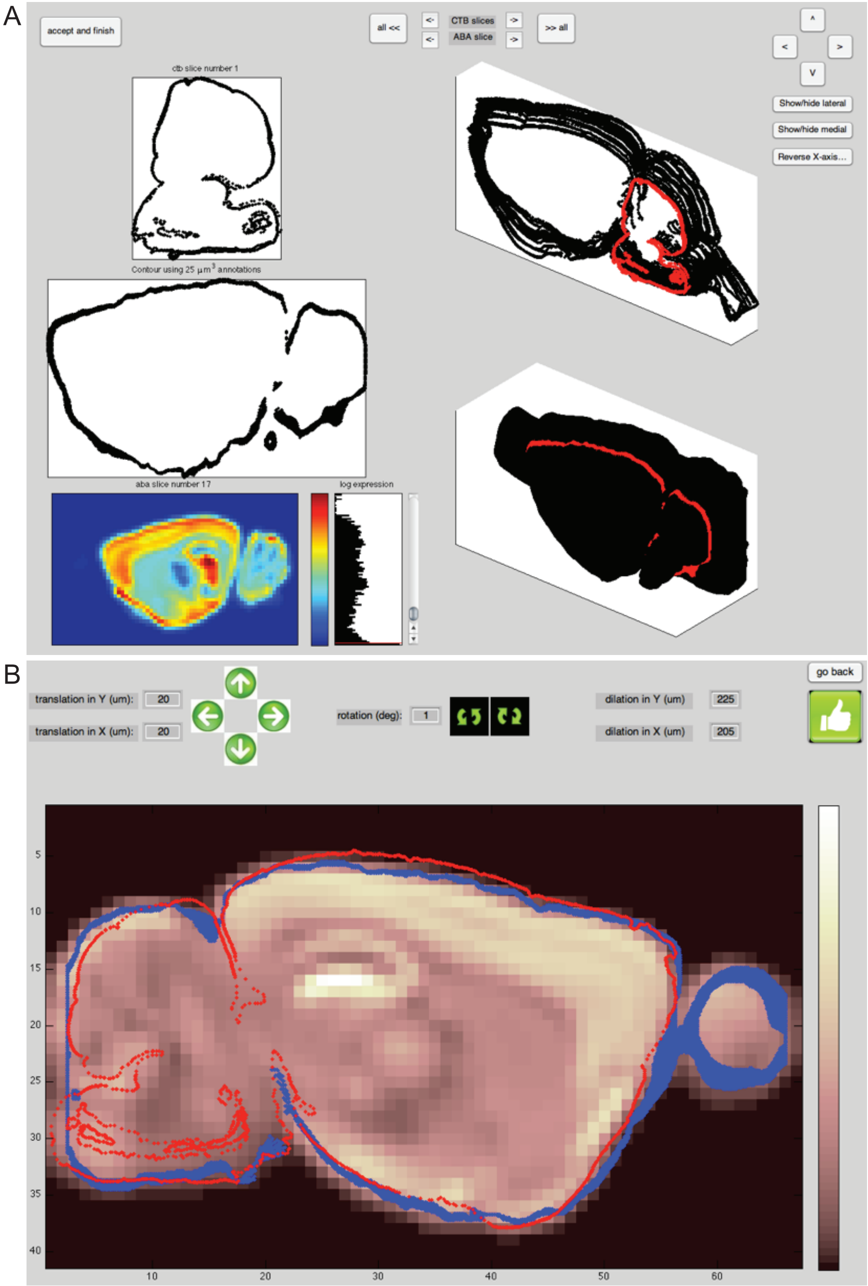

translation in Y (um): 20

translation in X (um): 20

rotation (deg): 1

dilation in Y (um) 225

dilation in X (um) 205

**Figure 3.4**: *Semi-automatic co-registration with Allen database*. (A) Histological sections are aligned in the Z dimension to the ABA. (B) Affine transformations are then applied per section, prioritizing brainstem co-registration. See section 3.3.4 for details.

## 3.4 Results

We generated a projection database of peripheral inputs to the trigeminal brainstem, in the form of serial primary images and reconstructed volumes (see Sec. 3.3 and Fig. 3.3), and co-registered these with a database of genome-wide gene expression. We now analyze statistical relationships between these two databases.

### 3.4.1 Projection versus regional gene expression

We first asked whether gene expression is better correlated with the pattern of inputs or with the regional boundaries of trigeminal brainstem. We used two unsupervised learning techniques to address this question of overall genetic structure.

#### 3.4.1.1 Principal components analysis of brainstem and trigeminal EEMs

We applied principal component analysis (PCA) to orthogonalize the expression energy matrix into a basis set of linearly uncorrelated vectors. We computed the eigenvalues of the covariance matrix for the subset of voxels of the EEM that are contained in the brainstem ($\sim 6000$). Voxels from each of the four primary nuclei of the trigeminal brainstem–principal nucleus, spinal oralis, spinal interpolaris, and spinal caudalis–tended to show similar within-group and between-group gene expression eigenvalues (Fig. 3.5). In particular, when the gene expression for each voxel is projected into the three dimensional principal component space generated from the three eigenvectors that explain the most variance in the data, the voxels tend to cluster in a subsection of the space of all brainstem voxels (Fig. 3.5). Similarly, voxels from each of the three subdivisions of trigeminal inputs–maxillary, mandibular, and ophthalmic also tended to cluster (Fig. 3.6). This suggests that both groupings, by inputs and by nuclei, show increased genetic similarity.

In order to quantify the genetic variability of voxels in each group (nuclei and inputs), we used a similarity metric based on Euclidean distance in principal component space,

$$D_E(\vec{x},\vec{y}) = \sqrt{\sum_{i=1}^{n}(x_i - y_i)^2}, \tag{3.1}$$

where $\vec{x}$ and $\vec{y}$ are vectors of $n$ “eigen-genes” from the same group. We computed this distance for voxels in all groups (Fig. 3.7). We found that voxels within groups are, in general, twice as close genetically as random voxels in brainstem, according to this metric. Additionally, voxels particularly within groups defined anatomically versus those defined by projections are not significantly different. Voxels in principal nucleus are more genetically similar than those in the rest of the groups. This result is consistent with the more homogeneous morphology found in principal nucleus. Meanwhile, the caudal nucleus shows the least genetic similarity among canonical trigeminal nuclei. This dissimilarity is consistent with the greater heterogeneity in caudal nucleus, which is essentially a medullary dorsal horn containing layers similar to those of Rexed in the spinal cord [Gobel et al., 1981]. The regions labeled strongly with CTb–locations in trigeminal brainstem that receive dense input from the maxillary periphery–tend to be more genetically similar than that for both weakly and strongly labeled regions, which suggests greater genetic homogeneity in the terminal zones of peripheral inputs; however, the effect is small. Finally, the ARA annotations of “supratrigeminal” and “brain stem” are closer to random, possibly because the “supratrigeminal” is ill-defined in most atlases, and the “brain stem” represents voxels that were otherwise not included in specific annotations of brainstem nuclei.

#### 3.4.1.2 Non-negative matrix factorization of trigeminal EEM

PCA is a useful general tool for capturing and visualizing the global variance of a data set. However, because PCA represents the original data matrix with weights that can take negative values, it is not best suited to describing gene expression, which cannot, by definition, be negative. To overcome this issue, we used a second dimensionality reduction technique called non-negative matrix factorization (NMF). NMF provides a low-rank approximation of the feature space by factorizing the original matrix (EEM) into two matrices $W$ an $H$ [Lee and Seung, 1999]. Here, the factorization involves minimizing the root mean square residual EEM $-WH$, subject to the constraint that all values of $W$ and $H$ are nonnegative. While the dimensions of EEM are large (voxels $\times$

genes), the factorization into basis vectors of W (voxels × $k$) and encodings of H ($k$ × genes) is compressed by the parameter $k$.

We used NMF to factorize the EEM composed of voxels within the trigeminal brainstem for a range of values for parameter $k$ (Fig. 3.8). Because the columns of $W$ are basis vectors for gene encodings and tend to be sparse representations of features in the data [Lee and Seung, 1999], we examined the dominant basis vector for each voxel in trigeminal brainstem (Fig. 3.8A). Complementary to the results with PCA, the basis vector that best captures the genetic expression profile for a given voxel tended to be the same for neighboring voxels (Fig. 3.8B). Interestingly, these clusters roughly correspond to locations within trigeminal brainstem associated with both afferent inputs and with nuclear divisions. For example, basis vector 6 corresponds to the location of spinal nucleus oralis, and does not appear in other nuclei, except part of caudal principalis. This correspondence held true for a range of values of the parameter $k$.

If a particular number of genetically distinct regions exists in the EEM, we reasoned that the residual error should decrease significantly when that number of basis vectors is used to factorize the EEM. Because we are interested in uncovering whether such putative regions match inputs or nuclei, we examined the decrease in the residual over a range of the parameter $k$, which sets the number of basis vectors in $W$ (Fig. 3.8B). However, the residual slowly and monotonically decays with increasing $k$, suggesting that a particular number of regions, based on inputs or nuclei, is not apparent using this method.

#### 3.4.1.3 Highly explanatory genes from unsupervised learning methods

PCA and NMF exploit different approaches to reduce the dimensionality of a matrix; however, they both provide a set of basis vectors composed of linear combinations of the original data matrix. The contribution of individual genes to the composition of the basis vectors varies, and particular genes that contribute largely to important basis vectors may hold significance for a genetic organization of voxels in the EEM. We therefore identified those genes that contributed greatest to basis vectors when PCA and NMF were computed specifically for the trigeminal EEM. We show results for the first principal component, where the contribution of a particular gene is taken from the entries of the first column of the coefficient matrix. We compare these with results for the most dominant basis vector in the $W$ matrix from NMF, defined as the basis vector that most closely resembles the genetic expression profile (as in Fig. 3.8A) for the most voxels (basis vector 6 in Fig. 3.9); gene contributions are defined by the coefficients of the row of the $H$ matrix corresponding to the column of the dominant $W$ basis vector. The normalized contribution of each gene is small, but strikingly similar across the two methods (Fig. 3.9). In fact, 20 of the 25 most contributing genes for PCA are among the top 25 most contributing genes for NMF (Fig. 3.9). Given the fact that the database includes $\sim$20,000 genes, this correspondence suggests that certain genes play a substantially greater role in organization than others. Additionally, many of these genes, and those contributing most to other dominant modes of both PCA and NMF (not shown), play important roles in neuronal organization, including CNS development (*Tuba1*; alpha tubulin 1), axon formation (*Neu3*; neuraminidase 3), neurite outgrowth (*Gapdh*; glyceraldehyde-3-phosphate dehydrogenase), mitochondrial docking in axons (*Dynll2*; dynein light chain LC8-type 2), and synaptic fusion (*Nsf*; N-methylmaleimide selective fusion protein). While we examined many other results from these unsupervised analyses not shown here, we next describe a complementary set of analyses to examine the role of individual genes for defining trigeminal regions, motivated by the consistency of results from PCA and NMF suggesting single genes' roles in organization.

### 3.4.2 A sparse genetic code may underlie trigeminal organization

We have so far examined the role of all genes on the organization of trigeminal brainstem. However, the relative weight of individual genes to dominant basis vectors in these analyses raises the possibility that certain genes are much more responsible for organization than others. Therefore, we next ask whether a small set of genes is sufficient to predict the projections to and nuclei within the trigeminal brainstem.

#### 3.4.2.1 Decision tree learning with individual genes

Supervised machine learning methods are ideal for this goal of associating a set of inputs (genes) with a set of outputs (membership in a regional class, such as principal nucleus) by inferring a function relating the sets. Because we are interested in whether individual genes are sufficient to predict class membership, we employ a classification algorithm called decision tree learning, which is frequently used in bioinformatics [Kingsford and Salzberg, 2008] and well suited to identifying highly predictive inputs. When applied to this problem of spatially organized gene expression, decision tree classification partitions the high dimensional gene space by recursively identifying the gene and its expression threshold that best classifies voxels according to membership in the class of interest. "Best" is defined as the maximal change in information, $I_{\text{gained}}$, before and after partitioning:

$$I_{\text{gained}} = \zeta(\text{trunk}) - \sum_{c}(p_c)\zeta(\text{branch}_c), \tag{3.2}$$

where "trunk" is the gene space before partitioning and "branch" is the subspace after partitioning, $p_c$ is the proportion of voxels in class $c$, and $\zeta(\cdot)$ is a scoring criterion. We use two different scoring criteria, producing qualitatively similar results, based on either information,

$$\zeta_H(f) = -\sum_{c} \frac{V_c(n)}{V(n)} \log_2\left(\frac{V_c(n)}{V(n)}\right), \tag{3.3}$$

or Gini impurity,

$$\zeta_G(f) = 1 - \sum_{c} \left\| p(c)\frac{V_c(n)}{V(n)} \right\|^2, \tag{3.4}$$

where $f$ is the gene subspace, $V$ is the number of voxels, $n$ is the node, and $\|\cdot\|$ is a unit length normalization. For the Gini impurity, $p(c)$ is a proportional prior, $p(c) = \frac{V_c}{V_{total}}$.

Intuitively, this algorithm thus finds the gene and expression threshold to separate voxels that are correctly assigned to one of two classes (e.g., inside or outside of a given nucleus), then recursively repeats this procedure in the partitioned gene subspace until all of the voxels are classified correctly (or it satisfies other stopping criteria).

#### 3.4.2.2 Feature selection using conservative criteria

Before implementing the decision tree algorithm, we evaluated all of the gene expression profiles to select a subset that were relevant to the trigeminal brainstem. This preprocessing stage removed genes based on complete lack or homogeneity of expression in the region of interest, and was important for the sake of computation time and statistical significance considerations. To reduce the set of genes to study, we generated a set of reasonable criteria based on first and second statistical moments of the expression distributions, using conservative thresholds:

$$\mu_{\text{trigeminus}} > 0.1 \tag{3.5}$$

$$\mu_{\text{trigeminus}} / \mu_{\text{brainstem}} > 1 \tag{3.6}$$

$$\mu_{\text{trigeminus}} - \mu_{\text{brainstem}} > 0.25 \tag{3.7}$$

$$\sigma^2_{\text{trigeminus}} > 1 \tag{3.8}$$

$$\sigma_{\text{trigeminus}} / \mu_{\text{trigeminus}} > 1, \tag{3.9}$$

where $\mu$ is the mean expression energy of defined voxels, $\sigma^2$ is the variance in expression energy of defined voxels, "trigeminus" includes all voxels defined within trigeminal brainstem, and "brainstem" includes all voxels with brainstem membership annotations, not including "trigeminus". Requiring each gene to satisfy all of these criteria reduced the number of genes from $\sim 20,000$ to 902. Every gene, sorted by performance on each of these criteria, is plotted on a linear scale with normalized criterion values (Fig. 3.10A) and a logarithmic scale with original criterion values (Fig. 3.10B). Genes with expression profiles that failed at least one of these metrics were discarded from analysis with decision trees.

Additionally, because we are interested specifically in trigeminal structure, we restrict our exploration of genes to the voxels that are within or near the trigeminal brainstem. We use the ARA annotations and the co-registered trigeminal input data to determine voxels of interest, numbering $\sim 600$ in total, which represents $\sim 10\%$ of all brainstem voxels.

#### 3.4.2.3 Classification of nuclei by decision tree learning

Having selected sets of genes that are most relevant to the trigeminal brainstem according to the preprocessing criteria, we are ready to conduct the supervised learning experiment. The data are limited to one instance of gene expression per voxel; generating training and test data sets would sacrifice much of the data, and there is no independent, quantified data set currently available with which to compare the results. Therefore, we use *k*-fold cross validation, in which the algorithm runs many times, holding out a portion of the data at random for each run, and determines how well the optimal tree generalizes to this nominally independent data.

First, we evaluated each of the four trigeminal brainstem nuclei–principalis, oralis, interpolaris, and caudalis–compared against all other portions of trigeminal brainstem. For each nucleus, a decision tree was generated that classified voxels according to the thresholded expression of genes. Strikingly, each of the trees successfully classified voxels into nuclei within just a few branches (Fig. 3.11). The small branching of these trees shows that only a few genes, when thresholded appropriately, are necessary to correctly classify virtually all of the voxels (see Sec. 3.5).

The expression of genes highlighted by this analysis shows local structure corresponding to parts of the trigeminal brainstem. For example, the gene for HoxA5, one of the family of Homeobox proteins important for body patterning during development [Brunet et al., 2007], shows high expression discretely in caudal portions of trigeminal brainstem (Fig. 3.12A). To better visualize gene expression corresponding to trigeminal brainstem regions, we mapped the three dimensional voxel space to two dimensions such that local distances among voxels are roughly preserved. From this two dimensional perspective, the intense, local expression is clear in caudal trigeminal brainstem (Fig. 3.12B). Because there is significant image processing in proceeding from serial images of ISH sections to the final matrix of gene expression values (see 3.3.1), we also confirmed by evaluating the original image data for a portion of the results. A sagittal section of *Hoxa5* cut in the plane of trigeminal brainstem shows that expression is high in the caudal divisions of trigeminal brainstem, and absent in the rostral divisions (Fig. 3.12C). The consistency of this example gene was recapitulated in many of the genes used for classification by decision trees, suggesting that their robust and localized expression could be related to the nuclear organization of trigeminal brainstem.

#### 3.4.2.4 Classification of terminal regions by decision tree learning

Using the same feature selection criteria for genes, we also trained decision tree classifiers for each of the three regions of brainstem innervated by trigeminal afferents. Using the co-registered histological data from multiple injections into the three branches of the trigeminal nerve, we constructed three classes of voxels receiving inputs. In principle, the three trigeminal branches could terminate in overlapping regions of the brainstem; in practice, however, the three branches tend to terminate in unique regions, roughly organized along the dorsoventral axis [Bregmann, 1892, Åström, 1953, Torvik, 1956, Kerr, 1963]. We treated each projection independently, and trained decision tree classifiers for each, comparing the class of voxels for a given projection with that from the rest of trigeminal brainstem and surrounding voxels. The decision trees representing the results from each of the projections are shown in figure 3.13. These trees required more branch nodes to correctly classify voxels, as compared to trees for the nuclei divisions. However, when only the two or first three levels of the tree were used for classification, voxels were correctly labeled in most cases. As an example, the performance for classification of the maxillary division of the trigeminal brainstem is shown in figure 3.14. Adjacent sections of the six voxelized sagittal slices containing maxillary voxels are shown as backdrop to the classification results. 210 (70.2%) of the brainstem voxels were correctly classified as maxillary (green), while 64 (21.4%) were classified incorrectly as maxillary (red), and 25 (8.4%) were classified incorrectly as *not* maxillary. This performance is surprising given the spatial extent of the maxillary representation across the entire pons and medulla, from principalis to caudalis nuclei. Interestingly, the classification errors occurred almost exclusively on the edges of the maxillary division, where the afferent input tends to be least robust. Most strikingly, for any given branch, only a few genes from the original database of $\sim 20,000$ genes are sufficient to classify the majority of voxels in all of the nuclei and branching regions studied.

### 3.4.3 Independent validation: GENSAT BAC image database

Results from an informatics study should be verified against independent data; however, no digitized, genome-wide adult mouse gene expression data similar to the ABA is currently available (see Sec. 3.5). Therefore, we compared highly informative genes from the above analyses with images from an independent database derived from bacterial artificial chromosome (BAC) vectors and transgenic mouse lines (GENSAT Brain Atlas of Gene Expression, [Gong et al., 2003]). We found $\sim 2/3$ of the explanatory genes from our dataset cross-referenced in the GENSAT SQL database. Inspection of a subset of these images revealed many consistent patterns of expression localized to regions of trigeminal brainstem in both adult and postnatal mice (Fig. 3.15). In particular, several genes strongly delineated boundaries and subregions within the caudalis and interpolaris nuclei. For example, in adult tissue, *Hoxa5* and *Rasgrp1* show discrete patterns in outer layers of caudalis, and *Cck* shows sparse and local expression in the inner portion of caudalis. Strikingly, *Nsf* shows strong expression exclusively in caudal interpolaris. In postnatal day 7 tissue, *Cck* shows prominent expression throughout caudalis, and *Rasgrp1* throughout all of trigeminus, but especially in interpolaris and the mandibular division of trigeminus. Perhaps most interesting in light of the findings from chapter 2, *Nrgn* is expressed strongly in oralis and discretely in muralis. This correspondence with image data obtained using an independent genetic strategy confirms the relevance of these genes for trigeminal organization.

## 3.5 Discussion

We have generated a projection atlas of the afferents to mouse trigeminal brainstem, developed a method to co-register this atlas with a large-scale genomics database, and analyzed the two datasets using statistical learning methods to identify regions and genes of particular relevance to this part of the brainstem.

### 3.5.1 Trigeminal projection database

The development of large-scale, digitally indexed, and spatially registered databases of connectivity has lagged behind that of genome-wide genetic expression in the mammalian brain, and well behind the sequencing of genomes [Kasthuri and Lichtman, 2007, Lichtman and Sanes, 2008, Bohland et al., 2009]. Generating projection databases presents significant challenges for automation due to the expertise required for local stereotaxic injections and live mouse experimentation; however, this endeavor is essential for fully understanding, modeling, and, ultimately, manipulating the fundamental substrate underlying neural computations. In light of the challenges of automation, we manually generated a complete dataset for a portion of the brain. Because the targeted injection locations are primarily in the periphery, these connections are unlikely to be addressed by initial automation attempts, which will prioritize stereotaxic brain injections. Therefore, this peripheral trigeminal innervation dataset is likely to be useful for a broad range of applications, from physiology to bioinformatics, and for inclusion in larger efforts in the future that would otherwise not replicate it. Additionally, our methods for digitizing and registering the data in a standard coordinate frame allow the data to be incorporated into larger frameworks for comparison across multiple scales of spatial and temporal resolution using disparate imaging and physiological techniques.

Our projection database is composed of many injections to each of the regions of face known to be innervated by each of the three branches of the trigeminal nerve: ophthalmic (supraorbital and forehead region), maxillary (vibrissa pad, microvibrissae and upper lip), and mandibular (lower lip and tongue). By nature of peripheral labeling with tracers and the spatial arrangement of subcutaneous receptors, any single case of a given branch injection may not label the entire set of receptors or central afferents. We have addressed this issue in three ways. First, in a subset of the cases, we have performed multiple injections in several locations for a given branch; for example, we injected into both the left hemi-section of the tongue and that of the lower lip for a subset of mandibular injections. Second, by combining the set of central afferents labeled, possibly incompletely, for each of the experiments on a given branch, we can digitally reconstruct a more complete set of projections by combining across different cases. This approach would not account for central afferent patterns that remained unlabeled in any of the injections; however, the majority of trigeminal brainstem is likely labeled over all of the cases, when compared to full trigeminal ganglion injections (see Sec. 2.4 of this thesis). Also, this approach assumes little individual variation, a reasonable consequence of our exclusively using adult males of an inbred mouse line (C57BL/6 strain). Third, we have reasoned that focal injections which do not label the entire branch could still provide insight into local patterning and cues, for example, by indicating terminal regions for one set of vibrissae versus a distinct set.

Why might peripheral afferents relate at all to genetic expression in the brainstem? The genomic data used in this study are from ISH riboprobes, which report mRNA transcript levels in soma and, for some cytoskeletal related transcripts, in dendrites [Lein et al., 2007]; meanwhile, our data label trigeminal ganglion cells, which are located outside of the brain, but with projections mapped centrally. Numerous neurodevelopmental results demonstrate that axon guidance and synapse formation require receptor-ligand pairs [Polleux et al., 2007]. This reliance on genetically-expressed cues for organization has been demonstrated specifically in the trigeminal system [Hodge et al., 2007] and, critically, for neuronal maintenance in the adult [Liu et al., 2008]. Therefore, it is reasonable, and likely, that gene expression patterns seen in soma or dendrites of trigeminal brainstem are inextricably related to the pattern of primary afferents impinging on them. Indeed, such a relationship appeared to be borne out in the expression analysis.

## 3.5.2 Statistical considerations

### 3.5.2.1 Quantification with amplified, non-isotopic ISH and probe quality

The ISH method employed by the Allen Brain Atlas uses a non-isotopic, amplified approach in order to provide cellular resolution data; however, this comes with the cost of a graded signal output [Ng et al., 2007, Lee et al., 2008]. Some groups have shown that non-isotopic methods are as sensitive as radiometric strategies for certain genes [Hougaard et al., 1997, Higo et al., 1999, Carson et al., 2005]. However, because of both this non-isotopic method, and the fact that amplification and signal detection of the image data were set for low expression detection, reported expression levels in AGEA may be more appropriately described in a qualitative (e.g. low , medium, and high), rather than a quantitative, framework [Ng et al., 2007, Lee et al., 2008, Jones et al., 2009]. Because the decision tree learning we employ evaluates both the information provided by genes and per gene expression threshold, the potentially non-quantitative nature of the data could be an issue. This issue could be explored using various techniques, including grouping the data into qualitative expression level sets, or exploring the sensitivity of the algorithm to perturbations around computed thresholds.

Other issues have been raised regarding the ISH probes, such as insufficient uniqueness, cross-hybridization with other genes, and detection of multiple splice forms of target genes; however, these issues have been addressed as noted by either removal from the database or redesign of improved probes [Jones et al., 2009]. Finally, to address concerns with the data quality, the Allen Institute has confirmed the expression profiles with those published in the literature for 1000 of the most popular genes[1]. Because we focus on highly informative genes in this work, these concerns underscore the importance of validating with complementary approaches (see 3.4 and 3.5.3); however, the methods we develop are applicable as genomics databases improve.

#### 3.5.2.2 Problems in high dimensions

A frequent issue in applications of statistics to modern biology is the so-called "small N, large p" problem, in which the number of independent measurements is far fewer than the number of parameters to be estimated from the data [Hastie et al., 2009]. This problem applies to the ABA dataset: the number of independent samples of a given gene in a given voxel is derived from image analysis of one or two local brain sections from one animal [Lein et al., 2007]. While many statistical learning methods are susceptible to overfitting, and decision trees are not an exception [Hastie et al., 2009], this problem is not unsurmountable, and successful classifiers have been built for the analagous problem in high dimensional microarray [Golub, 1999, Tamayo et al., 1999] (see also *Nature Genetics* Supplement 32, 2002) and single nucleotide polymorphism (SNP) data [Wu et al., 2009]. The ABA dataset adds a dimension of complexity because it involves spatially registered expression data, but other expression data sets can also add such complexity, notably in the temporal dimension, so in principle, the scale of the problem is similar. Here, we endeavor to circumvent this problem by first preselecting potentially relevant genes and discarding potentially uninformative ones, a common approach to overcoming the large P problem with application-specific approximations [Duda et al., 2001]. In particular, we use a set of reasonable feature selection criteria, reducing the number of genes studied from $\sim 20,000$ to less than 1000, which is the same order of magnitude as the number of voxels studied, $\sim$ 600, in trigeminal brainstem. Importantly, we note that principled, application-independent approaches to gene selection have not yet been formalized because of the dependence of underlying expression distributions across genes [Committee, 2005]. Additionally, we used 10-fold cross-validation to, in effect, repeatedly resample the data for generalization to indepen-

---

[1] Technical white paper: Top 1000 genes analysis: Validation of frequently accessed genes in the Allen Mouse Brain Atlas (2010). Allen Brain Institute [online], http://help.brain-map.org/display/mousebrain/Documentation

dent data.

To address the $n \ll P$ problem with further analysis, we would propose two directions. First, it would be useful to apply other sparse algorithms, such as the least absolute shrinkage and selection operator (LASSO) using $L^1$-norm regularization [Tibshirani, 1996] and elastic net regularization [Zou and Hastie, 2005]. LASSO introduces a sparsity penalty that drives the coefficients of uninformative features to zero; this method, therefore, would also emphasize individual genes that are most informative in classifying regional voxels [Tibshirani, 1996]. This focus on a sparse set of genes is important for biological interpretability (see above discussion), and has been applied successfully to SNP data [Wu et al., 2009]. However, when features are highly correlated, as in the ABA data set, LASSO selects just one gene to represent the correlated set. Therefore, elastic net regularization, which adds a quadratic penalty to the $L^1$-norm of LASSO, could complement the results; however, knowledge that a large group of genes is an informative feature in defining the boundaries of a particular region is less useful biologically. Transgenic and viral technologies are generally focused on single- or two-gene manipulations (see Sec. 3.5.3).

Second, we could, in principle, apply our histological database and subsequent analysis to independent genomics data sets. Unfortunately, no other data exist on the scale of the ABA data for adult mouse. The best candidate for extension of our work is EMAGE, a large-scale ISH database of the mouse embryo including $\sim$19,000 gene expression probes [Christiansen et al., 2006, Richardson et al., 2010]. It would be interesting to apply the sparse techniques we employ here to this data set; however, the projection data will not be relevant. It would be of great interest to perform similar injections in the developing mouse, since much of the gene expression that is developmentally important occurs in the first two postnatal weeks in mouse [Erzurumlu et al., 2010]. Importantly, though, because synapses must be maintained by the consistent turnover of synaptic proteins [Hirai et al., 2005, Lin et al., 2009], it is reasonable to infer that genes encoding connectivity information continue expression into adulthood. Indeed, some of the genes that resulted from our analysis (e.g. *Hoxa5*) are the very ones implicated in development.

### 3.5.3 Future directions

The trigeminal afferents whose central terminals we have examined in this study transmit information from a diverse array of receptors, including those for touch, temperature, and pain [Lumpkin and Caterina, 2007, Belmonte and Viana, 2008]. The vibrissa follicle alone contains a multitude of touch-sensitive receptor endings and specialized cells that synapse with primary trigeminal ganglion afferents [Rice et al., 1993, Rice et al., 1997] (see also Sec. 4.2 for a close reading of this literature). Recent work has begun to distinguish the molecular profiles of some of these touch receptor types and sensory subpopulations [Hasegawa et al., 2007, Hodge et al., 2007, Hasegawa and Wang, 2008]; however, the genetic tools available to independently probe these subpopulations are still limited. Large-scale informatics studies like the present one could suggest potential candidates for identifying and characterizing subpopulations of receptors. Conversely, histological data from these molecularly-defined subpopulations could be incorporated into our projection database: evaluating expression in the central termination patterns of these subpopulations could suggest other candidates for trigeminal organization.

A key reason we utilize a sparse supervised learning method in this study is to identify individual or small sets of genes that could play a role in trigeminal organization. One way to confirm that the mRNA transcripts uncovered through bioinformatics are relevant to the system is to confirm that the proteins they encode are translated in the neurons of predicted regions of expression. Such confirmation could be done with immunohistochemistry using antibodies against known gene products and looking for colocalization, and would be strong confirmation of the statistical methods. Alternatively, one could generate a transgenic mouse using the reconstituted GFP (recGFP) system [Ghosh et al., 2000], in which two fragments of GFP are expressed by promoters associated with our two genes of interest, such that only cells containing both genes would express GFP [Zhang et al., 2004]. Each of these approaches, antibody staining and recGFP, could confirm regionalized neuronal co-expression of genes we propose play a role in organization. However, reliable antibodies do not exist for all known proteins. Additionally, confirmation of the presence of a gene product does not demonstrate necessity for its role in organization or maintenance of a circuit. To determine whether proposed pairs of gene products play a role in organization, one could generate a transgenic mouse line using the Cre-loxP binary expression system [Orban et al., 1992, Gu et al., 1994]. Applied here, Cre recombinase expression could be driven by a promoter associated with expression of the first gene of interest, and loxP flanking a stop codon could be expressed only in neurons expressing the second gene. Only when the two genes are co-expressed would an XFP reporter downstream of the floxed stop codon be expressed. Further, tamoxifen-inducible Cre [Metzger et al., 1995] could be used to provide a means to directly manipulate the timing of Cre-loxP based expression, which would provide a means for probing the organizational role of these genes during development or circuit maintenance in adults.

*We thank the Allen Brain Institute for its generous open distribution of the ABA genome data. This chapter, in part, is a manuscript in preparation for likely submission. The dissertation author is the first author of this paper; though the full co-authorships have not yet been determined, they will include Harvey J. Karten, and David Kleinfeld.*

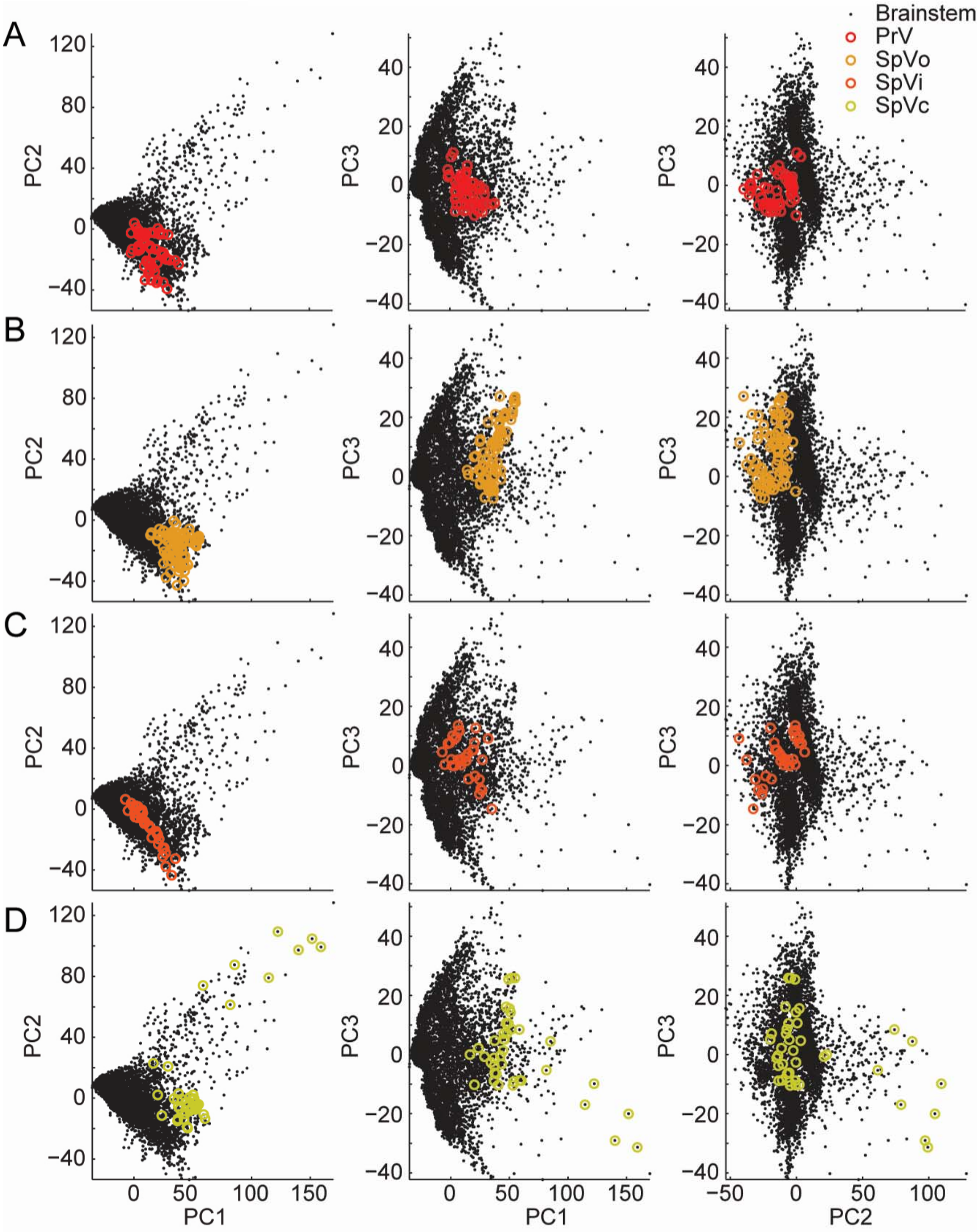

**Figure 3.5**: *Trigeminal nuclei-based clustering of brainstem voxels in principal component space.*

The gene expression from each voxel of the brainstem is projected into the first three dimensions computed from principal component analysis, and shown for each pair of two-dimensional principal component comparisons. Voxels with membership in different nuclei are represented by color, including principalis (A), oralis (B), interpolaris (C), and caudalis (D).

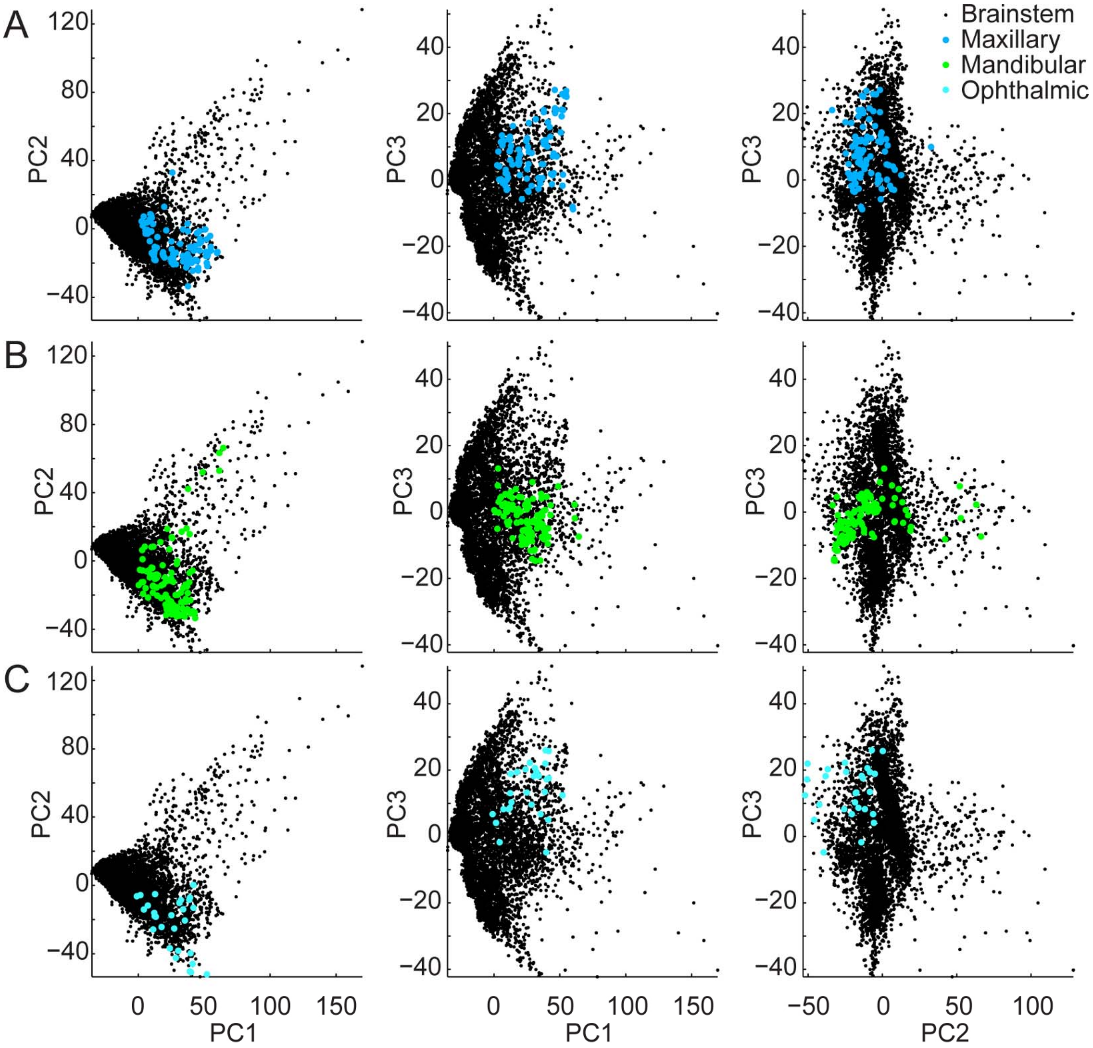

**Figure 3.6**: *Trigeminal projection-based clustering of brainstem voxels in principal component space.*

The gene expression from each voxel of the brainstem is projected into the first three dimensions computed PCA and shown for each of the two-dimensional PC comparisons. Voxels that receive input from each of the three trigeminal nerve branches are represented by color, including maxillary (A), mandibular (B), and ophthalmic (C).

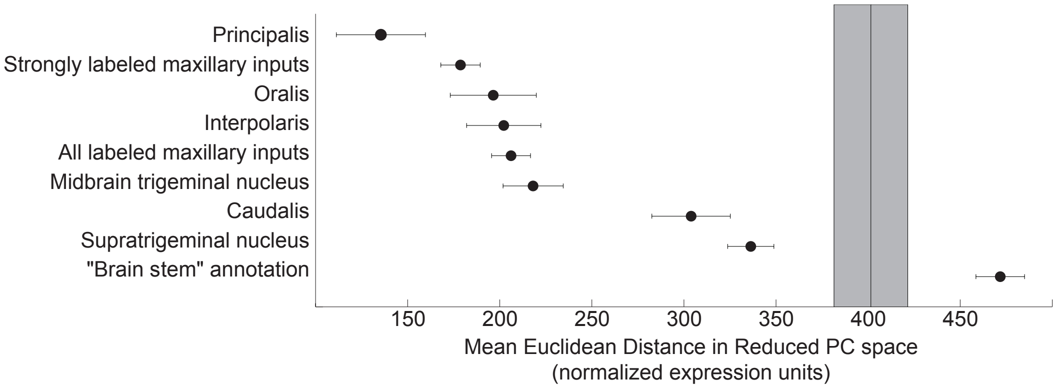

**Figure 3.7**: *Similarity index for trigeminal brainstem groups.*

The one-to-one Euclidean distance among all voxels within trigeminal input or nuclei groups in principal component space. CTb labeling results are shown for the maxillary, or whisker pad, inputs, and nuclei are from ARA. The ‘random’ group is drawn from a random sample of brainstem voxels. Points and horizontal bars indicate mean ± S.E.M.

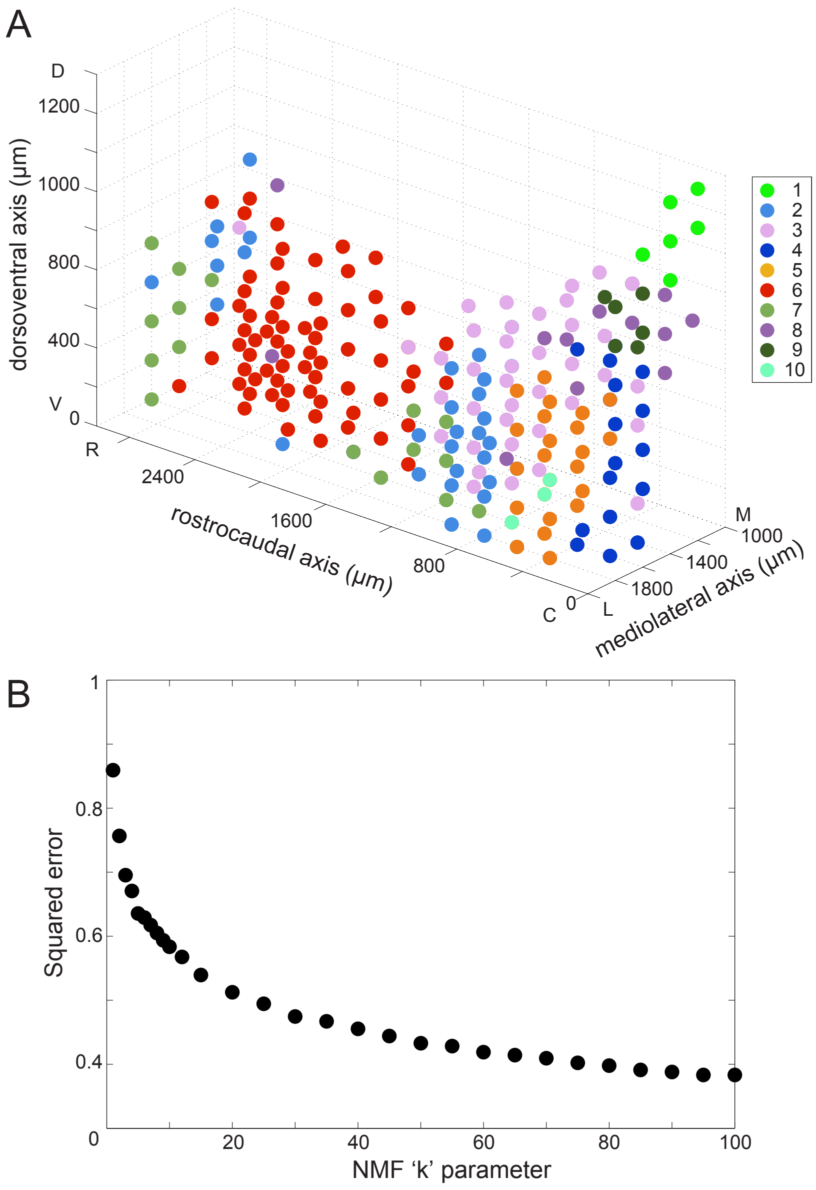

**Figure 3.8**: *Non-negative matrix factorization of trigeminal EEM*

(A) Voxels of the trigeminal brainstem, color coded by the basis vector of $W$ contributing the most to the genetic expression profile for that voxel. Voxels are positioned in brain coordinates, with the anatomical axes shown. The mediolateral dimension is set to 0 at the midline; dorsoventral is set to 0 at the ventral base of the brainstem; rostrocaudal is set to 0 at the beginning of the spinal cord. (B) The residual of EEM - $WH$ for increasing parameter $k$. The monotonic decay suggests that no particular number of regional parcellations is strongly suggested by NMF.

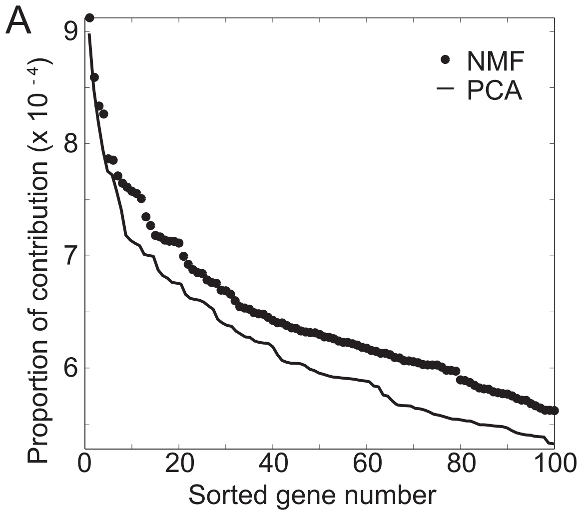

B

| NMF | PCA |
|---|---|
| Tuba1 | Tuba1 |
| Tnfaip6 | Neu3 |
| Neu3 | Tnfaip6 |
| 2510006D16Rik | 8030498B09Rik |
| 8030498B09Rik | LOC545465 |
| Aplp1 | Dynll2 |
| Pex16 | 2510006D16Rik |
| LOC546142 | LOC546142 |
| Atp5b | Gapdh |
| Gapdh | Gtl2 |
| LOC385068 | Aplp1 |
| Mmachc | Nsf |
| Dynll2 | Mmachc |
| Optc | Optc |
| Hes6 | App |
| Mtap1b | Fbxo22 |
| Tuba2 | Atp5b |
| Fbxo22 | Pex16 |
| Thy1 | 1700008H02Rik |
| LOC545465 | Mtap1b |
| 1700008H02Rik | 4930470H14Rik |
| Atp6v0b | Rtn1 |
| Gtl2 | LOC385068 |
| LOC433089 | Prepl |
| MGC68323 | LOC433089 |

**Figure 3.9**: *Gene contributions from dominant basis vectors of NMF and PCA.* (A) Sorted proportional contributions of the 100 most contributing genes to the dominant basis vector (for NMF) or first eigenvector (for PCA). (B) Lists of the 25 most-contributing genes from each analysis; 20 of the 25 genes appear in both lists. This correspondence holds true for other basis vectors examined (through the first 10).

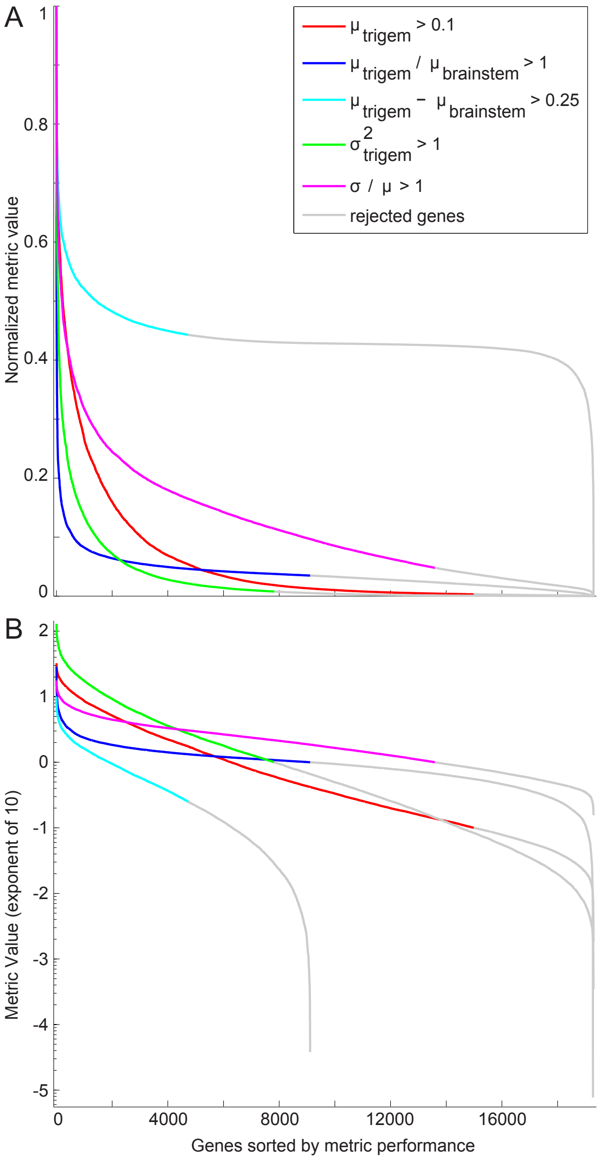

**Figure 3.10**: *Feature selection by preprocessing metrics*

Gene expression profiles assessed on the basis of several preprocessing metrics (see legend). Colored portions of plots indicate genes that satisfied these conservative thresholds; gray did not. Genes are sorted by performance on individual metrics: the same gene is not necessarily numbered identically for each metric. (A) Expression profile distributions for each of the preprocessing metrics on a linear scale. Data are normalized from zero to one for each metric. (B) Expression profile distributions for each of the preprocessing metrics on a logarithmic scale. Data are unnormalized, to show the full distribution. The abscissae are the same for both plots.

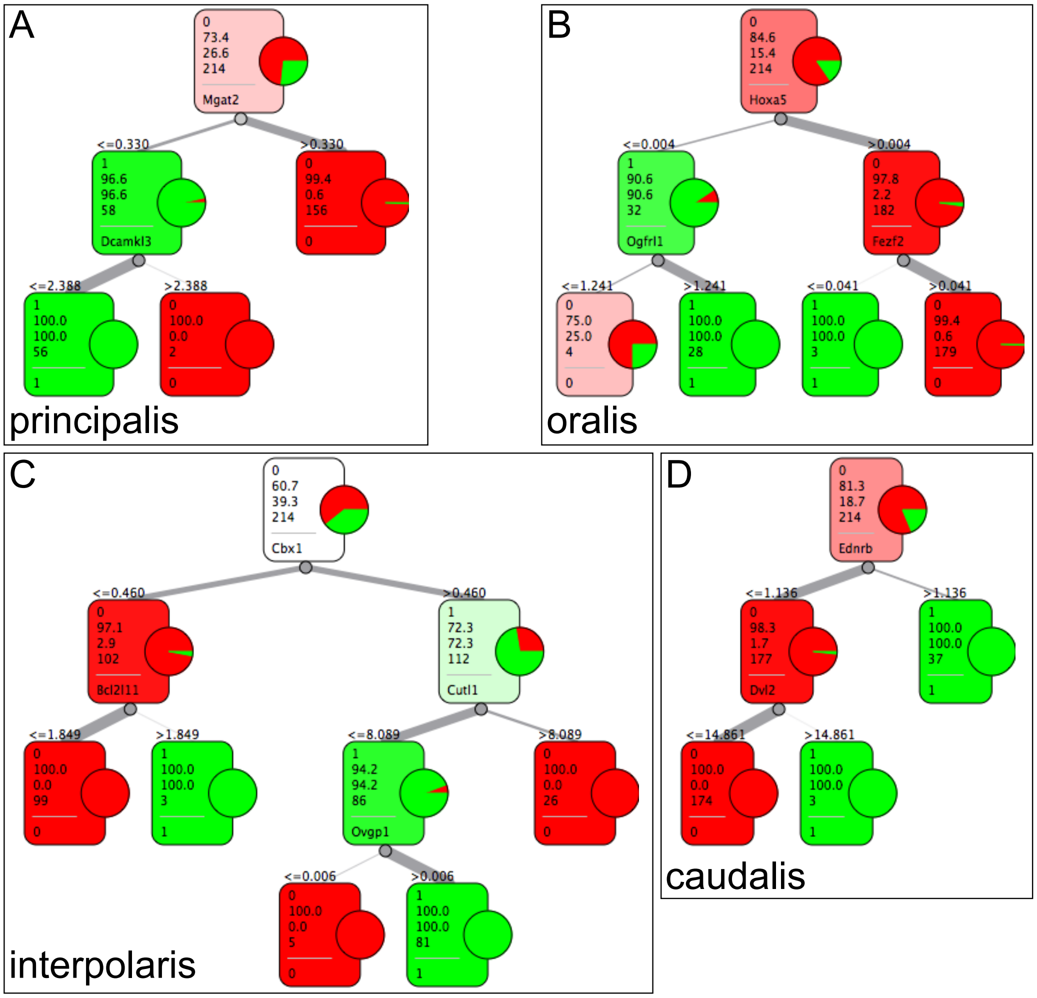

**Figure 3.11**: *Visualized decision trees for membership in trigeminal nuclei* Decision trees for each of the four annotated nuclei of the trigeminal brainstem: (A) principalis, (B) oralis, (C) interpolaris, and (D) caudalis. The pie chart represents the fraction of voxels that are in the target nucleus class (green) versus the non-target class (red). Each node shows (1) the gene expression threshold (above box), (2) the target class, the percentage of majority (3) and target (4) voxels, (5) the number of total voxels, and (6) the next gene for partitioning. Boxes are shaded by the proportion of voxels that are in the majority class (e.g. green shading contains mostly target voxels).

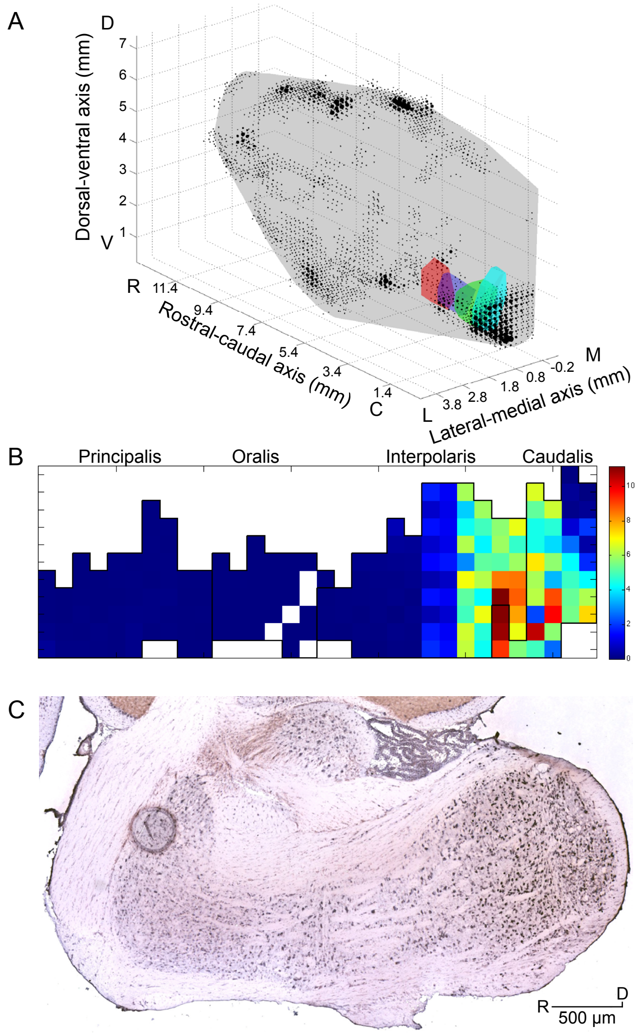

**Figure 3.12**: *Sample gene expression from training on nuclei:* Hoxa5

(A) Gene expression of *Hoxa5* in the left hemisphere of the brain. For each voxel, a sphere is plotted whose radius increases with expression intensity. The four nuclei are colored in red (principalis), purple (oralis), green (interpolaris), and cyan (caudalis). Brainstem expression is greatest in caudalis. (B) The three dimensional voxel space is mapped to a two dimensional representation of voxel space that preserves local distances among voxels. Black contours outline the four trigeminal nuclei, and expression intensity is represented as a heatmap. (C) A representative ISH section of *Hoxa5* from the Allen Brain Atlas image database, showing high levels of probe binding in interpolaris and caudalis.

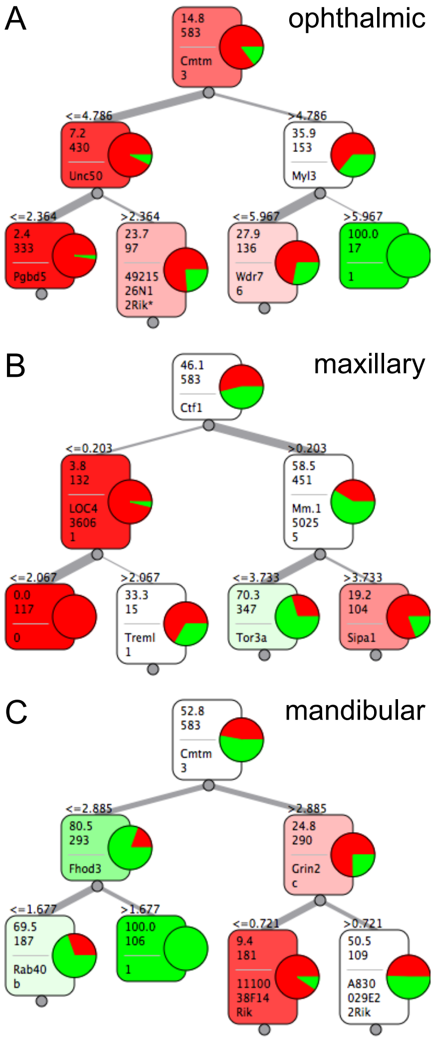

**Figure 3.13**: *Schematic decision trees of the three trigeminal branch inputs.* Decision trees for the classes of voxels containing projections from each of the three main branches of trigeminal nerve: (A) ophthalmic, (B) maxillary, and (C) mandibular. Similar to figure 3.11, the pie chart represents the fraction of voxels that are in the target class (green) versus the non-target class (red). Each node shows (1) the gene expression threshold used (above box), (2) the percentage of target voxels, (3) the number of total voxels, and (4) the next gene for partitioning; boxes are colored by the proportion of voxels that are in the majority class (e.g. greener indicates more target voxels). We show the first two branches of each tree for visualization purposes, but in some cases they extend to more levels, indicated by the branch point below boxes.

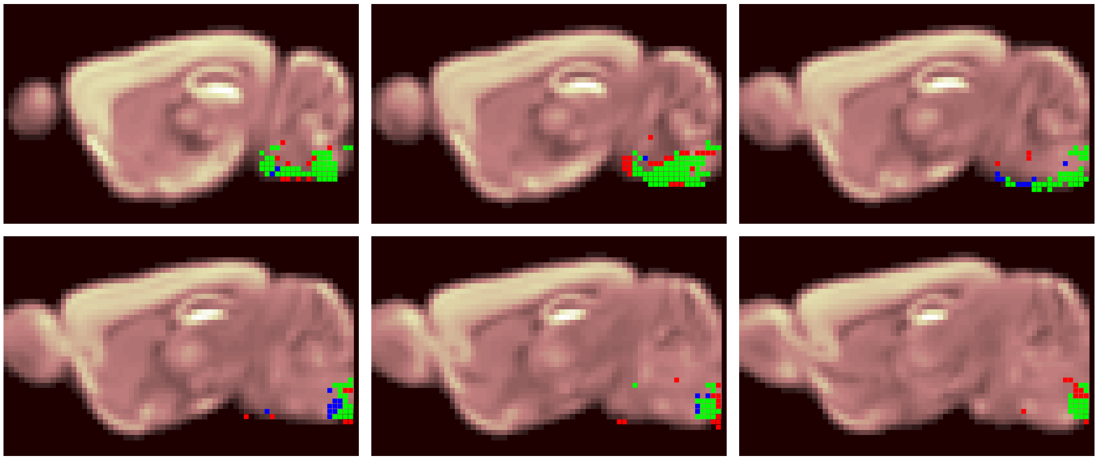

**Figure 3.14**: *Classification performance for maxillary decision tree superimposed on the voxelized brain.*

Classification performance is coded by color: voxels correctly labeled as maxillary (green), voxels incorrectly labeled as maxillary (red), and voxels incorrectly labeled as not maxillary (blue). Sagittal brain sections are placed for reference; these are spaced by 200 $\mu$m to match the ABA expression data. Sections include the majority of trigeminal brainstem and are arranged from the most lateral (top left) to the most medial (bottom right).

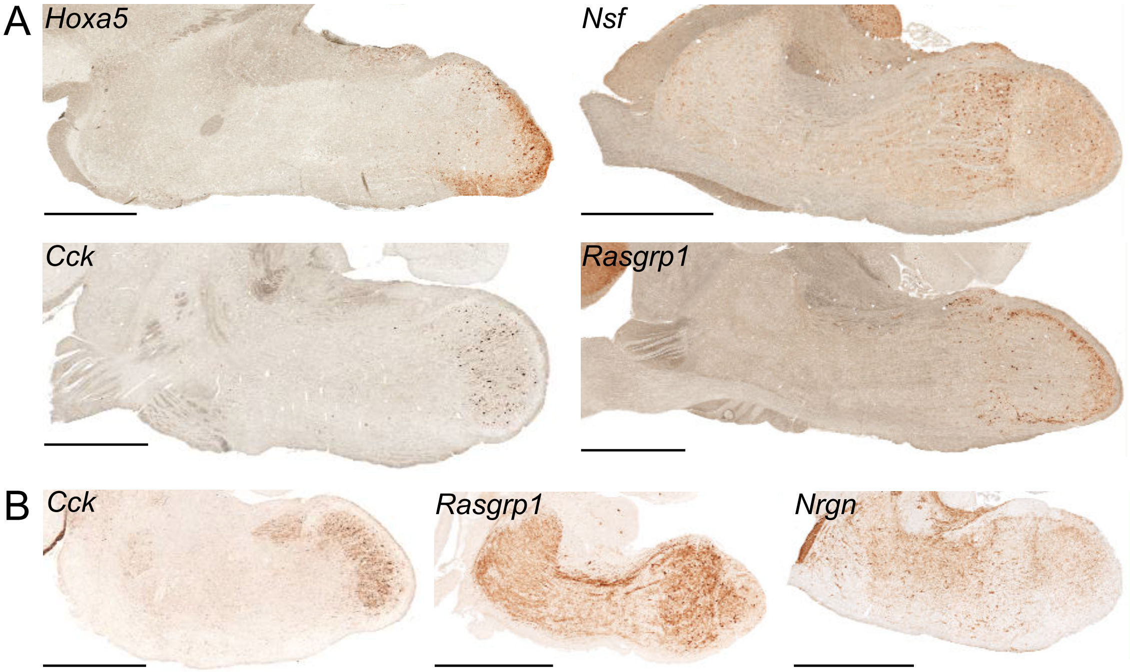

**Figure 3.15**: *Comparison with BAC database.*

Highly informative genes from our analyses show localized trigeminal expression patterns in both adult (A) and postnatal day 7 (B) neural tissue. A brown or black reaction product indicates regions of high expression. All images show primarily brainstem in a sagittal plane of section, in which rostral is toward the left and dorsal is toward the top of each panel. Scale bars = 1 mm.

# Chapter 4

# Imaging the mechanics of follicle receptors with two photon microscopy

## 4.1 Abstract

The encoding of somatosensory stimuli begins with signal transduction at specialized peripheral receptors in the dermis and epidermis. The murine follicle-sinus complex (FSC) is a useful model system for studying receptor mechanics, sensory transduction, and signal encoding because of its diverse innervation and its developmental, molecular, and physiological relationship with the trigeminal system. Understanding peripheral transduction is essential to understanding the inputs to upstream circuits. While much of the microanatomy of the FSC is well described, the mechanics of its receptors in response to sensory stimuli is not known. Here, we develop a novel *ex vivo* preparation for imaging the inner sensory receptors of the FSC using two photon imaging. We visualize peripheral sensors with fluorescent labels, surgically remove a row of follicles, and image the receptors using two photon microscopy. When a vibrissa is deflected along the path of whisking, receptors compress or expand about the vibrissa axis. Further, longitudinal deflection of a vibrissa results in morphological changes in a subset of receptor endings. These data are consistent with behavioral observations of rotational movements during whisking, and physiological data of responses to longitudinal deflection. This preparation will likely be useful both for developing a realistic biomechanical model of sensory receptors innervating the FSC, and for imaging the activity of receptors with calcium sensitive dyes in response to vibrissa deflection.

## 4.2 Introduction

Peripheral sensory transduction involves a variety of mechanisms evolutionarily tuned to the behavioral requirements of organisms. While transduction mechanisms of photoreceptors for vision [Burns and Baylor, 2001, Arshavsky and Burns, 2012], hair cells in audition [Roberts et al., 1988], olfactory sensory cells in olfaction [Breer, 2003], and taste receptors in gustation [Yarmolinsky et al., 2009] are well characterized, somatosensation has historically resisted mechanistic and molecular description. Recent interest in somatosensory transduction has elucidated many transduction schemes [Lumpkin and Caterina, 2007], especially for temperature and pain sensation using TRP channels [Venkatachalam and Montell, 2007]; however, the full sensory transduction of mechanosensory stimuli remains unsolved [Lumpkin and Caterina, 2007].

The follicle sinus-complex (FSC) is a useful model system for studying mechanosensory transduction and encoding because its morphology, innervation, and physiology are well-characterized. The FSC has been characterized with electron [Andres, 1966,Patrizi and Munger, 1966] and light [Munger and Rice, 1986,Rice et al., 1986] microscopy, revealing a complex, three-dimensional arrangement of nerve terminals from the infraorbital branch of the trigeminal nerve [Rice et al., 1993, Rice, 1993, Rice et al., 1997, Kim et al., 2011]. Nerve terminals are organized spatially in six groups within the follicle: the rete ridge collar, the inner conical body, the sinus capsule neck, the ring sinus, the cavernous sinus, and the dermal papilla [Rice et al., 1997]. Some of the more prominent endings include Merkel cell-neurite complexes [Merkel, 1875, Winkelmann and Breathnach, 1973], lanceolate endings, bundled C-fiber terminals, fine caliber axon endings, and reticular endings [Rice et al., 1993]. These terminals arrive through both the deep (83% of axons) and superficial (17%) vibrissal nerves [Rice et al., 1993, Waite and Jacquin, 1992]. The mean numbers of myelinated and unmyelinated axons for each follicle are $186.0 \pm 48.2$ and $90.2 \pm 15.7$, respectively ($\mu\pm$ S.D.), with the number of both types increasing along the rostral-caudal axis of the mystacial pad [Waite and Jacquin, 1992, Klein et al., 1988].

Meanwhile, the physiology resulting from the mechanosensory activation of follicles is also well characterized. A large proportion of trigeminal ganglion (Vg) units are directionally selective, with single units encoding vibrissa deflections in latitudinal directions with both slowly adapting and rapidly adapting responses (75% and 25%, respectively) [Lichtenstein et al., 1990]. Vibrissa responses to axial displacements are also strong [Stüttgen et al., 2008]. Limited band noise stimuli evoke reliable Vg responses, such that reverse correlation of the activity of one or a few cells with the stimulus can be used to determine the linearly optimal physical stimulus parameters with high accuracy [Jones et al., 2004]. Additionally, individual vibrissae can act as frequency-specific band-pass filters, depending on their intrinsic resonance frequencies [Hartmann et al., 2003,Neimark et al., 2003,Andermann et al., 2004,Shatz and Christensen, 2008]. These resonances form a systematic map across vibrissae, suggesting a combination of spatially distributed texture encoding [Neimark et al., 2003] and individual vibrissal kinetic encoding [Arabzadeh et al., 2005, Szwed and Ahissar, 2006]. In addition to contact and resonance signals, Vg cells report the position of the vibrissae [Szwed et al., 2003, Szwed and Ahissar, 2006]. Further, some Vg cells respond to vibrissa position, to vibrissa contact with or release from an object, or to a combination of these [Szwed et al., 2003]. Extracellular recordings from awake rats confirm that many of these response properties hold true during behavior [Nicolelis et al., 1995, Leiser and Moxon, 2007, Khatri et al., 2009].

The fact that Vg neurons can encode many stimulus parameters is consistent with the receptor diversity at the follicle. Biomechanical models of the FSC have captured some of these physiological properties [Mitchinson et al., 2004, Birdwell et al., 2007]; however, these models remain phenomenological because of the lack of empirical descriptions of the forces impinging on individual receptors from vibrissa movement. Ultimately, despite detailed knowledge of the microarchitecture of the follicle and physiology of Vg neurons, the relationship between nerve terminal morphology and physiological encoding remains elusive. Here, we examine this relationship with a novel *ex vivo* preparation for two photon imaging of intact, visualized follicle sensors in response to movements of the vibrissa.

## 4.3 Methods

### 4.3.1 Surgical extraction and preparation of follicle

Adult C57BL/6, PvCre-FloxTdTomato, and CerTNL-15 mice were euthanized by intraperitoneal injection of $100 - 200$ $\mu$L of pentobarbital (Fatal Plus), followed by careful removal of the entire mystacial pad from both sides of the face. Subsequent steps for imaging preparation were performed in two ways. In the case of imaging with calcium sensors (Fig. 4.1A), a single follicle was removed from the vibrissa pad and a $\sim 1 \times 2.5$ mm portion of the follicle capsule was excised for optical access; the window is positioned longer in the longitudinal direction, parallel to the axis of the vibrissa. This portion of the surgery requires the greatest care to avoid disturbing the sensitive receptors underlying the capsule. The tissue was then transferred to a custom-machined imaging dish designed to submerge the follicle while its vibrissa was in air.

Throughout the excision process, the tissue was submerged in cold carbogen-infused artificial cerebrospinal fluid (ACSF). After the tissue was excised and the window was sufficiently large, a thermocouple was placed in the bath for feedback-controlled maintenance of constantly-perfused ACSF at 37°C. The vibrissa was cut to $\sim$10 mm and inserted $\sim$ 100 $\mu$m into a glass pipette, which was coupled to a computer controlled piezoelectric stimulus that moves in all directions of the perpendicular plane to the vibrissa. In some cases, we also positioned tungsten single channel electrodes (0.5 MΩ, WE30030.5A10; MicroProbes) near to the receptor endings for current stimulation to observe $Ca^{2+}$ transients, or coupled the vibrissa to a manual manipulator that moved along the axis of the vibrissa. Finally, the two photon microscope objective was positioned such that receptors of interest were visible. In the case of imaging for mechanical movement of the receptors (Fig.4.1B), a reduced preparation was used, where temperature controlled ACSF was replaced with 37°C phosphate-buffered saline (PBS) and the piezoelectric stimulus was replaced with a micrometer-resolution manipulator (MPC-200; Sutter Instrument, Novato, CA). Additionally, we included the tissue surrounding individual follicles, typically an entire follicle row. For this chapter, we focus on data from the latter case. Animal care and treatment conformed to the National Institutes of Health Guidelines and were approved by the Institutional Animal Care and Use at University of California, San Diego.

### 4.3.2 Imaging and analysis

Fluorophores that were not expressed transgenically were introduced in the following ways. $\sim$ 2.5 $\mu$L / g body weight of 2 mM FM1-43X (F-35355, Invitrogen) was injected sub-cutaneously 24 h before imaging. 4',6-diamidino-2-phenylindole (DAPI) dilactate (1:1000; Sigma-Aldrich) was exposed to the follicle for $20-30$ min following introduction of the capsule window. Images of follicles were taken by several means. Wide-field imaging was performed with an upright fluorescence microscope (MVX10, Olympus and Axioplan2, Zeiss) and high resolution imaging with a confocal microscope (FV1000, Olympus) using a 20× air objective; these images were converted and leveled in Fiji (an open source ImageJ distribution). Two photon imaging was performed on a custom-built system [Tsai et al., 2009], tuned to 800 nm, with a 40× water objec-

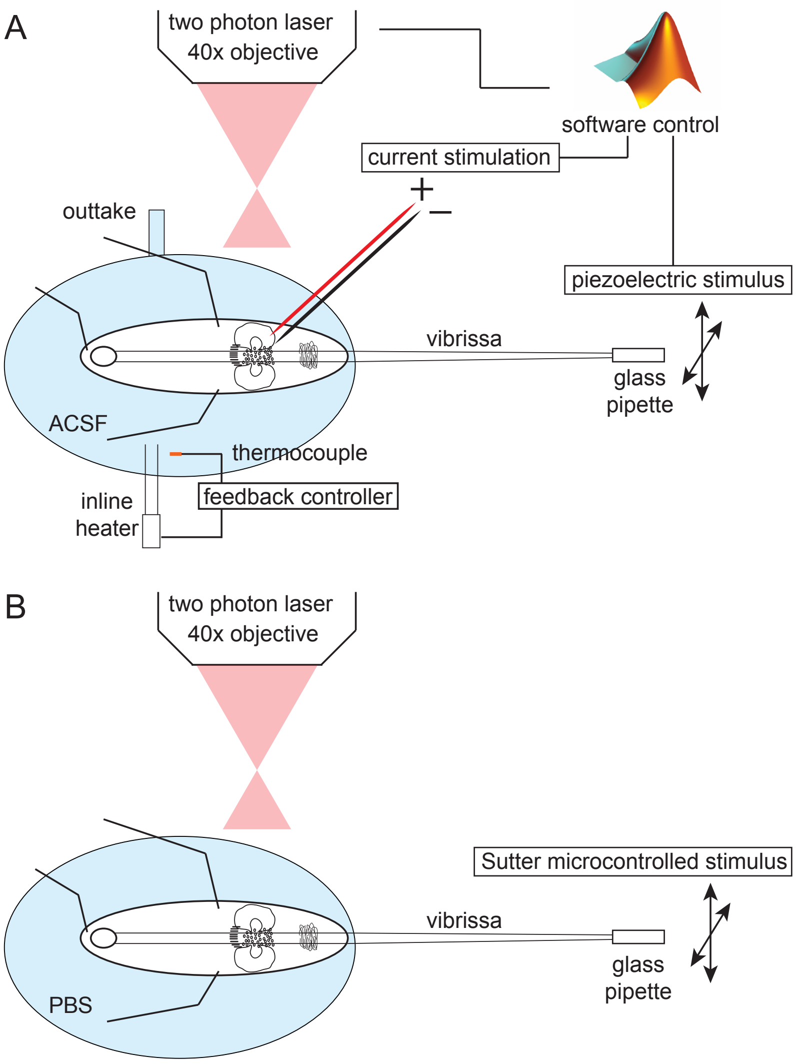

**Figure 4.1**: *Schematic of follicle preparation for two photon imaging*. (A) For live follicle imaging, the tissue is surgically removed from the face and pinned to a firm gel plate custom machined to allow the follicle to be submerged for imaging while its vibrissa remains in air. The vibrissa is positioned within a glass pipette coupled to a piezoelectric device. Current electrodes are positioned near the receptor endings for stimulation. A 40× objective is positioned to best visualize receptor endings in the follicle. All devices are under software control on a central computer. ACSF is perfused through the system and heated by a feedback-controlled temperature unit. (B) In the reduced preparation, vibrissa manipulation is performed submerged in PBS and is governed by a micrometer-resolution manipulator.

tive and galvanometric scan mirrors (6210H scanners with MicroMax 673XX dual-axis servo driver; Cambridge Technology), using MPScope [Nguyen et al., 2006, Nguyen et al., 2009] for acquisition and control.

In order to assess receptor mechanics, we took two photon image stacks of the follicle body, centered on Merkel cells near the ringwulst. The receptors were imaged (1) in their relaxed ('set point') position, with the vibrissa undeflected in the bath; (2) at $10^\circ$, $20^\circ$, or $30^\circ$ angles from the set point in cardinal and ordinal directions about the vibrissa axis; or (3) at 180 $\mu$m axial displacements from the set point. Because the entire tissue can move in response to vibrissa deflections, we corrected for global tissue rotation by registering each volume with the set point case. The positions of DAPI-stained bodies for the deflected (pink, for the example in figure 4.2A) and set point (cyan) cases were automatically identified, then shifted together to minimize the sum of squared errors, in all three planes, between the two population of points (Fig. 4.2). Custom scripts for analysis were written in Matlab (Mathworks, MA).

## 4.4 Results

### 4.4.1 Follicle imaging

In order to visualize the follicle receptors, we screened for a suitable fluorescence-based contrast agent. Given the high fatty tissue content in the periphery, we began with a fluorescently-tagged lipophilic dye, 5-hexadecanoylamino-fluorescein (Invitrogen, H-110). We found that the fluorophore did not label receptors reliably and bleached quickly: typical signals from this fluorophore dropped by more than 50% at 4 s of exposure, and to $\sim$1/3 of initial fluorescence by 30 s (Fig. 4.3). Because we needed to image a single follicle over several hours to measure many deflection conditions, this bleaching rate was unacceptable.

We found several fluorophores that permitted consistent, well-resolved imaging of the follicle. First, we used a transgenic animal in which parvalbumin neurons expressed Cre (PvCre), and crossed this with a floxed reporter line conditionally expressing TdTomato red fluorescent protein; the crossed transgenic animal is named PvCre-TdTomato. Noting that some Vg neurons express parvalbumin and that this expression

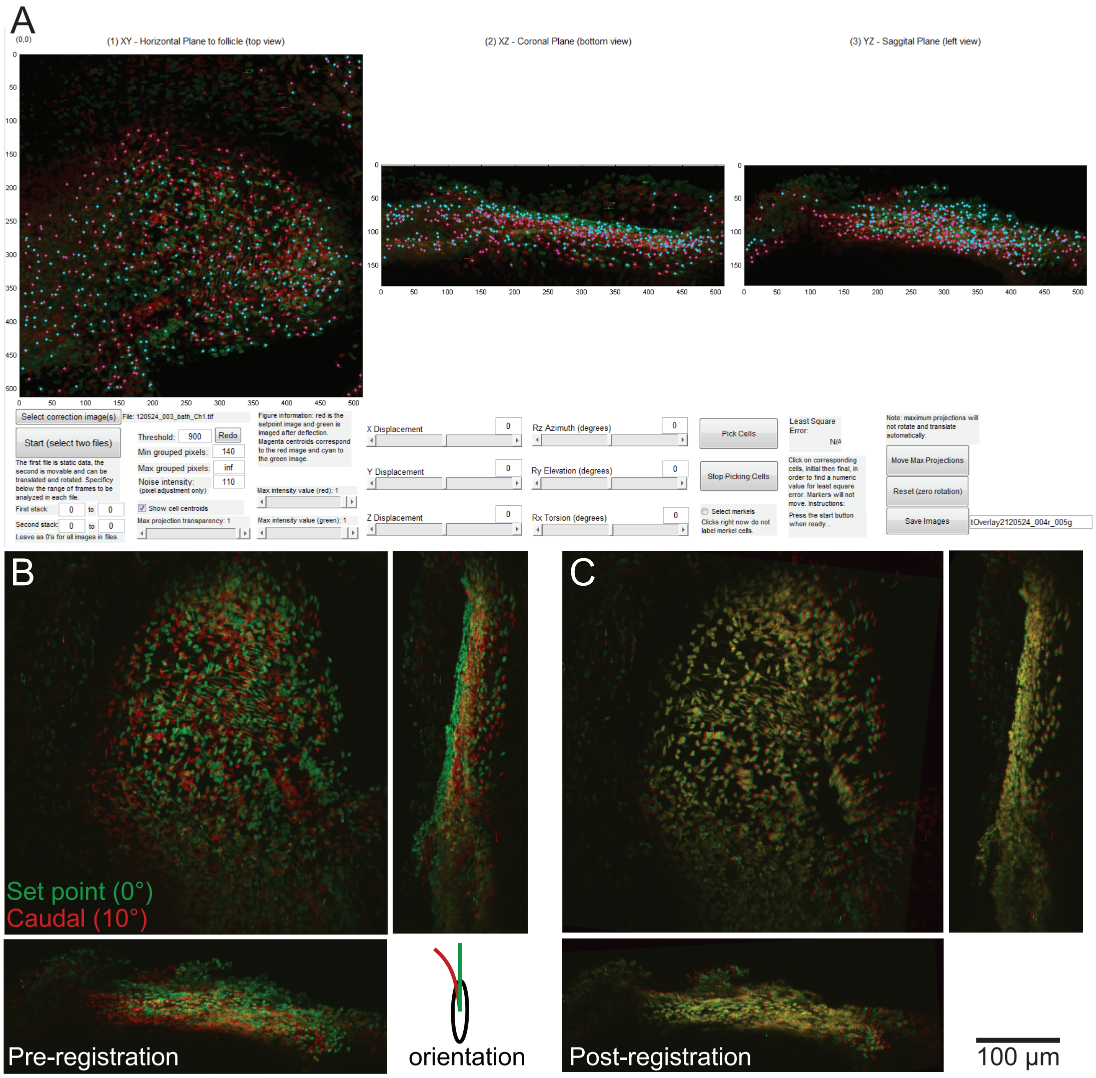

File: 120524_003_bath_Ch1.tif

The first file is static data, the second is movable and can be translated and rotated. Specificy below the range of frames to be analyzed in each file.

First stack: 0 to 0

Second stack: 0 to 0

Leave as 0's for all images in files.

Threshold: 900

Min grouped pixels: 140

Max grouped pixels: inf

Noise intensity: (pixel adjustment only) 110

☑ Show cell centroids

Max projection transparency: 1

Figure information: red is the setpoint image and green is imaged after deflection. Magenta centroids correspond to the red image and cyan to the green image.

Max intensity value (red): 1

Max intensity value (green): 1

X Displacement: 0

Y Displacement: 0

Z Displacement: 0

Rz Azimuth (degrees): 0

Ry Elevation (degrees): 0

Rx Torsion (degrees): 0

○ Select merkels

Clicks right now do not label merkel cells.

Least Square Error: N/A

Click on corresponding cells, initial then final, in order to find a numeric value for least square error. Markers will not move. Instructions:

Press the start button when ready...

Note: maximum projections will not rotate and translate automatically.

tOverlay2120524_004r_005g

**Figure 4.2**: *Global registration of DAPI-labeled bodies across follicle experiments.* (A) Graphical user interface for registration of DAPI stained volumes before and after deflection. See text for a description of the registration method. (B-C) Maximal projections of pre- (B) and post- (C) registration volumes in all three planes. The overlap of DAPI bodies from the two volumes appears as yellow.

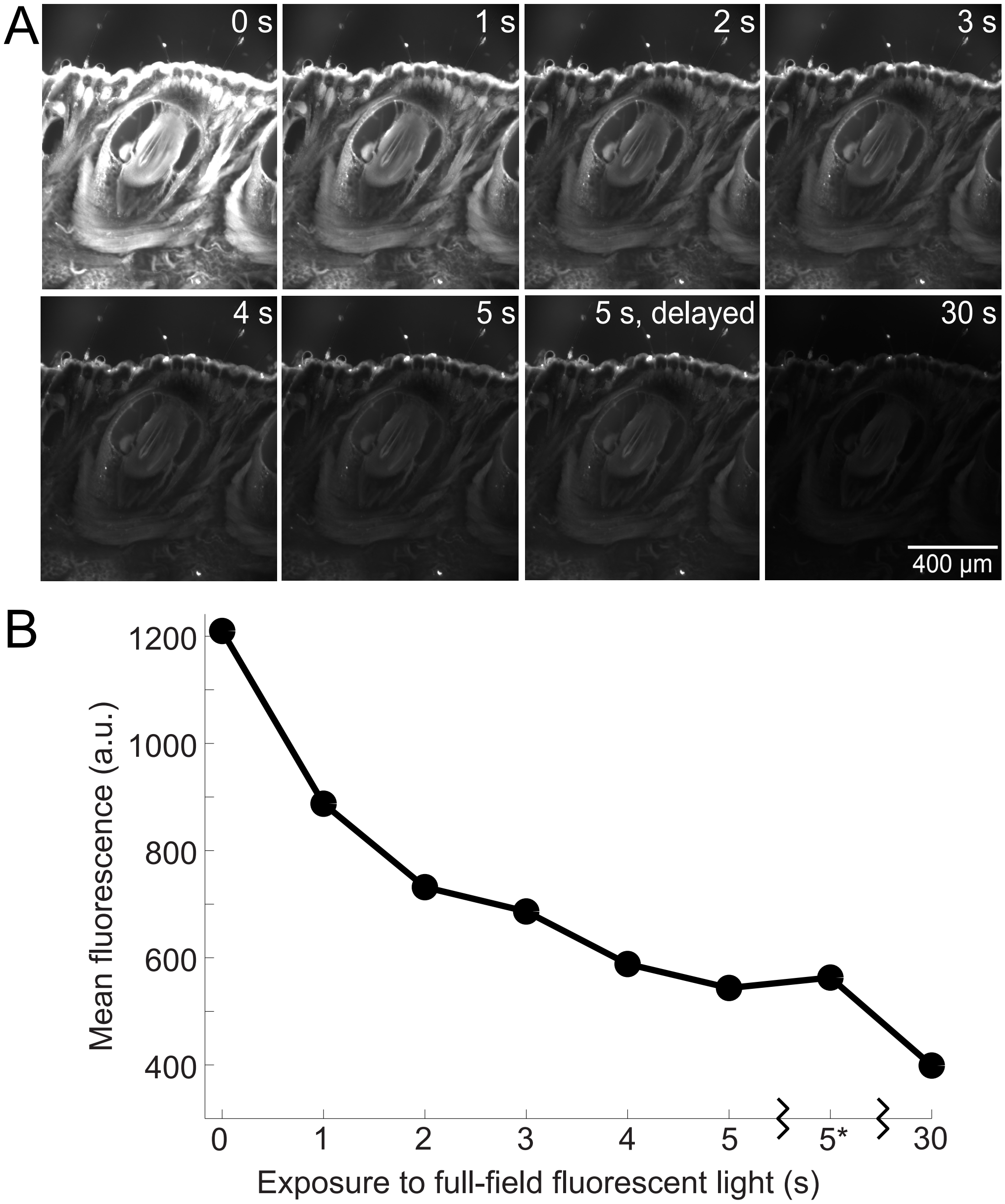

**Figure 4.3**: *Bleaching of 5-hexadecanoylamino-fluorescein.*

(A) An example follicle stained with 5-hexadecanoylamino-fluorescein and imaged with a full field Xenon lamp at indicated time points. At 5 s, the light was removed and the tissue was permitted to recover; after 5 s, the light returned until a full 30 s time point was reached. (B) Mean fluorescence of the full field image at each indicated time point. Mean fluorescence was computed across each image frame, though this underestimates the total bleaching effect.

is downregulated following axotomy [Lazarov, 2002], we reasoned that parvalbumin might appear in follicle terminals from Vg afferents. Accordingly, Merkel cells expressed parvalbumin strongly and exclusively within the follicle (Fig. 4.4A-B). There was some slight labeling of innervation by the deep vibrissal nerve visible (Fig. 4.4A). Because none of the other receptor endings were well labeled, this could be a useful transgenic line for the exclusive study of Merkel cells; however, we moved to other approaches to visualize more than one receptor type.

We next tested a line of mice expressing the fluorescence resonance energy transfer (FRET)-based calcium sensor TN-XXL under expression by the pan-neuronal promoter Thy-1 [Heim and Griesbeck, 2004, Heim et al., 2007]. These follicles showed high expression in many receptors, including Merkel cells, lanceolate endings, the rete ridge collar, and the ringwulst, as well as in tissue outside of the FSC (Fig. 4.4C). Counterstaining with DAPI (blue) showed strong labeling throughout the follicle and surrounding tissue (Fig. 4.4C). Thy1-TN-XXL expressed in the receptors could be used to image calcium activity; however, tissue showed high background fluorescence, and its use merely as a reporter line for receptor endings was unnecessary.

Finally, we loaded the small styryl dye FM1-43, which is known to enter mechanotransduction channels and primary trigeminal axons [Meyers et al., 2003,Fukuda et al., 2003], and found strong labeling in many receptor endings (Fig. 4.5). FM1-43 labels many sensory endings, including longitudinal lanceolate endings, Merkel neurites and Merkel cells, club-like endings, and reticular endings (not shown); DAPI generates punctate labeling throughout the elements of the follicle, as before, and labels Merkel cells. This promiscuous DAPI staining is useful because it permits straightforward image analysis of local deformations throughout the FSC. Because of the quality and ease of FM1-43 and DAPI labeling and the fact that no transgenic animals were necessary, we chose these methods to visualize follicle receptors and components.

### 4.4.2 Vibrissa displacement effects receptor location

We displaced the vibrissa in two systematic ways. First, because Vg neurons respond physiologically with great reliability to axial movements (those along the vibrissa shaft) [Stüttgen et al., 2008], we displaced the vibrissa axially away from the skin by

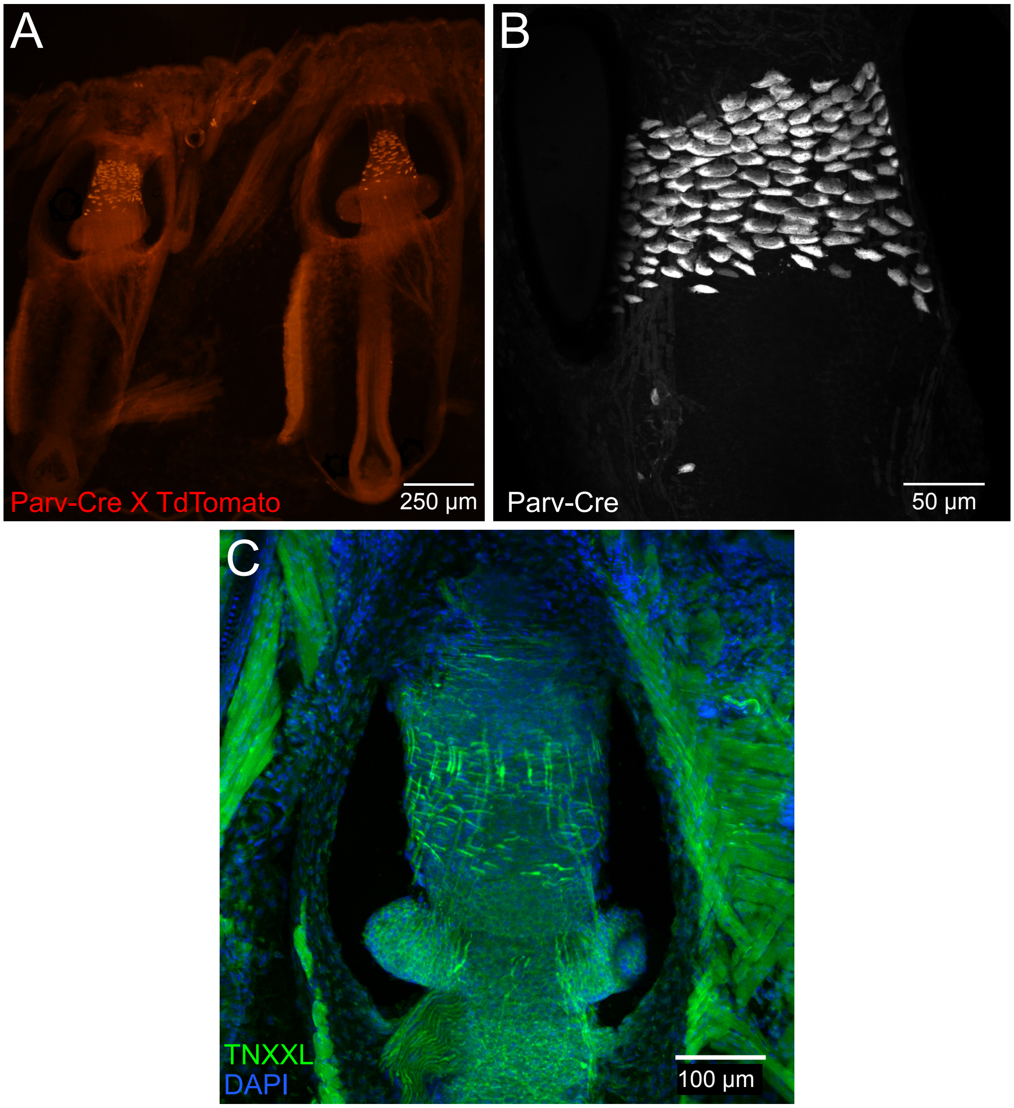

**Figure 4.4**: *Labeled follicle receptors in PvCre-TdTomato and TN-XXL mouse lines.* (A) Two follicles, showing strong labeling primarily in Merkel cells (intrinsic RFP fluorescence). 60 $\mu$m slice under upright full field illumination. (B) Maximum z-projection through a 48 $\mu$m confocal stack of the upper layer of a single follicle from a vibrissa pad slice. Merkel cells are exclusively and robustly labeled. In both A and B, the distal portion of skin is facing upward. (C) Maximum z-projection through a 58 $\mu$m confocal stack of the upper layer of a single follicle from a vibrissa pad section of a Thy1-TN-XXL adult mouse (intrinsic fluorescence of both CFP and YFP, green), counterstained with DAPI (blue). The distal portion of skin is facing upward.

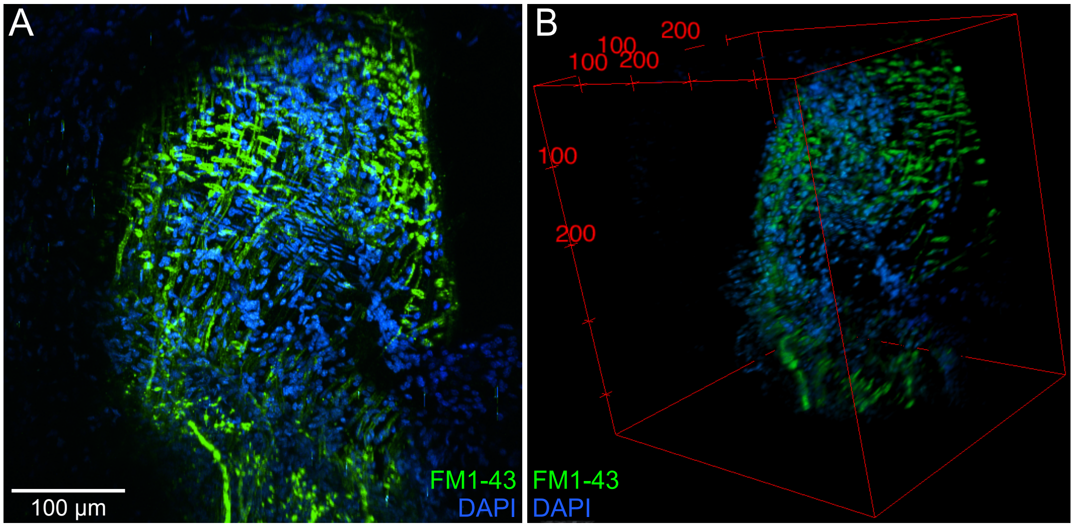

**Figure 4.5**: *FM1-43 and DAPI label many receptors in the follicle*.
(A) Maximum z- projection through a 360 $\mu$m volume of an intact single follicle (left C1) imaged under two photon. FM1-43 (green), DAPI (blue). The vibrissa is pointed upward. (B) Volume of the follicle in three dimensions, viewing from the dorsorostral aspect. Scale indicated on bounding box. The vibrissa is pointed upward.

180 $\mu$m (Fig. 4.6). Interestingly, while the majority of receptors and gross structure did not change locations, the longitudinal lanceolate endings elongated greatly in the axial dimension. Lanceolate endings produce rapidly adapting (RA) responses in Vg [Iggo and Ogawa, 1977], and axial displacement of vibrissae results in a large proportion of RA responses [Stüttgen et al., 2008]; therefore, the mechanical deflections we see are consistent with responses seen physiologically.

Second, primary afferents respond strongly to latitudinal vibrissa deflections [Lichtenstein et al., 1990]; therefore, we deflected vibrissae in eight cardinal and ordinal directions at 10°, 20°, or 30° angles. In order to focus on local deformations in the tissue, we globally registered the follicle image stacks using DAPI fluorescence (see Sec. 4.3). We then computed the movement vectors for each DAPI-stained point across conditions and averaged these vectors in $\sim 50$ $\mu$m blocks to evaluate the patterns of follicle tissue deformations. Strikingly, deflections in opposite directions cause reliable compression and dilation of the tissue. For example, when the left C1 vibrissa is deflected caudally, follicle receptors tend to move toward the vibrissa; when deflected

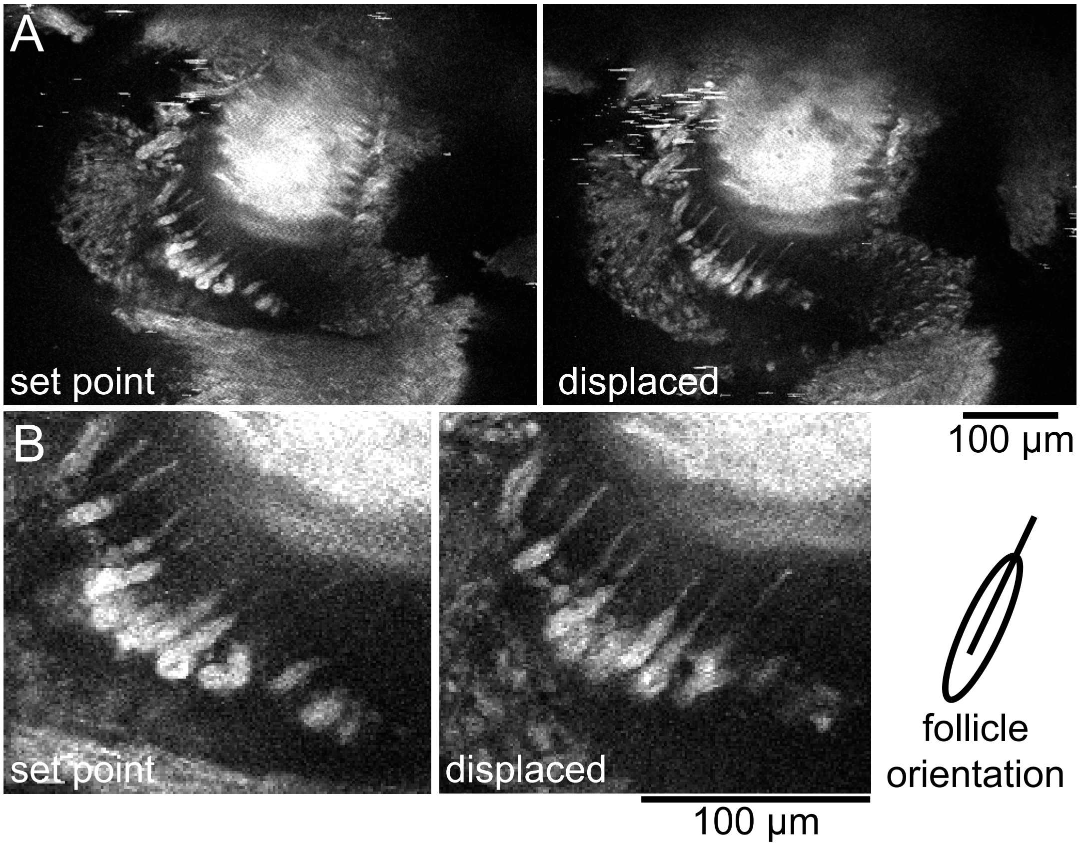

**Figure 4.6**: *Axial displacement of vibrissa.*

(A) Location of receptors with vibrissa in its resting position “set point” and displaced axially by 180 $\mu$m (“displaced”). (B) Magnified image focusing on the local changes to axons putatively terminating as lanceolate endings. The follicle schematic shows correct orientation for both panels.

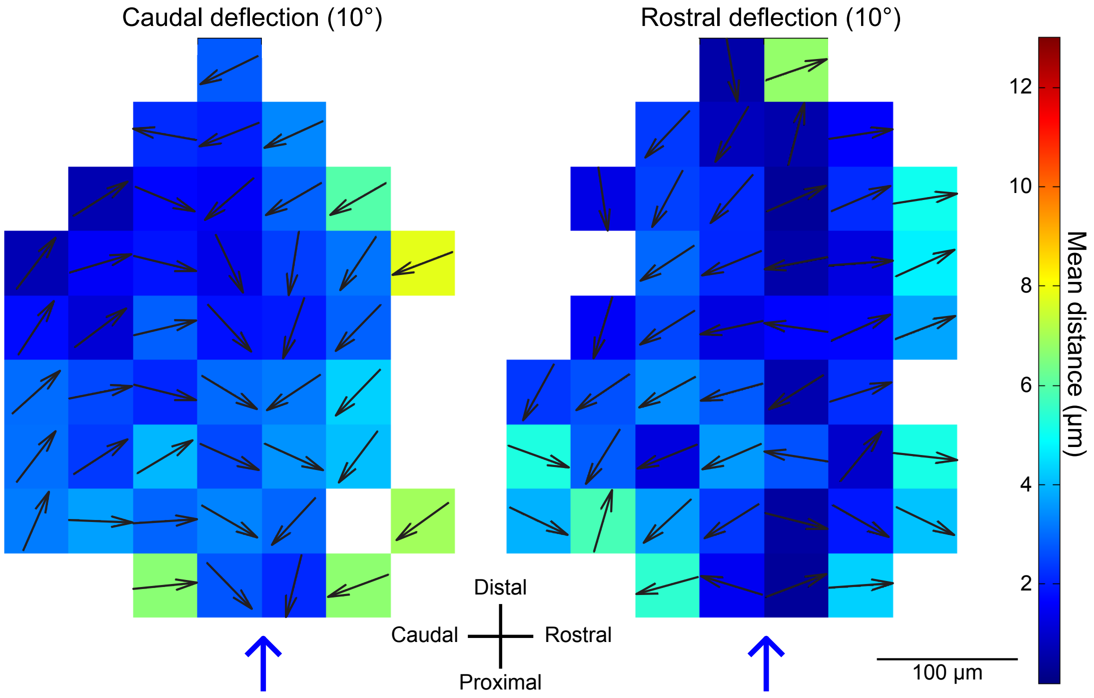

**Figure 4.7**: *Rostral and caudal displacement of vibrissa.*
Vector fields of the mean direction and amplitude of DAPI-stained receptors in response to vibrissa deflection. The vibrissa location is indicated by the blue arrow; this example is from the left C1 vibrissa. The vibrissa is pointed in the distal direction, away from the skin. Color indicates the mean distance that the vectors move for a given block. These results are computed for the data shown registered in figure 4.2.

rostrally, they tend to move away from the vibrissa (Fig. 4.7). The mean movement of receptors tends to increase farther from the vibrissa, near to the ring sinus. The amplitude of this effect grows with the angle of vibrissa displacement, though the variance among mean vectors also increases (data not shown).

## 4.5 Discussion and Future Directions

We have presented a novel preparation for imaging the movement of receptors in response to vibrissa deflection under two photon microscopy. We identified fluorescent markers, specifically DAPI and FM1-43, that reliably label many or all of the primary receptor endings and Merkel cells in the FSC. We found that outward axial displacement of the vibrissa causes elongation specifically of the axons innervating lanceolate endings but not of other parts of the tissue. Further, we demonstrate that rostral and caudal deflections have opposing effects on the movement of receptors, especially at the edge of the mesenchymal sheath, close to the ring sinus. These data are preliminary, but demonstrate the utility of this preparation for the study of a complex sensory organ that has historically been approached only with electrophysiology and histology.

Past behavioral and physiological studies suggest several extensions of the experiments we have performed with this preparation. First, rodents naturally detect the radial distance of stimuli along the shaft of their vibrissae, with rats having a radial acuity of $\sim 3$ mm [Krupa et al., 2001, Shuler et al., 2002]. Physiologically, Vg neurons report increased radial distance from the skin with a decrease in firing rate when a stimulus is encountered during active touch [Szwed and Ahissar, 2006, Ahissar and Knutsen, 2008]. These data imply that radial distance could be encoded at the level of the periphery, and would therefore be interesting to examine in this preparation.

While we have identified one approach to gaining optical access to the receptors for high resolution imaging, the surgical introduction of a window in the follicle capsule could disrupt the natural mechanics and kinetics of the system because of disruption of blood pressure in the ring sinus abutting the receptors. Further, the follicle is imaged *ex vivo*, so the properties of the tissue may not generalize to the intact system. To overcome these challenges, it would be interesting to pursue different imaging modalities besides two photon microscopy. We assessed the possibility of optical coherence tomography for this application; however, the resolution was poor at depths necessary for receptor visualization ($> 1$ mm below skin; data not shown). Another possibility is X-ray-based imaging, which resolves differences in tissue densities. If the spatial resolution is sufficient to identify parts of the FSC, then two experiments are of immediate interest. First, we could passively deflect the vibrissa in the anesthetized animal, and examine how the follicle and its components move. Second, if the temporal resolution is also sufficient, we could evaluate the mechanical relationship between the follicle and the vibrissa during whisking and in response to active contact with a stimulus.

Finally, imaging the physiological activity of follicle receptors in response to vibrissa deflection would provide critical insight into how vibrissa parameters are encoded. The pan-neuronal expression of the Thy1 promoter results in transgenic expression of the [$\mathrm{Ca}^{2+}$] indicator TN-XXL in follicle receptors (Fig. 4.4), making this line a viable option. Alternative approaches for labeling receptors with [$\mathrm{Ca}^{2+}$] sensors would include bath application or trigeminal ganglion injection of organic indicators, such as OGB-1-AM.

*We thank Fan Wang (Duke University, NC) for the use of an initial line of PvCre(Tdtomato) mice, Oliver Griesbeck (Max Planck Institut für Neurobiologie, Martinsried, Germany) for the use of the TN-XXL line of mice, Ellen Lumpkin (Columbia University, NY) for an FM1-43 labeling protocol, and Frank Rice (Albany Medical College; Intidyn, LLC, NY) for useful discussions. This chapter is preliminary, but will, in part, likely result in submission. The dissertation author will be a first author or coauthor of this paper, and likely coauthors will include Samuel Whiteley, Per M. Knutsen, and David Kleinfeld.*

# Chapter 5

# Conclusion

In this dissertation, I have combined recent developments in molecular and viral tools, computational techniques, and imaging technologies to further our understanding of the neural substrates for sensation and behavior.

Focusing on the mouse vibrissa system, I have examined the initial transduction mechanics of somatosensation in the follicle, revealed principles of organization from genomic analysis of the trigeminal brainstem, and anatomically dissected the components of a novel brainstem circuit that mediates fast, sensorimotor feedback for the sensory-driven modulation of whisking behavior.

Each of these studies immediately suggests exciting future experiments, which I detail in the discussions of their respective chapters. These experiments, not possible without the insights that the data have provided on the underlying circuitry of the trigeminal-facial system, include the functional and molecular interrogation and manipulation of the follicle sinus complex encoding sensory information, the polysynaptic brainstem circuitry mediating sensorimotor behaviors, and the genetic logic determining brainstem circuit architecture.

As the repertoire of available neuroanatomical tools continues to grow, the grand challenge of neuroscience to understand brain connectivity will further constrain and, in concert with functional techniques, perhaps fully reveal the principles that govern neural systems.

# Appendix A

# Automatic identification of fluorescently labeled brain cells for rapid functional imaging

## A.1 Abstract

The online identification of labeled cells and vessels is a rate-limiting step in scanning microscopy. We use supervised learning to formulate an algorithm that rapidly and automatically tags fluorescently labeled somata in full-field images of cortex and then constructs an optimized scan path through these cells. A single classifier works across multiple subjects, regions of the cortex of similar depth, and different magnification and contrast levels without the need to retrain the algorithm. Retraining only has to be performed when the morphological properties of the cells change significantly. In conjunction with two-photon laser scanning microscopy and bulk-labeling of cells in layers 2/3 of rat parietal cortex with a calcium-indicator, we can automatically identify $\sim$50 cells within one minute and sample them at $\sim$100 Hz with a signal-to-noise ratio of $\sim$10.

## A.2 Introduction

*In vivo* two-photon laser scanning microscopy (TPLSM) of brain cells labeled with a functional indicator is a powerful and increasingly popular method to probe neural function. This approach, for example, enables the simultaneous detection of intracellular $Ca^{2+}$ changes in populations of neurons and astrocytes within the middle to upper layers of the rodent cerebral cortex [Kerr et al., 2005, Ohki et al., 2005]. Yet it has been a challenge to achieve high temporal resolution across regions of cortex as only one voxel is measured at a time. The limit on temporal resolution for functional imaging arises not from an inability to scan the laser beam more rapidly, but rather from the efficiency of two-photon excitation of the dye and the need to avoid damage to tissue from high laser powers.

When cells of interest occupy only a small fraction of the field of view, one means to increase the sampling rate is to scan along an arbitrary path that passes cyclically through the cells of interest [Göbel and Helmchen, 2007, Göbel et al., 2007, Lillis et al., 2008, Rothschild et al., 2010], rather than scanning the entire field with a raster pattern. The rate-limiting step to determine the scan path through a large number of cells is the need to manually annotate the location of all somata. Automatic identification of somata in TPLSM images is a challenge due to low signal-to-noise ratios associated with images deep within the cortex and differences in the fluorescence intensity of cells caused by uneven uptake of dye. Traditional spatial segmentation approaches that use handmade morphometric filters do not generalize across preparations. In particular, because of the need to differentiate between cell somata, blood vessels, and unusually bright areas of neuropil, approaches that segment based solely on time-averaged intensity or predetermined masks do not perform well. Further, techniques that focus on temporal variation are effective for disentangling cells in populations of asynchronously active neurons and astrocytes, but fail to detect cells that do not spike or to differentiate cells that spike synchronously [Mukamel et al., 2009, Ozden et al., 2008, Sasaki et al., 2008].

Here we address the issue of rapid scanning with a cell segmentation algorithm that utilizes machine learning to automatically identify the location of somata and an optimized scan algorithm to compute a scan path that preferentially passes through labeled somata while minimizing the time spent scanning neuropil and unidentified tissue. This approach can incorporate scans across and along cerebral blood vessels [Schaffer et al., 2006] to permit simultaneous measurements of neuronal activity, astrocytic activity, and blood flow. While arbitrary scanning has been previously implemented for functional imaging by TPLSM [Göbel and Helmchen, 2007, Göbel et al., 2007, Lillis et al., 2008, Rothschild et al., 2010], our approach further optimizes the scan pattern and integrates it with automated segmentation.

## A.3 Methods

### A.3.1 Experimental methods

#### A.3.1.1 Animal preparation

Our subjects were Sprague Dawley rats from Charles River, ranging in mass from 270 to 310 g. Initial surgeries were performed under isoflurane (Baxter Healthcare) anesthesia, with 4 % (v/v) in 30 % oxygen and 70 % nitrous oxide for induction and 1 to 2 % (v/v) for maintenance. Craniotomies were placed over the hindlimb representation of the somatosensory cortex, with a window size of $\sim 4 \times 4$ mm centered at 2.5 mm medial-lateral and $-1.0$ mm anterior-posterior, as described [Kleinfeld et al., 1998, Shih et al., 2009]. A metal frame that supports a window made from a no. 1 cover slip was mounted above the craniotomy and filled with 1.5% (w/v) agarose in an artificial cerebral spinal saline [Kleinfeld and Delaney, 1996]. Catheters were placed in the femoral artery for continuous measurement of blood pressure (BP-1; World Precision Instruments), and withdrawal of arterial blood for blood gas analysis (RapidLab 248; Bayer). The femoral vein was separately catheterized for drug and anesthetic delivery. Isoflurane was discontinued prior to imaging, and anesthesia was transitioned to $\alpha$-chloralose with an intravenous bolus injection of 50 mg/kg for induction, and a steady flow of 40 mg/kg/h for maintenance [Devor et al., 2008]. Body temperature was maintained at 37°C with a feedback-regulated heat pad (50-7053-F; Harvard Apparatus). Heart rate and blood oxygen levels were continuously monitored using a pulse oximeter (8600V; Nonin). Intraperitoneal injections of 5% (w/v) glucose in 1 mL saline were given every 2 hours to prevent dehydration. The care and experimental manipulation of our mice and rats have been reviewed and approved by the Institutional Animal Care and Use Committee at the University of California at San Diego.

#### A.3.1.2 Somatosensory cortex mapping

We mapped the hindlimb region of the somatosensory cortex using intrinsic optical imaging of blood oxygenation, as described [Drew and Feldman, 2009,Masino et al., 1993]. The contralateral hindlimb was electrically stimulated with 1 mA, 10 ms wide pulses delivered at 3 Hz for 3 s [Devor et al., 2008]. Images were acquired with a 12-bit CCD camera (1M60, Dalsa) with a macroscope composed of camera lenses [Ratzlaff and Grinvald, 1991]. An initial image of the cortical vasculature was taken using 430 nm illumination to provide a map for dye injections. The cortical surface was then illuminated at 630 nm and images of a 3 by 3 mm field, at 1024 by 1024 pixel resolution, were obtained at 58 frames/s and binned into 256 by 256 pixel images at 2 frames/s for analysis.

#### A.3.1.3 Calcium dye injection and imaging

*In vivo* two-photon imaging was performed using the membrane-permeant Ca2+ indicator OGB1-AM (Invitrogen) as described [Stosiek et al., 2003]. Briefly, OGB1-AM was dissolved in 20 % (w/v) Pluronic F-127 in DMSO to a concentration of 10 mM. This solution was diluted 1:10 with a buffered saline, 150 mM NaCl, 2.5 mM KCl, and 10 mM HEPES at pH 7.4, to yield a final dye concentration of 1 mM for loading into a micropipet tip. The cover slip over the cranial window was removed, the electrode was lowered into the appropriate region of cortex, and the dye was then pressure injected, at 0.07 bar for 1 to 5 s, into the hind-limb somatosensory cortex at a depth 250 to 300 $\mu$m below the pial surface. The pipette was left in place for 5 minutes to allow equilibration of the dye with the tissue, then removed. The exposed cortical surface was then incubated with 50 $\mu$M sulforhodamine 101 (SR101, Sigma) in buffered saline for 10 minutes to label cerebral astrocytes [Nimmerjahn et al., 2004]. Finally, the cranial window was resealed. All imaging was performed with a two-photon microscope of local design [Tsai et al., 2009] using a 40× dipping objective and galvanometric scan mirrors (6210H scanners with MicroMax 673xx dual-axis servo driver; Cambridge Technology), and MPScope [Nguyen et al., 2006, Nguyen et al., 2009] for acquisition and control. The optimized scan algorithm is readily integrated with this software. The excitation wavelength was 800 nm and the collection band of OGB1 fluorescence was 350 to 570 nm and that of SR101 was 570 to 680 nm. Images were 256 by 256 pixels or 400 by 256 pixels in size and a time-series consisted of 200 frames collected at 5 or 10 Hz. Two sensory stimulation protocols were used in conjunction with the imaging. A single 10 ms stimulus was applied to the hindlimb to induce neuronal responses, while thirty 10 ms pulses readily induced changes in both neuronal activity and blood flow.

### A.3.2 Computational methods

#### A.3.2.1 Implementation of the cell segmentation algorithm

The algorithm was implemented in MATLAB code and C++ code compiled into MEX, i.e., MATLAB accessible, libraries. RobustBoost, which is an improved version of the Adaboost algorithm, was used as realized in JBoost version 2.0r1, freely available at jboost.sourceforge.net. The output classifiers generated by JBoost take the form of MATLAB .m files. Cross-validation and other classification metrics were evaluated using Python and Perl scripts distributed with JBoost; we note that nfold.py, VisualizeScore.py, and atree2graphs.pl are particularly useful. All calculations made use of a workstation with an Intel® Pentium® D Processor with 4 MB of cache memory and a 3.2 GHz clock speed.

Our realization of the algorithm is organized into five principle parts: (i) Training code to generate the first step classifier; (ii) Annotation and training code to help annotate and then generate the second step classifier; (iii) Segmentation code whose input is full-field TPLSM images and whose output is the result of the second classifier; (iv) PathGUI code that interacts with the segmentation code to find cells, construct an optimized path through them, and interacts with the TPLSM control software; and (v) PathAnalyzeGUI code that is used as a quick analysis tool to check the accuracy of the path. Additional analysis code was developed to segment raw scan data, identify onset times, and automatically differentiate astrocytes from neurons.

The training code used to generate the first step classifier takes full-field TPLSM data as input. Adobe Photoshop$^{TM}$ was used to perform annotations. Not all pixels that are parts of cells need to be annotated, but modest care must be taken to avoid labeling pixels inaccurately. The annotation and training algorithm that is used to generate the second step classifier uses the output of the first step classifier after it is thresholded at multiple levels. A graphical user interface was developed to assist annotation. For each candidate cell produced, the annotator is presented its outline and can choose whether the outline segments a cell, not a cell, or an ambiguous region.

Both classifier training codes interact with JBoost using command line calls from MATLAB. The RobustBoost algorithm requires three parameters to be chosen. The first parameter, $rb_{epsilon}$, characterizes the expected amount of error in the annotations of the training set; the default value is 0.1. The second parameter, $rb_{theta}$, characterizes how much separation is desired between two classes; the default value is 0. The third parameter, $rb_{sigma}$, characterizes how the potential function changes with time; the default value is 0.1. To construct the first classifier, $rb_{epsilon}$ was set to 0.15, $rb_{theta}$ was set to 0.2, and $rb_{sigma}$ was set to 0.1. To construct the second classifier $rb_{epsilon}$ was set to

0.06, $rb_{theta}$ was set to 0.1, and $rb_{sigma}$ to 0.1. The final decision tree contains hundreds of nodes, each with a tunable threshold on a particular feature.

The final classifier is relatively insensitive to the exact values of the parameters. Two parameters, $rb_{theta}$ and $rb_{sigma}$, can be changed by a factor of two to three with negligible effect. The most critical parameter is $rb_{epsilon}$, which corresponds to the fraction of expected errors in the annotation. This parameter should be set to the lowest number for which the algorithm converges, We used the training error found after 300 rounds of training with LogitBoost [Friedman et al., 2000] to estimate this number. LogitBoost is a common boosting procedure with no adjustable parameters apart from the number of training rounds and produces slightly smaller training error than RobustBoost but has a greater test error. In practice, the value of $rb_{epsilon}$ may be changed by a factor of 1.1 to 1.2 with little effect on the test error. If the parameter $rb_{epsilon}$ is set too low, RobustBoost does not converge.

#### A.3.2.2 Optimized Scan Algorithm

The cell detection algorithm is integrated with a scan algorithm to generate a near optimal path between the segmented cells. The location and spatial extent of all cells are tabulated in terms of regions of interest (ROIs) formed by rectangular bounding boxes around each cell. This scan algorithm seeks to: (i) maintain a constant scan speed over regions of interest, such as segmented cells; (ii) scan each cell with a single straight line that, for computational simplicity, is restricted to cross the cell through the corners of a bounding box; (iii) maximize the speed of the scan when the laser is not passing though a region of interest; and (iv) minimize the total time along the path by optimizing the order in which cells are scanned. Mathematical details of the algorithm are given in section A.3.2.3.

The scan path is further optimized by rearranging the order in which the ROIs are scanned, as well as by selecting among one of four vectors that pass along the diagonals of each ROI, through the use of the ANT System algorithm [Di Caro and Dorigo, 1998]. The ANT System algorithm is used iteratively. Initially a large set of paths is generated through a search among nearest neighboring cells to minimizes the time it takes to go from one ROI to a specified second ROI, cycling among all ROIs. Once all of the possible paths are generated, they are weighed by the total distance of each path. This weighting determines the interaction energy between any two ROIs; the interaction energy is set to zero if no path exists between a given pair of ROIs. In the next iteration a modified nearest neighbor search is performed, this time the nearest neighbor is determined by a weighted function of the time it takes to move between a pair of ROIs and the interaction energy between the two sites. This process iterates, with the energy growing the more a path between two sites is used, until the ANT System algorithm converges on a final, optimized pathway among all sites.

All of the software presented in this paper will be available for download at physics.ucsd.edu/neurophysics/links.html.

#### A.3.2.3 Scan Path Considerations

The portions of the scan path that pass through the ROIs are created as straight lines, given by

$$P = P_0 + V_{linear} \cdot t$$

where P is a two-dimensional vector of voltages that specifies the deflection of the scan mirrors which in turn directs the beam. The parameter Po is the initial voltage and the parameter $V_{linear}$ is the slew (in V/ms), whose magnitude determines the time spent crossing the cell and whose direction is set by the diagonal of the bounding box. The paths through each ROI are connected by third-order polynomial splines that are constructed so that the scan path is continuous in both voltage and slew. This creates a physically realizable path that is followed by the scan mirrors with a constant delay, typically 80 $\mu$s for our scanners. The connecting paths between the ROIs are described by

$$P_{spline} = P_i + V_i \cdot t + C \cdot t^2 + D \cdot t^3$$

where for computational convenience, the spline is taken to start at $t = 0$ and end at $t = \pi$, the initial voltage $P_i$ and slew $V_i$ are set to match the position and velocity of the end of the ROI preceding the spline, and the parameters $C$ and $D$ are found from

$$C = \frac{3P_f}{\tau^2} - \frac{3P_i}{\tau^2} - \frac{2V_i}{\tau} - \frac{V_f}{\tau}$$

and

$$C = \frac{V_f}{3\tau^2} - \frac{V_i}{3\tau^2} - \frac{2C_i}{3\tau}.$$

The value of $\pi$ is the smallest positive real value that does not subject the mirrors to an acceleration larger than a hardware limit, denoted $m$, where typically $m = 100$ V/ms$^2$. Candidate values for the shortest possible spline length are found by setting the acceleration to $\pm m$ at the beginning and end of each spline, and finding all positive real values for $\pi$, i.e.,

$$0 = \pm m\tau^2 + (4V_f + 2V_i^2)\tau + (6P_i - 6P_f)$$

for acceleration at the start of a spline and

$$0 = \pm m\tau^2 + (4V_i + 2V_f^2)\tau + (6P_i - 6P_f)$$

for acceleration at the end of a spline. This leads to multiple values for $\tau$; we choose the smallest value that bounds the acceleration at the beginning and end of the spline but allows the mirrors to make positional errors on other parts of the spline (Fig. A.1).

Thus

$$\begin{aligned} |2C_x| &= m, \\ |2C_y| &= m, \\ |2C_x + 6D_x\tau| &= m, \text{ and} \\ |2C_y + 6D_y\tau| &= m. \end{aligned}$$

The total time spent scanning across the regions between ROIs was minimized by estimating the optimum order in which to scan the ROIs. This is a “traveling salesman” problem in terms of minimizing the time between ROIs, for which the ANT System algorithm [Di Caro and Dorigo, 1998] provides a robust and easily implemented approximate solution. Finally, the vector along the diagonals through each ROI is iteratively adjusted to further minimize the total time spent scanning across connecting sections.

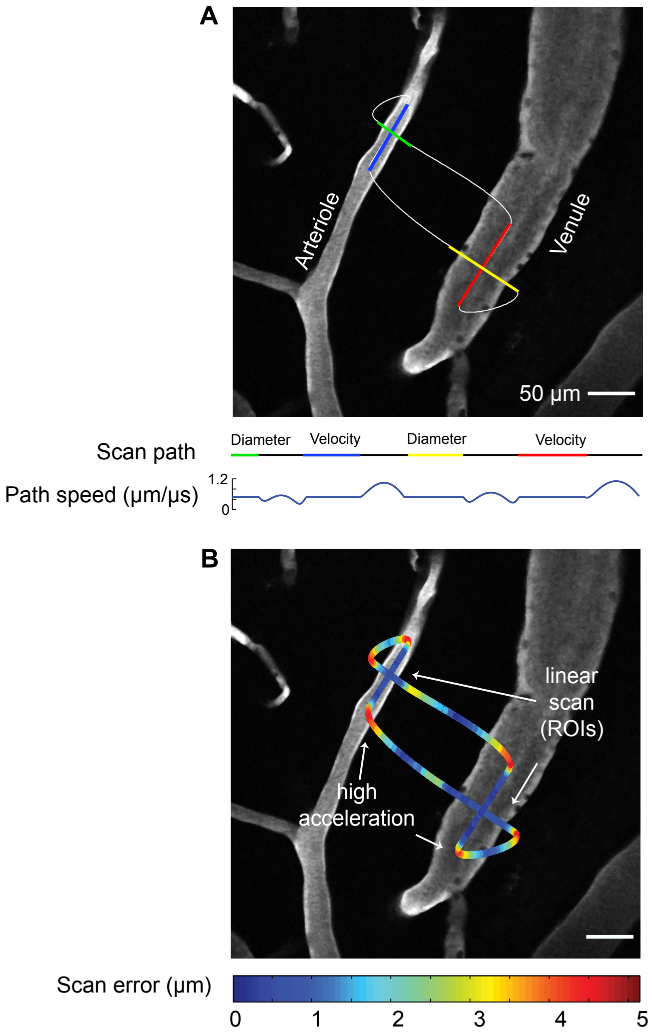

**Figure A.1**: *Illustration of line scan speeds and error in the measurement of blood flow.* (A) Image of an arteriole and venule on the cortical surface with the scan pattern superimposed. Portions of the scan path along the length are used to calculate the velocity of blood cells, while portions across the diameter of the vessels are used to calculate diameter. Scans were acquired at a rate of 735 Hz. The graph shows the galvometric mirror speed as a function of time. Portions used to acquire velocity and diameter data have constant speed while the connecting spline regions have variable speed. (B) Scan path, colored to show the error between the desired scan path and the actual path the mirrors traversed. The error along linear portions of the image is well below 0.5 $\mu$m, yet increases when the mirrors undergo rapid acceleration along the splines. The error between successive scans of the same path is less than 0.15 $\mu$m.

## A.4 Results

### A.4.1 Implementation

Cell segmentation consists of two classification steps. In the first step we classify individual pixels as to whether or not they are part of a cell. The pixels identified as being part of a cell are divided into connected elements that form candidate cells. In the second step we classify these connected elements as to whether or not they are indeed cell somata as opposed to other features. The first step yields a significant number of false positives. The second step removes most of these false positives and generates the final decision as to the locations of the cells. Both steps use classifiers generated by the RobustBoost algorithm [Freund, 2009], which is relatively insensitive both to explicit errors in human annotations and inconsistencies in labeling of ambiguous regions [Schapire et al., 1998]. RobustBoost is part of a family of machine learning algorithms called Boosting, which have been used in several biological image segmentation problems [Giannone et al., 2007,Liu et al., 2008]. The classifiers consist of a non-binary decision tree whose nodes correspond to thresholds on selected features and whose output is a score that corresponds to whether a given pixel is part of a cell. RobustBoost iteratively adds nodes and adjusts the thresholds to optimize the prediction given by the decision tree relative to the manually annotated images.

The first step classifier determines if a pixel belongs to a cell. The inputs to the classifier are feature maps that highlight the objects of interest in the TPLSM data. To identify cells, we chose eight heuristics that evaluate temporal and spatial differences, including mean values, variances, covariances, correlations, and normalized versions of these quantities (Fig. A.2). RobustBoost is used to generate the classifier, using as training data the full-field images of cortical regions in which pixels in the images are annotated as to whether they are part of a cell, not part of a cell, or if the determination is ambiguous. Once trained, the output from this classifier corresponds to a map of the score of a pixel being part of a cell. The output is median filtered to remove isolated pixels and thresholded at multiple levels to form connected elements that are candidate cells.

The second classifier scores whether a candidate cell is indeed a cell. This clas-

| Index | Feature map |
|---|---|
| 1 | $I^{Mean}_{x,y} = \left\langle \tilde{I}_{x,y}(t) \right\rangle$ §,† |
| 2 | $I^{Var}_{x,y} = \left\langle \left[ \tilde{I}_{x,y}(t) - I^{Mean}_{x,y} \right]^2 \right\rangle$ |
| 3 | $I^{Cov}_{x,y} = \sqrt{ \left\langle \left[ \tilde{I}_{x,y}(t) - I^{Mean}_{x,y} \right] \left[ \tilde{I}_{x+1,y}(t) - I^{Mean}_{x+1,y} \right] \right\rangle^2 + \left\langle \left[ \tilde{I}_{x,y}(t) - I^{Mean}_{x,y} \right] \left[ \tilde{I}_{x,y+1}(t) - I^{Mean}_{x,y+1} \right] \right\rangle^2 }$ |
| 4 | $I^{Corr}_{x,y} \equiv \sqrt{ \frac{ \left\langle \left[ \tilde{I}_{x,y}(t) - I^{Mean}_{x,y} \right] \left[ \tilde{I}_{x+1,y}(t) - I^{Mean}_{x+1,y} \right] \right\rangle^2 }{ I^{Var}_{x,y} \; I^{Var}_{x+1,y} } + \frac{ \left\langle \left[ \tilde{I}_{x,y}(t) - I^{Mean}_{x,y} \right] \left[ \tilde{I}_{x,y+1}(t) - I^{Mean}_{x,y+1} \right] \right\rangle^2 }{ I^{Var}_{x,y} \; I^{Var}_{x,y+1} } }$ |
| 5 | $I^{NormMean}_{x,y} = \frac{ I^{Mean}_{x,y} - \hat{I}^{Mean}_{x,y} }{ \hat{\sigma}^{Mean}_{x,y} }$ ‡ |
| 6 | $I^{NormVar}_{x,y} = \frac{ I^{Var}_{x,y} - \hat{I}^{Var}_{x,y} }{ \hat{\sigma}^{Var}_{x,y} }$ |
| 7 | $I^{NormCov}_{x,y} = \frac{ I^{Cov}_{x,y} - \hat{I}^{Cov}_{x,y} }{ \hat{\sigma}^{Cov}_{x,y} }$ |
| 8 | $I^{NormCorr}_{x,y} = \frac{ I^{Corr}_{x,y} - \hat{I}^{Corr}_{x,y} }{ \hat{\sigma}^{Corr}_{x,y} }$ |

§ $\left\langle I(t) \right\rangle \equiv \frac{1}{N} \sum_{t=1}^{N} I(t)$

† $\tilde{\boldsymbol{I}}(t) = \boldsymbol{I}(t) \otimes \boldsymbol{W}_5$, where $\boldsymbol{W}_n$ is a uniform filter of $n$ pixels.

‡ $\hat{\boldsymbol{I}}(t) = \boldsymbol{I}(t) \otimes \boldsymbol{W}_{21}$ and $\hat{\sigma}_{x,y} = \sqrt{ \sum_{x'=x-10}^{x+10} \sum_{y'=y-10}^{y+10} \left[ I_{x',y}(t) - \hat{I}_{x,y} \right]^2 } \Big/ \sqrt{(21)^2 - 1}$.

**Figure A.2**: *Feature map of time-series image data*

For cell identification in the first step of the classifier, we use eight heuristics that capture temporal and spatial differences in images. These include mean (1), variance (2), covariance (3), and correlation (4), and normalized versions of each (5-8).

| Index | Feature map |
|---|---|
| 1 | Threshold level at which the candidate is generated |
| 2 | The area of the candidate, in pixels |
| 3 | The Euler number, defined as the number of objects in the candidate minus the number of holes in those objects. |
| 4 | The extent, defined as the area of the candidate divided by the area of the bounding box. |
| 5 | The eccentricity of an ellipse that has the same second-moments as the candidate. |
| 6 | The solidity of the candidate, determined as the ratio of the area of the candidate to that of the associated convex hull. |

**Figure A.3**: *Feature map of intermediate cluster data*
For evaluating candidate cells in the second step of the classifier, we use six quantifiable morphological properties (1-6).

sifier takes as input a second set of feature maps computed from the output of the first stage, this time using six morphological properties (Fig. A.3). We again use RobustBoost with training data in which we annotate the output of the first classifier to identify candidate cells as cells, not cells, or ambiguous objects. The final likelihood map generated by the trained classifier is thresholded at or near zero and contains only connected elements that are likely to be cells.

We realized the cell segmentation algorithm by training the first and second classifiers using 64 different data sets, i.e., 16 different regions imaged with TPLSM over four trials each in four animals; see examples in figure A.4. Each data set consisted of 200 consecutive frames at a resolutions of 256x256 pixels or higher frames. Once the training was completed, we applied the cell segmentation algorithm to segment a test set. In all of our tests, we used a single classifier that was trained only once with annotated data from different regions of the cortex, different magnification and contrast levels, and different animals.

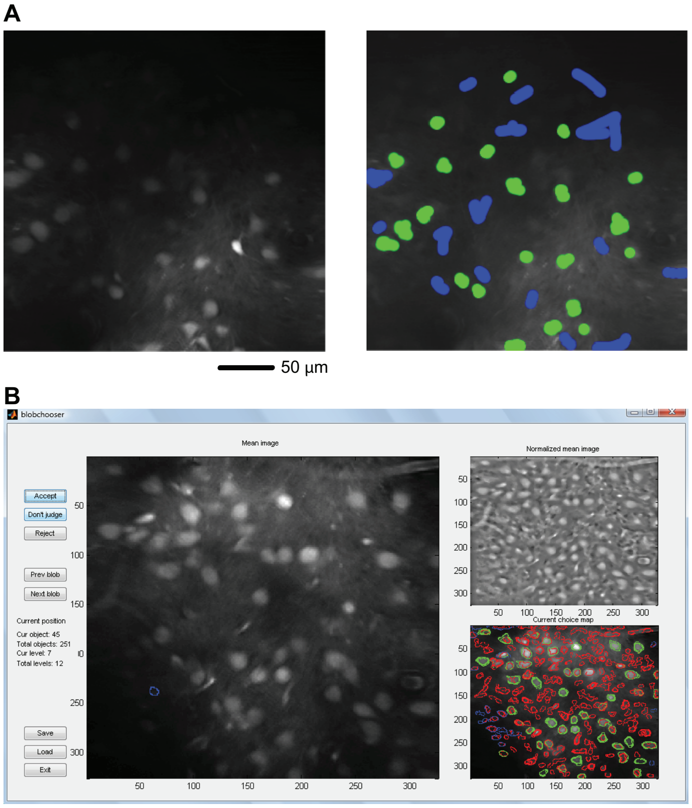

Current position
Cur object: 45
Total objects: 251
Cur level: 7
Total levels: 12

**Figure A.4**: *Examples of annotations used to generate the two classifiers.* (A) Example, shown raw and annotated, for the first classifier. This image is one of 16 full field annotated images. Since four trials were performed for each annotated region, these annotations were used in learning on 64 stimulation trials. Green indicates that the pixel is part of cell somata while blue indicates that it is uncertain whether a pixel is part of cell somata. All uncolored pixels are taken as examples of pixels that are not parts of cells. Notice that a very rough annotation was sufficient to produce good results. (B) Example to generate second classifier. A screenshot of a graphical user interface used to annotate whether a particular cluster of pixels is a cell, not a cell, or ambiguous region. On the left panel, a large mean image is shown with a current candidate cell outlined. Outlines that have not yet been evaluated are colored blue, those that were selected as not cells are colored red, those that have been selected as cells are colored green, and those that were selected as ambiguous regions remain colored blue. *Upper right:* a normalized mean image of the region. *Lower right:* a mean image with all of the previously made selections outlined with appropriate colors.

The application of our method to test cases is illustrated in the example of Figure 2, which shows the eight feature maps generated from the data (Fig. A.5 A) and the output from the first classifier (Fig. A.5 B); the thresholded version of this output, at multiple levels, is used as input to the second classifier. The output of the second classifier (Fig. A.5 C) is thresholded at zero to yield the segmented cells (Fig. A.5 D). In practice, it takes several hours of computer processing time to generate the classifiers for a particular preparation but only a few minutes to apply the algorithm and segment all cells in a sequence of images.

To evaluate the cell segmentation algorithm, a *k*-fold cross validation was performed for both the first and second step classifiers. A *k-fold* cross validation was done by lumping training sets from the 16 different brain regions and then partitioning the data into five equal sets (k = 5). Five different estimates for test error were then obtained by training on four of the five sets and using the remaining set to test. We observed an average estimated error of 0.07 (combined false positives and false negatives) for the test data. The area under the receiver operating characteristic (ROC) curve, a combined measure of method specificity and sensitivity, is 0.97 and is dominated by false positives (Fig. A.6). An examination of incorrectly classified cells shows that they predominantly occur in areas where it is difficult for a human expert to consistently label the cells.

### A.4.2 Application

As a proof-of-principle implementation of our algorithms, we performed over 200 trials of fast scanning measurements across 23 fields in primary somatosensory cortex that responded to stimulation of the hindpaw (n = 4 rats). The scan-mirror speed was adjusted so that the imaging time for each cell was about 200 $\mu$s per scan cycle, which yielded a signal-to-noise ratio sufficient to detect the nominal 10% fluorescence changes associated with calcium action potentials in neurons labeled with the indicator Oregon Green BAPTA (OGB1) [Dombeck et al., 2007,Kerr et al., 2005,Kerr et al., 2007, Komiyama et al., 2010,Ohki et al., 2005,Rothschild et al., 2010]. Recall that the calcium spikes are not necessarily associated with single sodium spikes, since previous work has shown that many sodium spikes can contribute to a single calcium spike [Greenberg et al., 2008]. We chose to study the upper layers of cortex for technical convenience and

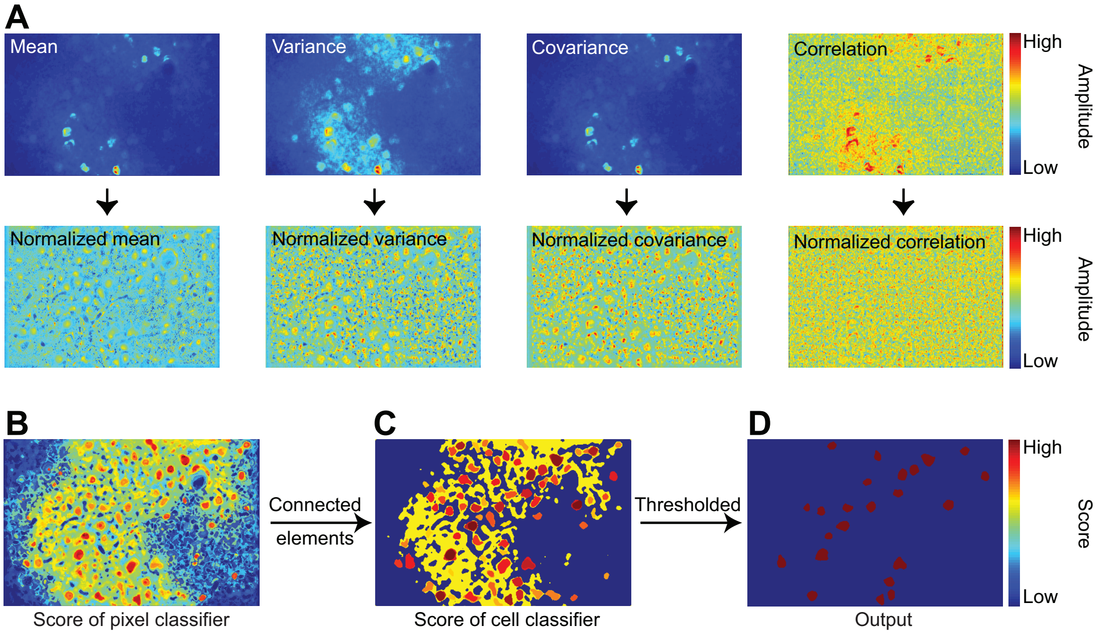

**Figure A.5**: *Example of segmentation of a test data set.*

(A) The four unnormalized filtered version of the raw data (A.2, formulas 1-4). The color corresponds to amplitude of the filtered output. The normalized versions of filtered images from panel A, (Table 1, formulas 5-8). (B) The output of the first classifier. The color corresponds to the likelihood that a given pixel is a cell. (C) The output of the second step classifier, with isolated pixels, i.e., speckle noise, removed with a 5x5 pixel median filter, along with the output values then thresholded to form clusters of pixels that are candidate cells; we chose six levels, which correspond to pixels lying in the top 5, 10, 15, 20, 25, and 30 percent of the maximum amplitude. (D) Final classification made by thresholding the output shown in panel C.

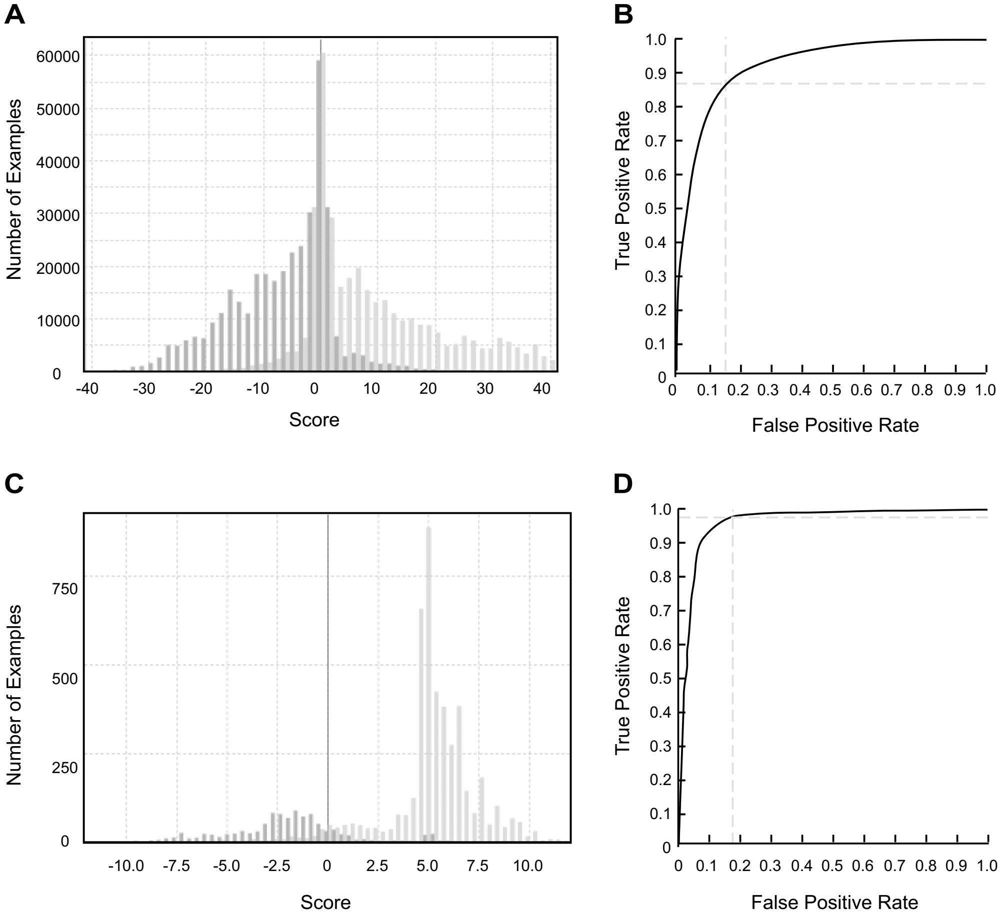

**Figure A.6**: *Validation statistics for the classifiers.*

(A) A histogram of cross-validated examples binned by the scores that they received from the first classifier. Black: examples of pixels that are parts of cells, gray: examples of pixels that are not parts of cells. (B) Receiver operating characteristic curve of the first classifier; the two dotted lines indicate the point on the ROC curve for which the score threshold is zero. Note that because ground truth is poorly defined, the ROC curve is only approximately representative of the real classifier errors. (C) A histogram of cross-validated examples binned by the score they have received from the second classifier. Black: candidate cells that are actually cells, gray: candidate cells that are not cells. (D) An ROC curve of the second classifier; the two dotted lines indicate the location on the ROC for which the score threshold is zero, which is the nominal final threshold for our algorithm. Note that because ground truth is poorly defined, the ROC curve is only approximately representative of the real classifier errors.

because different somata are well separated. Objects that overlap will be rejected, so that areas with extremely dense cells may be problematic and were thus avoided.

We present two typical examples of fast scanning in cortical layers 2/3 of rat somatosensory cortex with our approach. First, a region with 68 identified cells, 64 neurons and four astrocytes that was scanned at 70 Hz (Fig. A.8 A-D). Data was acquired for 10 minutes with only minimal photobleaching. Second, a region with 20 identified cells, 19 neurons and one astrocyte, along with three blood vessels, that was scanned at 110 Hz (Fig. A.8 E-H). Data was acquired for 4 minutes, again with only minimal bleaching. In both examples the cell segmentation algorithm was used in conjunction with full-field images from the OGB1 emission channel to determine all possible cell bodies (Fig. A.8 A, E; see also example in ) to an example of segmentation of 12 trials across four animals using the same classifier. Segmentation requires about one minute of computation and determination of the optimized pathway requires an additional 2 minutes. Cells that were co-labeled with the astrocytic marker sulforhodamine 101 (SR101) were automatically labeled as astrocytes; the coordinates of selected blood vessels were also marked. The optimized scan algorithm was then used to find the shortest cycle time through all cells (Fig. A.8 A, E), with $\sim$ 70% of the scan time spent over regions of interest, and a series of scan measurements were performed that encompassed periodic sensory stimulation (Fig. A.8 B, F). The typical signal-to-RMS-noise ratio for a change in intracellular calcium induced by a single sensory stimulus, which we define as the ratio of the peak value of the response to the value of the RMS noise during baseline activity, is $\sim$10 (Fig. A.8 C, G).

Our rapid segmentation process also facilitates online data analysis. For example, the average, trial-by-trial activity of all cells as a function of time after stimulation is readily calculated (Fig. A.8 D). As a second example, changes in astrocytic calcium levels together with changes in the speed of red blood cells in a nearby microvessel are readily compared with the composite neuronal activity (Fig. A.8 H).

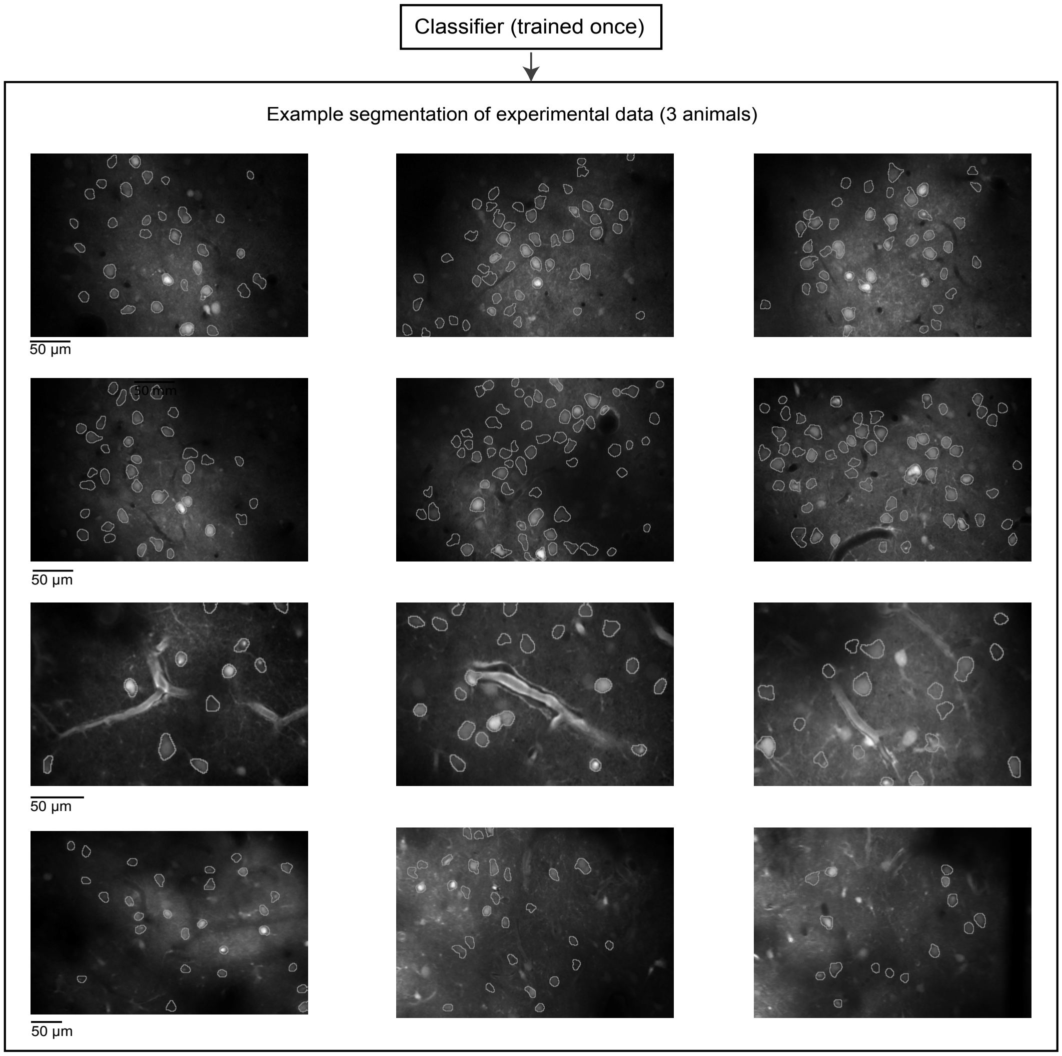

**Figure A.7**: *Illustration of cell bodies identified using a single classifier.* Borders of cells were identified in 12 regions from four animals and superimposed on top of the mean image for each region. Even though only a single training set was used, regions with different prominence of blood vasculature, zoom, and contrast were analyzed successfully.

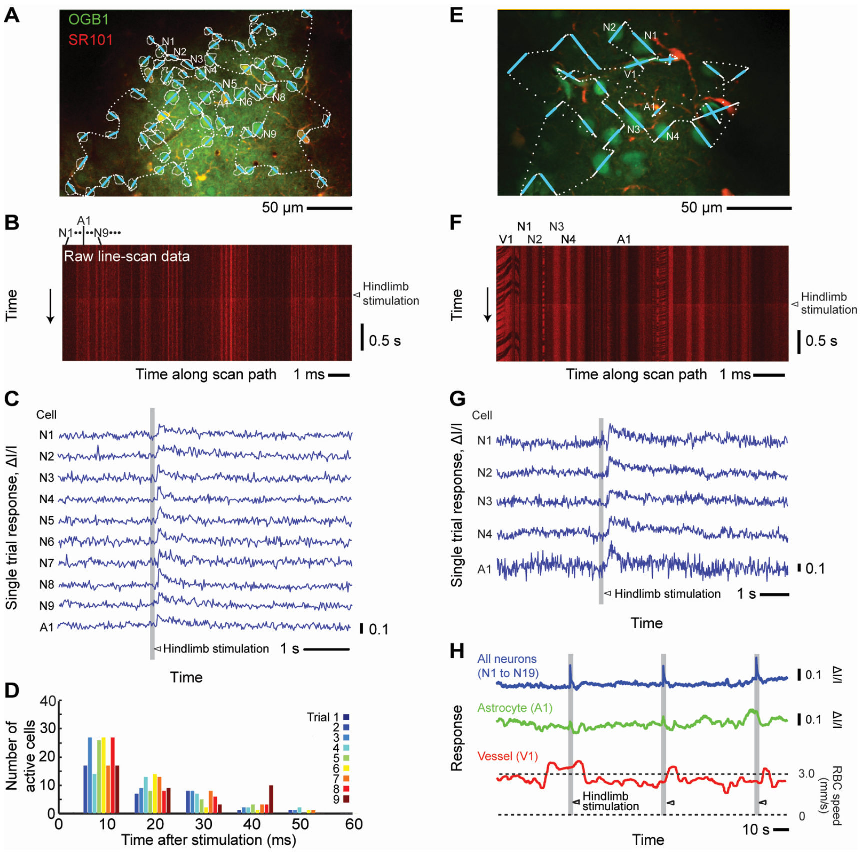

**Figure A.8**: *Two examples of cell segmentation and fast scanning for functional imaging of neurons and astrocytes in rat parietal cortex*

(A) Full-field image of region with 68 cells, obtained at 4 frames/s, with superimposed scan path; cells sampled at 70 Hz. White shows the outlines of algorithmically-determined cells. (B) Raw data output from consecutive scans, including hindlimb stimulation. (C) Activity of 10 cells, 9 neurons, and 1 astrocyte from A and B, during the same time interval as shown in B. Traces are shown in the order of the cells that were scanned. (D) Distribution of onset times for changes in intracellular [$Ca^{2+}$] in all 68 cells after stimulation across 9 trials. (E) Full-field image of 19 neurons, 1 astrocyte, and 3 blood vessels scanned at 110 Hz with superimposed scan path. (F) Raw data output that includes hindlimb stimulation. (G) Activity of cells, neurons, and an astrocyte indicated in E and F during the same time interval as shown in F. (H) The calcium response of the astrocyte (A1), the average neuronal response (N1 - N19), and the speed of red blood cells in one capillary (V1).

## A.5 Discussion

Our cell detection method can identify the borders of $\sim$70 cells in a 512x512 pixel image in one minute, which appears to be at least ten-fold faster than human annotation. This is crucial for studies that involve longitudinal measurements of somatic activation, such as developmental plasticity [Golshani et al., 2009, Rochefort et al., 2009], or swelling of the brain, such as experimental stroke [Sigler et al., 2009], where recalculation of the scan path compensates for shifts in the position of cells. As a practical matter, multiple cells and blood vessels may be monitored typically at rates that are ten-fold greater than those achieved with full-field images.

Optimization of the scan algorithm insures that the majority of time is spent over somata and blood vessels of interest. We chose to optimize with use of the ANT system algorithm [Di Caro and Dorigo, 1998]. This approach was chosen over gradient descent algorithms, genetic algorithms [Potvin, 1996], and convex hull algorithms [Nikolenko et al., 2007] because, for regions with order one hundred ROIs, the ANT system is relatively insensitive to internal parameters when computing the shortest pathway. Although there is no strong upper bound on the time for convergence of the ANT algorithm, the time increases slowly with an increase in the number of ROIs. The relatively high efficiency of this process may, in some instances, obviate the need to replace galvometric scanners with acousto-optical deflectors (AODs), and can also be combined with AODs for 3D scanning applications [Duemani Reddy et al., 2008, Vucinić and Sejnowski, 2007].

One potential limitation of optimized path scanning is that it is not compatible with schemes for correcting for motion artifacts [Dombeck et al., 2007]. This implies that our method should be primarily used on anesthetized animals. Nonetheless, the segmentation part of our approach can be used to do post-experiment analysis of full-frame images collected from behaving animals. This allows one to analyze in hours what could take weeks to do manually.

The insensitivity of our algorithm to correlated activity implies that it may be superior to correlation-based algorithms [Mukamel et al., 2009, Sasaki et al., 2008]. The natural capability of learning-based approaches, such as ours, to generate very complex morphological classifiers makes it superior to hand tuned approaches, albeit at the cost of obtaining and annotating training data. At the same time, our approach can make use of specialized filters, such as automatic spike train deconvolution [Vogelstein et al., 2010], to provide a fuller analysis of TPLSM data. Lastly, the use of compiled languages or specialized hardware may greatly decrease the computational time to segment the image data and compute an optimized scan path.

*This chapter, in full, is a reprint of the material as it appears in The Journal of Neurophysiology, 104 (3), 1803-1811, Valmianski, I.; Shih, A.Y.; Driscoll, J.D.; Matthews, D.W.; Freund, Y.; & Kleinfeld, D. (2010). The dissertation author was a coauthor of this paper.*

# Appendix B

# Table of abbreviations

| | |
|---|---|
| ABA | Allen Brain Atlas |
| ACSF | Artificial cerebrospinal fluid |
| ARA | Allen Reference Atlas |
| AGEA | Allen Gene Expression Atlas |
| AOD | Acousto-Optical Deflectors |
| API | Application programming interface |
| BAC | Bacterial artificial chromosome |
| C | Caudal (in figures) |
| C57BL/6 | Inbred, wild-type mouse line |
| CA1 | Cornu Ammonis-1 (hippocampus) |
| CA3 | Cornu Ammonis-3 (hippocampus) |
| Cck | Cholecystokinin |
| CDF | Cumulative distribution function |
| ChAT | Choline acetyltransferase |
| CNS | Central nervous system |
| Cre | Cre Recombinase |
| CTb | Cholera Toxin subunit b |
| D | Dorsal (in figures) |
| DAB | Diaminobenzidine |
| DAPI | 4’,6-diamidino-2-phenylindole |
| DEPC | Diethylpyrocarbonate, treatment for ISH procedure |
| DMSO | Dimethyl sulfoxide |
| Dynll2 | Dynein Light Chain LC8-Type 2 |
| EEM | Expression energy matrix |
| EMAGE | Edinburgh Mouse Atlas of Gene Expression |
| FG | Fluorogold |
| FM1-43 | Fluorescent small styryl dye |
| FRET | Fluorescence Resonance Energy Transfer |
| FSC | Follicle-sinus complex |
| GAD67 | Glutamate decarboxylase, isoform 1 (67 kDa) |
| Gapdh | Glyceraldehyde-3-phosphate dehydrogenase |
| GENSAT | Gene Expression Nervous System Atlas |
| GFP | Green fluorescent protein |
| GUI | Graphical user interface |
| HEPES | 4-(2-hydroxyethyl)-1-piperazineethanesulfonic acid |
| Hoxa5 | Homeobox gene A5; encodes homeobox protein A5 |
| ID | Inner diameter |
| IgG | Immunoglobulin G |
| ION | Infraorbital accessory of maxillary branch of trigeminal nerve |
| INCF | International Neuroinformatics Coordinating Facility |

| | |
|---|---|
| IRt | Intermediate reticular nucleus of the brainstem |
| ISH | *In situ* hybridization |
| L | Lateral (in figures) |
| LASSO | Least Absolute Shrinkage and Selection Operator |
| LoxP | Locus of X-over bacteriophage P1, a DNA recognition site |
| M | Medial (in figures) |
| MEX | MATLAB Executable file |
| mRNA | messenger ribonucleic acidÊÊ |
| NA | numerical aperture |
| NaCl | Sodium chloride |
| NDPI | Nanozoomer Digital Pathology Image, an image file format |
| Neu3 | Neuraminidase 3 |
| NHS | Normal horse serum |
| NLS | N-Lauroylsarcosine |
| NMF | Non-negative matrix factorization |
| Nrgn | Neurogranin |
| Nsf | N-ethylmaleimide-sensitive fusion protein/gene |
| OD | Outer diameter |
| OGB-1-AM | Oregon Green 488 BAPTA-1 AM Ester |
| P | Postnatal |
| PBS | Phosphate-buffered saline |
| PCA | Principal Components Analysis |
| PCRt | Parvocellular reticular nucleus, brainstem |
| PFA | Paraformaldehyde |
| PRV | Pseudorabies virus |
| PrV | Principal, or main, nucleus of the trigeminal |
| PvCre | Parvalbumin-Cre recombinase, transgenic mouse |
| RA | Rapidly adapting |
| Rasgrp1 | RAS guanyl-releasing protein 1 |
| recGFP | Reconstituted GFP |
| Ri | Right direction (in figures) |
| R/Ro | Rostral direction (in figures) |
| RNA | Ribonucleic acid |
| ROC | Receiver operating characteristic |
| ROI | Region of interest |
| SA | Slowly adapting |
| SD | Standard deviation |
| SDS | sodium dodecyl sulfate |
| SEM | Standard error of the mean |
| SG | Substantia gelatinosa |

| | |
|---|---|
| SNP | Single nucleotide polymorphism |
| SpV | Trigeminal spinal nuclei (SpVo, SpVi, SpVmu, and SpVc) |
| SpVc | Trigeminal spinal nucleus, Caudalis |
| SpVi | Trigeminal spinal nucleus, Interpolaris |
| SpVmu | Trigeminal spinal nucleus, Muralis |
| SpVo | Trigeminal spinal nucleus, Oralis |
| SR101 | Sulforhodamine 101 |
| SSC | Saline and sodium citrate |
| TdTomato | Tandem Dimer Tomato Fluorescent protein |
| Thy1 | Thymocyte antigen 1, promoter |
| TNL15 | Troponin-based [$Ca^{2+}$] sensor, first generation |
| TN-XXL | Troponin-based [$Ca^{2+}$] sensor |
| TPLSM | Two-Photon Laser Scanning Microscopy |
| Tuba1 | Alpha tubulin 1 |
| TRP | Transient receptor potential |
| Vbs | Trigeminal brainstem |
| Vg | Trigeminal ganglion |
| VIAAT | Vesicular inhibitory amino acid transporter |
| VGluT1 | Vesicular glutamate transporter type 1 |
| VGluT2 | Vesicular glutamate transporter type 2 |
| Vm | Trigeminal motor nucleus |
| Vn | Trigeminal nerve |
| VIIm | Facial motor nucleus |
| VIIn | Facial nerve |
| WGA | Wheat germ agglutinin |
| XFP | X fluorescent protein |
| XML | Extensible markup language |

# Bibliography

[Ahissar and Knutsen, 2008] Ahissar, E. and Knutsen, P. (2008). Object localization with whiskers. *Biological Cybernetics*, 98(6):449–458.

[Andermann et al., 2004] Andermann, M., Ritt, J., Neimark, M., and Moore, C. (2004). Neural Correlates of Vibrissa Resonance:: Band-Pass and Somatotopic Representation of High-Frequency Stimuli. *Neuron*, 42(3):451–463.

[Andres, 1966] Andres, K. H. (1966). Uber Die Feinstruktur der Rezeptoren an Sinushaaren. *Zeitschrift for Zellforschung*, 75:339–365.

[Angelucci et al., 1996] Angelucci, A., Clasca, F., and Sur, M. (1996). Anterograde axonal tracing with the subunit B of cholera toxin: a highly sensitive immunohistochemical protocol for revealing fine axonal morphology in adult and neonatal brains. *The Journal of Neuroscience Methods*, 65(1):101–112.

[Arabzadeh et al., 2005] Arabzadeh, E., Zorzin, E., and Diamond, M. E. (2005). Neuronal encoding of texture in the whisker sensory pathway. *PLoS Biology*, 3(1):e17.

[Armit et al., 2012] Armit, C., Venkataraman, S., Richardson, L., Stevenson, P., Moss, J., Graham, L., Ross, A., Yang, Y., Burton, N., Rao, J., Hill, B., Rannie, D., Wicks, M., Davidson, D., and Baldock, R. (2012). eMouseAtlas, EMAGE, and the spatial dimension of the transcriptome. *Mammalian Genome*, pages 1–11.

[Arshavsky and Burns, 2012] Arshavsky, V. Y. and Burns, M. E. (2012). Photoreceptor signaling: supporting vision across a wide range of light intensities. *The Journal of Biological Chemistry*, 287(3):1620–6.

[Arvidsson, 1982] Arvidsson, J. (1982). Somatotopic organization of vibrissae afferents in the trigeminal sensory nuclei of the rat studied by transganglionic transport of HRP. *The Journal of Comparative Neurology*, 211(1):84–92.

[Åström, 1953] Åström, K. E. (1953). On the central course of afferent fibres in the trigeminal, facial, glossopharyngeal, and vagal nerves and their nuclei in the mouse. *Acta Physiologica Scandinavica*, 29(Supp106):209–320.

[Avendaño et al., 2005] Avendaño, C., Machín, R., Bermejo, P. E., and Lagares, A. (2005). Neuron numbers in the sensory trigeminal nuclei of the rat: A GABA- and glycine-immunocytochemical and stereological analysis. *The Journal of Comparative Neurology*, 493(4):538–53.

[Bellavance et al., 2010] Bellavance, M.-A., Demers, M., and Deschênes, M. (2010). Feedforward inhibition determines the angular tuning of vibrissal responses in the principal trigeminal nucleus. *The Journal of Neuroscience*, 30(3):1057–63.

[Belmonte and Viana, 2008] Belmonte, C. and Viana, F. (2008). Molecular and cellular limits to somatosensory specificity. *Molecular Pain*, 4(1):14.

[Birdwell et al., 2007] Birdwell, J., Solomon, J. H., Thajchayapong, M., Taylor, M., Cheely, M., Towal, R., Conradt, J., and Hartmann, M. J. (2007). Biomechanical models for radial distance determination by the rat vibrissal system. *The Journal of Neurophysiology*, 98(4):2439.

[Bishop, 2000] Bishop, K. M. (2000). Regulation of Area Identity in the Mammalian Neocortex by Emx2 and Pax6. *Science*, 288(5464):344–349.

[Bohland et al., 2009] Bohland, J. W., Bokil, H., Allen, C. B., and Mitra, P. (2009). The brain atlas concordance problem: quantitative comparison of anatomical parcellations. *PloS One*, 4(9):e7200.

[Bohland et al., 2010] Bohland, J. W., Bokil, H., Pathak, S. D., Lee, C.-K., Ng, L., Lau, C., Kuan, C., Hawrylycz, M., and Mitra, P. P. (2010). Clustering of spatial gene expression patterns in the mouse brain and comparison with classical neuroanatomy. *Methods*, 50(2):105–12.

[Bota et al., 2005] Bota, M., Dong, H.-w., and Swanson, L. W. (2005). Brain Architecture Management System. *Neuroinformatics*, 3(1):15–47.

[Breer, 2003] Breer, H. (2003). Sense of smell: recognition and transduction of olfactory signals. *Biochemical Society Transactions*, 31(Pt 1):113–6.

[Bregmann, 1892] Bregmann, E. (1892). Über experimentelle aufsteigende degeneration motorischer und sensibler hirnnerven. *Arb. Neurol. Inst. (Inst. Anat. Physiol. Zentnerv.) Univ.*

[Briggman et al., 2011] Briggman, K. L., Helmstaedter, M., and Denk, W. (2011). Wiring specificity in the direction-selectivity circuit of the retina. *Nature*, 471(7337):183–188.

[Brunet et al., 2007] Brunet, I., Di Nardo, A. a., Sonnier, L., Beurdeley, M., and Prochiantz, A. (2007). The topological role of homeoproteins in the developing central nervous system. *Trends in Neurosciences*, 30(6):260–7.

[Burger et al., 2004] Burger, C., Gorbatyuk, O. S., Velardo, M. J., Peden, C. S., Williams, P., Zolotukhin, S., Reier, P. J., Mandel, R. J., and Muzyczka, N. (2004). Recombinant AAV viral vectors pseudotyped with viral capsids from serotypes 1, 2, and 5 display differential efficiency and cell tropism after delivery to different regions of the central nervous system. *Molecular Therapy*, 10(2):302–17.

[Burns and Baylor, 2001] Burns, M. E. and Baylor, D. a. (2001). Activation, deactivation, and adaptation in vertebrate photoreceptor cells. *Annual Review of Neuroscience*, 24:779–805.

[Carson et al., 2010] Carson, J., Ju, T., Bello, M., Thaller, C., Warren, J., Kakadiaris, I. a., Chiu, W., and Eichele, G. (2010). Automated pipeline for atlas-based annotation of gene expression patterns: application to postnatal day 7 mouse brain. *Methods*, 50(2):85–95.

[Carson et al., 2005] Carson, J. P., Ju, T., Lu, H.-C., Thaller, C., Xu, M., Pallas, S. L., Crair, M. C., Warren, J., Chiu, W., and Eichele, G. (2005). A digital atlas to characterize the mouse brain transcriptome. *PLoS Computational Biology*, 1(4):e41.

[Chédotal and Richards, 2010] Chédotal, A. and Richards, L. J. (2010). Wiring the brain: the biology of neuronal guidance. *Cold Spring Harbor Perspectives in Biology*, 2(6):a001917.

[Christiansen et al., 2006] Christiansen, J. H., Yang, Y., Venkataraman, S., Richardson, L., Stevenson, P., Burton, N., Baldock, R. a., and Davidson, D. R. (2006). EMAGE: a spatial database of gene expression patterns during mouse embryo development. *Nucleic Acids Research*, 34(Database issue):D637–41.

[Committee, 2005] Committee, Mathematical Sciences Research for DOE: Computational Biology, N. R. C. (2005). *Mathematics and 21st Century Biology*. The National Academies Press.

[Courville, 1966] Courville, J. (1966). The nucleus of the facial nerve; the relation between cellular groups and peripheral branches of the nerve. *Brain Research*, 1:338–354.

[Curtis and Kleinfeld, 2009] Curtis, J. C. and Kleinfeld, D. (2009). Phase-to-rate transformations encode touch in cortical neurons of a scanning sensorimotor system. *Nature Neuroscience*, 12(4):492–501.

[Damak et al., 2008] Damak, S., Mosinger, B., and Margolskee, R. F. (2008). Transsynaptic transport of wheat germ agglutinin expressed in a subset of type II taste cells of transgenic mice. *BMC Neuroscience*, 9:96.

[Denk et al., 2012] Denk, W., Briggman, K. L., and Helmstaedter, M. (2012). Structural neurobiology: missing link to a mechanistic understanding of neural computation. *Nature Reviews Neuroscience*, 13(5):351–8.

[Devor et al., 2008] Devor, A., Hillman, E. M. C., Tian, P., Waeber, C., Teng, I. C., Ruvinskaya, L., Shalinsky, M. H., Zhu, H., Haslinger, R. H., Narayanan, S. N., Ulbert, I., Dunn, A. K., Lo, E. H., Rosen, B. R., Dale, A. M., Kleinfeld, D., and Boas, D. a. (2008). Stimulus-induced changes in blood flow and 2-deoxyglucose uptake dissociate in ipsilateral somatosensory cortex. *The Journal of Neuroscience*, 28(53):14347–57.

[Di Caro and Dorigo, 1998] Di Caro, G. and Dorigo, M. (1998). AntNet : Distributed Stigmergetic Control for Communications Networks. *Journal of Artificial Intelligence Research*, 9:317–365.

[Dombeck et al., 2007] Dombeck, D., Khabbaz, A., Collman, F., Adelman, T., and Tank, D. (2007). Imaging Large-Scale Neural Activity with Cellular Resolution in Awake , Mobile Mice. *Neuron*, 56(1):43–57.

[Dong, 2008] Dong, H. (2008). *The Allen Atlas: A Digital Brain Atlas of C57BL/6J Male Mouse*. Wiley, Incorporated.

[Dong et al., 2009] Dong, H.-W., Swanson, L. W., Chen, L., Fanselow, M. S., and Toga, A. W. (2009). Genomic-anatomic evidence for distinct functional domains in hippocampal field CA1. *Proceedings of the National Academy of Sciences of the United States of America*, 106(28):11794–9.

[Drew and Feldman, 2009] Drew, P. J. and Feldman, D. E. (2009). Intrinsic signal imaging of deprivation-induced contraction of whisker representations in rat somatosensory cortex. *Cerebral Cortex*, 19(2):331–48.

[Duda et al., 2001] Duda, R. O., Hart, P. E., and Stork, D. G. (2001). *Pattern Classification*. Wiley-Interscience, 2 edition.

[Duemani Reddy et al., 2008] Duemani Reddy, G., Kelleher, K., Fink, R., and Saggau, P. (2008). Three-dimensional random access multiphoton microscopy for functional imaging of neuronal activity. *Nature Neuroscience*, 11(6):713–20.

[Dumitru, 1995] Dumitru, D. (1995). *Electrodiagnostic medicine*. Hanley and Belfus, Philadelphia, PA.

[Erzurumlu and Killackey, 1979] Erzurumlu, R. and Killackey, H. P. (1979). Efferent connections of the brainstem trigeminal complex with the facial nucleus of the rat. *The Journal of Comparative Neurology*, 188(1):75–86.

[Erzurumlu et al., 2010] Erzurumlu, R., Murakami, Y., and Rijli, F. M. (2010). Mapping the face in the somatosensory brainstem. *Nature Reviews Neuroscience*, 11(4):252–263.

[Falls, 1984] Falls, W. (1984). Termination in trigeminal nucleus oralis of ascending intratrigeminal axons originating from neurons in the medullary dorsal horn: an HRP study in the rat employing light and electron microscopy. *Brain Research*, 290(1):136–140.

[Fay and Norgren, 1997] Fay, R. A. and Norgren, R. (1997). Identification of rat brainstem multisynaptic connections to the oral motor nuclei in the rat using pseudorabies virus. II. Facial muscle motor systems. *Brain Research Reviews*, 25(3):276–90.

[Filipkowski et al., 2001] Filipkowski, R. K., Rydz, M., and Kaczmarek, L. (2001). Expression of c-Fos, Fos B, Jun B, and Zif268 transcription factor proteins in rat barrel cortex following apomorphine-evoked whisking behavior. *Neuroscience*, 106(4):679–88.

[French and Pavlidis, 2011] French, L. and Pavlidis, P. (2011). Relationships between gene expression and brain wiring in the adult rodent brain. *PLoS computational biology*, 7(1):e1001049.

[French et al., 2011] French, L., Tan, P. P. C., and Pavlidis, P. (2011). Large-Scale Analysis of Gene Expression and Connectivity in the Rodent Brain: Insights through Data Integration. *Frontiers in Neuroinformatics*, 5(July):12.

[Freund, 2009] Freund, Y. (2009). A more robust boosting algorithm. *Arxiv Preprint*, arXiv:0905.

[Friedman et al., 2000] Friedman, B. J., Hastie, T., and Tibshirani, R. (2000). Additive logistic regression: A statistical view of boosting. *Annals of Statistics*, 28(2):337–407.

[Fukuda et al., 2003] Fukuda, J., Ishimine, H., and Masaki, Y. (2003). Long-term staining of live Merkel cells with FM dyes. *Cell and tissue research*, 311(3):325–332.

[Furuta et al., 2008] Furuta, T., Timofeeva, E., Nakamura, K., Okamoto-Furuta, K., Togo, M., Kaneko, T., and Deschênes, M. (2008). Inhibitory gating of vibrissal inputs in the brainstem. *The Journal of Neuroscience*, 28(8):1789.

[Ghosh et al., 2000] Ghosh, I., Hamilton, A. D., and Regan, L. (2000). Antiparallel Leucine Zipper-Directed Protein Reassembly : Application to the Green Fluorescent Protein. *Journal of the American Chemical Society*, 122:5658–5659.

[Giannone et al., 2007] Giannone, G., Dubin-Thaler, B. J., Rossier, O., Cai, Y., Chaga, O., Jiang, G., Beaver, W., Döbereiner, H.-G., Freund, Y., Borisy, G., and Sheetz, M. P. (2007). Lamellipodial actin mechanically links myosin activity with adhesion-site formation. *Cell*, 128(3):561–75.

[Gibson, 1962] Gibson, J. J. (1962). Observations on active touch. *Psychological Review*, 69(6):477.

[Gobel et al., 1981] Gobel, S., Hockfield, S., and Ruda, M. (1981). Anatomical similarities between medullary and spinal dorsal horns. In Kawamura, Y. and Dubner, R., editors, *Oral-facial Sensory and Motor Functions*, pages 211–223. Quintessence.

[Göbel and Helmchen, 2007] Göbel, W. and Helmchen, F. (2007). New angles on neuronal dendrites in vivo. *Journal of Neurophysiology*, 98(6):3770–9.

[Göbel et al., 2007] Göbel, W., Kampa, B. M., and Helmchen, F. (2007). Imaging cellular network dynamics in three dimensions using fast 3D laser scanning. *Nature Methods*, 4(1):73–9.

[Golgi, 1873] Golgi, C. (1873). Sulla struttura della sostanza grigia del cervelo. *Gazzetta Medica Italiana*, 33:244–246.

[Golshani et al., 2009] Golshani, P., Gonçalves, J. T., Khoshkhoo, S., Mostany, R., Smirnakis, S., and Portera-Cailliau, C. (2009). Internally mediated developmental desynchronization of neocortical network activity. *The Journal of Neuroscience*, 29(35):10890–9.

[Golub, 1999] Golub, T. R. (1999). Molecular classification of cancer: Class discovery and class prediction by gene expression monitoring. *Science*, 286(5439):531–537.

[Gong et al., 2003] Gong, S., Zheng, C., Doughty, M. L., Losos, K., Didkovsky, N., Schambra, U. B., Nowak, N. J., Joyner, A., Leblanc, G., Hatten, M. E., and Heintz, N. (2003). A gene expression atlas of the central nervous system based on bacterial artificial chromosomes. *Nature*, 425(6961):917–25.

[Gradinaru et al., 2010] Gradinaru, V., Zhang, F., Ramakrishnan, C., Mattis, J., Prakash, R., Diester, I., Goshen, I., Thompson, K. R., and Deisseroth, K. (2010). Molecular and cellular approaches for diversifying and extending optogenetics. *Cell*, 141(1):154–65.

[Grange and Mitra, 2011] Grange, P. and Mitra, P. P. (2011). Marker Genes for Anatomical Regions in the Brain: Insights from the Allen Gene Expression Atlas. *Arxiv Preprint*, page 26.

[Greenberg et al., 2008] Greenberg, D. S., Houweling, A. R., and Kerr, J. N. D. (2008). Population imaging of ongoing neuronal activity in the visual cortex of awake rats. *Nature Neuroscience*, 11(7):749–51.

[Gu et al., 1994] Gu, H., Marth, J. D., Orban, P. C., Mossmann, H., and Rajewsky, K. (1994). Deletion of a DNA Polymerase , 3 Gene Segment in T Cells Using Cell Type-Specific Gene Targeting. *Science*, 265(5168):103–106.

[Hallas and Jacquin, 1990] Hallas, B. H. and Jacquin, M. F. (1990). Structure-function relationships in rat brain stem subnucleus interpolaris. IX. Inputs from subnucleus caudalis. *The Journal of Neurophysiology*, 64(1):28–45.

[Hartmann et al., 2003] Hartmann, M. J., Johnson, N., Towal, R., and Assad, C. (2003). Mechanical characteristics of rat vibrissae: resonant frequencies and damping in isolated whiskers and in the awake behaving animal. *The Journal of Neuroscience*, 23(16):6510.

[Hasegawa et al., 2007] Hasegawa, H., Abbott, S., Han, B., Qi, Y., and Wang, F. (2007). Analyzing somatosensory axon projections with the sensory neuron-specific Advillin gene. *The Journal of Neuroscience*, 27(52):14404.

[Hasegawa and Wang, 2008] Hasegawa, H. and Wang, F. (2008). Visualizing mechanosensory endings of TrkC-expressing neurons in HS3ST-2-hPLAP mice. *The Journal of Comparative Neurology*, 511(4):543–556.

[Hastie et al., 2009] Hastie, T., Tibshirani, R., and Friedman, J. (2009). *The elements of statistical learning: data mining, inference and prediction*. Springer, 2 edition.

[Hattox et al., 2002] Hattox, A., Priest, C., and Keller, A. (2002). Functional circuitry involved in the regulation of whisker movements. *The Journal of Comparative Neurology*, 442(3):266–276.

[Hawrylycz et al., 2011] Hawrylycz, M. J., Baldock, R. A., Burger, A., Hashikawa, T., Johnson, G. A., Martone, M. E., Ng, L. L., Lau, C., Larson, S. D., Nissanov, J., and Puelles, L. (2011). Digital Atlasing and Standardization in the Mouse Brain. *PLoS Computational Biology*, 7(2):2–7.

[Hayashi, 1980] Hayashi, H. (1980). Distributions of vibrissae afferent fiber collaterals in the trigeminal nuclei as revealed by intra-axonal injection of horseradish peroxidase. *Brain Research*, 183:442–446.

[Hayashi, 1985a] Hayashi, H. (1985a). Morphology of central terminations of intra-axonally stained, large, myelinated primary afferent fibers from facial skin in the rat. *The Journal of Comparative Neurology*, 215:195–215.

[Hayashi, 1985b] Hayashi, H. (1985b). Morphology of terminations of small and large myelinated trigeminal primary afferent fibers in the cat. *The Journal of Comparative Neurology*, 240(1):71–89.

[Heim et al., 2007] Heim, N., Garaschuk, O., Friedrich, M., Mank, M., Milos, R., Kovalchuk, Y., Konnerth, A., and Griesbeck, O. (2007). Improved calcium imaging in transgenic mice expressing a troponin CâĂŞbased biosensor. *Nature Methods*, 4(2):127–129.

[Heim and Griesbeck, 2004] Heim, N. and Griesbeck, O. (2004). Genetically encoded indicators of cellular calcium dynamics based on troponin C and green fluorescent protein. *The Journal of Biological Chemistry*, 279(14):14280–6.

[Hemert and Baldock, 2007] Hemert, J. V. and Baldock, R. (2007). Mining spatial gene expression data for association rules. In Hochreiter, S. and Wagner, R., editors, *Bioinformatics Research and Development*, pages 66–76. Springer-Verlag.

[Higo et al., 1999] Higo, N., Oishi, T., Yamashita, A., Matsuda, K., and Hayashi, M. (1999). Quantitative non-radioactive in situ hybridization study of GAP-43 and SCG10 mRNAs in the Cerebral Cortex of Adult and Infant Macaque Monkeys. *Cerebral Cortex*, 9:317–331.

[Hill et al., 2008] Hill, D., Bermejo, R., Zeigler, H. P., and Kleinfeld, D. (2008). Biomechanics of the vibrissa motor plant in rat: rhythmic whisking consists of triphasic neuromuscular activity. *The Journal of Neuroscience*, 28(13):3438.

[Hirai et al., 2005] Hirai, H., Pang, Z., Bao, D., Miyazaki, T., Li, L., Miura, E., Parris, J., Rong, Y., Watanabe, M., Yuzaki, M., and Morgan, J. I. (2005). Cbln1 is essential for synaptic integrity and plasticity in the cerebellum. *Nature Neuroscience*, 8(11):1534–41.

[Hodge et al., 2007] Hodge, L., Klassen, M., Han, B., Yiu, G., Hurrell, J., Howell, A., Rousseau, G., Lemaigre, F., Tessier-Lavigne, M., and Wang, F. (2007). Retrograde BMP signaling regulates trigeminal sensory neuron identities and the formation of precise face maps. *Neuron*, 55(4):572–586.

[Hollis et al., 2008] Hollis, E. R., Kadoya, K., Hirsch, M., Samulski, R. J., and Tuszynski, M. H. (2008). Efficient retrograde neuronal transduction utilizing self-complementary AAV1. *Molecular Therapy*, 16(2):296–301.

[Holstege et al., 1986] Holstege, G., van Ham, J. J., and Tan, J. (1986). Afferent projections to the orbicularis oculi motoneuronal cell group. An autoradiographical tracing study in the cat. *Brain Research*, 374(2):306–20.

[Hougaard et al., 1997] Hougaard, D. M., Hansen, H., and Larsson, L.-I. (1997). Non-radioactive in situ hybridization for mRNA with emphasis on the use of oligodeoxynucleotide probes. *Histochemistry and Cell Biology*, 108:335–344.

[Iggo and Ogawa, 1977] Iggo, B. A. and Ogawa, H. (1977). Correlative physiological and morphological studies of rapidly adapting mechanoreceptors in cat's glabrous skin. *Journal of Physiology*, 266:275–296.

[Inan and Crair, 2007] Inan, M. and Crair, M. C. (2007). Development of cortical maps: perspectives from the barrel cortex. *The Neuroscientist*, 13(1):49–61.

[Isokawa-Akesson and Komisaruk, 1987] Isokawa-Akesson, M. and Komisaruk, B. (1987). Difference in projections to the lateral and medial facial nucleus: anatomically separate pathways for rhythmical vibrissa movement in rats. *Experimental Brain Research*, 65(2):385–398.

[Jacquin et al., 1989] Jacquin, M. F., Barcia, M., and Rhoades, R. W. (1989). Structure-function relationships in rat brainstem subnucleus interpolaris: IV. Projection neurons. *The Journal of Comparative Neurology*, 282(1):45–62.

[Jacquin et al., 1984] Jacquin, M. F., Mooney, R., and Rhoades, R. W. (1984). Axon arbors of functionally distinct whisker afferents are similar in medullary dorsal horn. *Brain Research*, 298(1):175–180.

[Jones et al., 2009] Jones, A. R., Overly, C. C., and Sunkin, S. M. (2009). The Allen Brain Atlas: 5 years and beyond. *Nature Reviews Neuroscience*, 10(11):821–828.

[Jones et al., 2004] Jones, L., Depireux, D., Simons, D. J., and Keller, A. (2004). Robust temporal coding in the trigeminal system. *Science*, 304(5679):1986.

[Ju et al., 2006] Ju, T., Warren, J., Carson, J., Bello, M., Kakadiaris, I., Chiu, W., Thaller, C., and Eichele, G. (2006). 3D volume reconstruction of a mouse brain from histological sections using warp filtering. *Journal of Neuroscience Methods*, 156(1-2):84–100.

[Kasthuri and Lichtman, 2007] Kasthuri, N. and Lichtman, J. W. (2007). The rise of the 'projectome'. *Nature Methods*, 4(4):307–8.

[Kerr, 1963] Kerr, F. W. (1963). The divisional organization of afferent fibres of the trigeminal nerve. *Brain*, 86(4):721.

[Kerr, 1970] Kerr, F. W. (1970). The fine structure of the subnucleus caudalis of the trigeminal nerve. *Brain Research*, 23(2):129–145.

[Kerr et al., 2007] Kerr, J., De Kock, C., Greenberg, D., Bruno, R., Sakmann, B., and Helmchen, F. (2007). Spatial organization of neuronal population responses in layer 2/3 of rat barrel cortex. *The Journal of Neuroscience*, 27(48):13316.

[Kerr et al., 2005] Kerr, J. N. D., Greenberg, D., and Helmchen, F. (2005). Imaging input and output of neocortical networks in vivo. *Proceedings of the National Academy of Sciences of the United States of America*, 102(39):14063–8.

[Khatri et al., 2009] Khatri, V., Bermejo, R., Brumberg, J., Keller, A., and Zeigler, H. P. (2009). Whisking in air: encoding of kinematics by trigeminal ganglion neurons in awake rats. *The Journal of Neurophysiology*, 101(4):1836.

[Kim et al., 2011] Kim, J.-N., Koh, K.-S., Lee, E., Park, S.-C., and Song, W.-C. (2011). The morphology of the rat vibrissal follicle-sinus complex revealed by three-dimensional computer-aided reconstruction. *Cells, tissues, organs*, 193(3):207–14.

[Kingsford and Salzberg, 2008] Kingsford, C. and Salzberg, S. L. (2008). What are decision trees? *Nature Biotechnology*, 26(9):1011–3.

[Kinoshita et al., 2002] Kinoshita, N., Mizuno, T., and Yoshihara, Y. (2002). Adenovirus-mediated WGA gene delivery for transsynaptic labeling of mouse olfactory pathways. *Chemical Senses*, 27(3):215–23.

[Klein et al., 1988] Klein, B., Renehan, W. E., Jacquin, M. F., and Rhoades, R. W. (1988). Anatomical consequences of neonatal infraorbital nerve transection upon the trigeminal ganglion and vibrissa follicle nerves in the adult rat. *The Journal of Comparative Neurology*, 268(4):469–488.

[Klein and Rhoades, 1985] Klein, B. G. and Rhoades, R. W. (1985). Representation of whisker follicle intrinsic musculature in the facial motor nucleus of the rat. *The Journal of Comparative Neurology*, 232:55–69.

[Kleinfeld et al., 2006] Kleinfeld, D., Ahissar, E., and Diamond, M. E. (2006). Active sensation: insights from the rodent vibrissa sensorimotor system. *Current Opinion in Neurobiology*, 16(4):435–444.

[Kleinfeld et al., 1999] Kleinfeld, D., Berg, R. W., and O'Connor, S. M. (1999). Anatomical loops and their electrical dynamics in relation to whisking by rat. *Somatosensory & Motor Research*, 16(2):69–88.

[Kleinfeld and Delaney, 1996] Kleinfeld, D. and Delaney, K. R. (1996). Distributed representation of vibrissa movement in the upper layers of somatosensory cortex revealed with voltage-sensitive dyes. *The Journal of Comparative Neurology*, 375(1):89–108.

[Kleinfeld et al., 1998] Kleinfeld, D., Mitra, P. P., Helmchen, F., and Denk, W. (1998). Fluctuations and stimulus-induced changes in blood flow observed in individual capillaries in layers 2 through 4 of rat neocortex. *Proceedings of the National Academy of Sciences of the United States of America*, 95(26):15741–6.

[Komiyama et al., 1984] Komiyama, M., Shibata, H., and Suzuki, T. (1984). Somatotopic representation of facial muscles within the facial nucleus of the mouse. *Brain, Behavior and Evolution*, pages 144–151.

[Komiyama et al., 2010] Komiyama, T., Sato, T. R., O'Connor, D. H., Zhang, Y.-X., Huber, D., Hooks, B. M., Gabitto, M., and Svoboda, K. (2010). Learning-related fine-scale specificity imaged in motor cortex circuits of behaving mice. *Nature*, 464(7292):1182–6.

[Krupa et al., 2001] Krupa, D., Brisben, A., and Nicolelis, M. A. (2001). A multichannel whisker stimulator for producing spatiotemporally complex tactile stimuli. *The Journal of Neuroscience Methods*, 104(2):199–208.

[Lavallée et al., 2005] Lavallée, P., Urbain, N., Dufresne, C., Bokor, H., Acsády, L., and Deschênes, M. (2005). Feedforward inhibitory control of sensory information in higher-order thalamic nuclei. *The Journal of Neuroscience*, 25(33):7489–7498.

[Lazarov, 2002] Lazarov, N. (2002). Comparative analysis of the chemical neuroanatomy of the mammalian trigeminal ganglion and mesencephalic trigeminal nucleus. *Progress in Neurobiology*, 66(1):19–59.

[LeChasseur et al., 2011] LeChasseur, Y., Dufour, S., Lavertu, G., Bories, C., Deschênes, M., Vallée, R., and De Koninck, Y. (2011). A microprobe for parallel optical and electrical recordings from single neurons in vivo. *Nature Methods*, 8(4):319–25.

[Lee et al., 2008] Lee, C.-K., Sunkin, S. M., Kuan, C., Thompson, C. L., Pathak, S., Ng, L. L., Lau, C., Fischer, S., Mortrud, M., Slaughterbeck, C., Jones, A. R., Lein, E. S., and Hawrylycz, M. J. (2008). Quantitative methods for genome-scale analysis of in situ hybridization and correlation with microarray data. *Genome biology*, 9(1):R23.

[Lee and Seung, 1999] Lee, D. and Seung, H. (1999). Learning the parts of objects by non-negative matrix factorization. *Nature*, 401(6755):788–791.

[Lei et al., 2008] Lei, M., Xu, H., Yang, H., and Yao, B. (2008). Femtosecond laser-assisted microinjection into living neurons. *The Journal of Neuroscience Methods*, 174(2):215–218.

[Lein et al., 2007] Lein, E. S., Hawrylycz, M. J., Ao, N., Ayres, M., Bensinger, A., Bernard, A., Boe, A. F., Boguski, M. S., Brockway, K. S., Byrnes, E. J., Chen, L., Chen, L., Chen, T.-M., Chin, M. C., Chong, J., Crook, B. E., Czaplinska, A., Dang, C. N., Datta, S., Dee, N. R., Desaki, A. L., Desta, T., Diep, E., Dolbeare, T. A., Donelan, M. J., Dong, H.-W., Dougherty, J. G., Duncan, B. J., Ebbert, A. J., Eichele, G., Estin, L. K., Faber, C., Facer, B. A., Fields, R., Fischer, S. R., Fliss, T. P., Frensley, C., Gates, S. N., Glattfelder, K. J., Halverson, K. R., Hart, M. R., Hohmann, J. G., Howell, M. P., Jeung, D. P., Johnson, R. A., Karr, P. T., Kawal, R., Kidney, J. M., Knapik, R. H., Kuan, C. L., Lake, J. H., Laramee, A. R., Larsen, K. D., Lau, C., Lemon, T. A., Liang, A. J., Liu, Y., Luong, L. T., Michaels, J., Morgan, J. J., Morgan, R. J., Mortrud, M. T., Mosqueda, N. F., Ng, L. L., Ng, R., Orta, G. J., Overly, C. C., Pak, T. H., Parry, S. E., Pathak, S. D., Pearson, O. C., Puchalski, R. B., Riley, Z. L., Rockett, H. R., Rowland, S. A., Royall, J. J., Ruiz, M. J., Sarno, N. R., Schaffnit, K., Shapovalova, N. V., Sivisay, T., Slaughterbeck, C. R., Smith, S. C., Smith, K. A., Smith, B. I., Sodt, A. J., Stewart, N. N., Stumpf, K.-R., Sunkin, S. M., Sutram, M., Tam, A., Teemer, C. D., Thaller, C., Thompson, C. L., Varnam, L. R., Visel, A., Whitlock, R. M., Wohnoutka, P. E., Wolkey, C. K., Wong, V. Y., Wood, M., Yaylaoglu, M. B., Young, R. C., Youngstrom, B. L., Yuan, X. F., Zhang, B., Zwingman, T. A., and Jones, A. R. (2007). Genome-wide atlas of gene expression in the adult mouse brain. *Nature*, 445(7124):168–76.

[Leiser and Moxon, 2007] Leiser, S. and Moxon, K. (2007). Responses of trigeminal ganglion neurons during natural whisking behaviors in the awake rat. *Neuron*, 53(1):117–133.

[Li et al., 1997] Li, Y. Q., Takada, M., Kaneko, T., and Mizuno, N. (1997). Distribution of GABAergic and glycinergic premotor neurons projecting to the facial and hypoglossal nuclei in the rat. *The Journal of Comparative Neurology*, 378(2):283–94.

[Lichtenstein et al., 1990] Lichtenstein, S., Carvell, G., and Simons, D. J. (1990). Responses of rat trigeminal ganglion neurons to movements of vibrissae in different directions. *Somatosensory & Motor Research*, 7(1):47–65.

[Lichtman and Sanes, 2008] Lichtman, J. W. and Sanes, J. R. (2008). Ome sweet ome: what can the genome tell us about the connectome? *Current Opinion in Neurobiology*, 18(3):346–53.

[Lillis et al., 2008] Lillis, K. P., Eng, A., White, J. a., and Mertz, J. (2008). Two-photon imaging of spatially extended neuronal network dynamics with high temporal resolution. *Journal of Neuroscience Methods*, 172(2):178–84.

[Lin et al., 2009] Lin, L., Lesnick, T. G., Maraganore, D. M., and Isacson, O. (2009). Axon guidance and synaptic maintenance: preclinical markers for neurodegenerative disease and therapeutics. *Trends in Neurosciences*, 32(3):142–9.

[Liu et al., 2008] Liu, T., Li, G., Nie, J., Tarokh, A., Zhou, X., Guo, L., Malicki, J., Xia, W., and Wong, S. T. C. (2008). An automated method for cell detection in zebrafish. *Neuroinformatics*, 6(1):5–21.

[Lo et al., 1999] Lo, F. S., Guido, W., and Erzurumlu, R. S. (1999). Electrophysiological properties and synaptic responses of cells in the trigeminal principal sensory nucleus of postnatal rats. *Journal of Neurophysiology*, 82(5):2765–75.

[López et al., 2010] López, I. P., Salin, P., Kachidian, P., Barroso-Chinea, P., Rico, A. J., Gómez-Bautista, V., Conte-Perales, L., Coulon, P., Goff, L. K.-L., and Lanciego, J. L. (2010). The added value of rabies virus as a retrograde tracer when combined with dual anterograde tract-tracing. *The Journal of Neuroscience Methods*, 194(1):21–7.

[Lumpkin and Caterina, 2007] Lumpkin, E. A. and Caterina, M. (2007). Mechanisms of sensory transduction in the skin. *Nature*, 445(7130):858–865.

[Luo et al., 2009] Luo, W., Enomoto, H., Rice, F. L., Milbrandt, J., and Ginty, D. (2009). Molecular identification of rapidly adapting mechanoreceptors and their developmental dependence on ret signaling. *Neuron*, 64(6):841–856.

[Ma, 1991] Ma, P. (1991). The barrelettesâĂŤarchitectonic vibrissal representations in the brainstem trigeminal complex of the mouse. Normal structural organization. *The Journal of Comparative Neurology*, 309(2):161–199.

[MacKenzie-Graham et al., 2004] MacKenzie-Graham, A., Lee, E.-F., Dinov, I. D., Bota, M., Shattuck, D. W., Ruffins, S., Yuan, H., Konstantinidis, F., Pitiot, A., Ding, Y., Hu, G., Jacobs, R. E., and Toga, A. W. (2004). A multimodal, multidimensional atlas of the C57BL/6J mouse brain. *Journal of Anatomy*, 204(2):93–102.

[Mallamaci et al., 2000] Mallamaci, A., Muzio, L., Chan, C.-h., Parnavelas, J., and Boncinelli, E. (2000). Area identity shifts in the early cerebral cortex of Emx2 -/- mutant mice. *Nature Neuroscience*, 3(7):679–686.

[Mank et al., 2008] Mank, M., Santos, A., Direnberger, S., Mrsic-Flogel, T., Hofer, S., Stein, V., Hendel, T., Reiff, D., Levelt, C., Borst, A., and Others (2008). A genetically encoded calcium indicator for chronic in vivo two-photon imaging. *Nature Methods*, 5(9):805–811.

[Marfurt, 1981] Marfurt, C. (1981). The central projections of trigeminal primary afferent neurons in the cat as determined by the tranganglionic transport of horseradish peroxidase. *The Journal of Comparative Neurology*, 203(4):785–798.

[Masino et al., 1993] Masino, S. a., Kwon, M. C., Dory, Y., and Frostig, R. D. (1993). Characterization of functional organization within rat barrel cortex using intrinsic signal optical imaging through a thinned skull. *Proceedings of the National Academy of Sciences of the United States of America*, 90(21):9998–10002.

[Mason et al., 2010] Mason, M. R. J., Ehlert, E. M. E., Eggers, R., Pool, C. W., Hermening, S., Huseinovic, A., Timmermans, E., Blits, B., and Verhaagen, J. (2010). Comparison of AAV serotypes for gene delivery to dorsal root ganglion neurons. *Molecular Therapy*, 18(4):715–24.

[Merkel, 1875] Merkel, F. (1875). Tastzellen und Tastkörperchen bei den Hausthieren und beim Menschen. *Archiv für Mikroskopische Anatomie*, 11:636–652.

[Metzger et al., 1995] Metzger, D., Clifford, J., Chiba, H., and Chambon, P. (1995). Conditional site-speciic recombination in mammalian cells using a ligand-dependent chimeric Cre recombinase. *Proceedings of the National Academy of Sciences of the United States of America*, 92(July):6991–6995.

[Meyers et al., 2003] Meyers, J., MacDonald, R., Duggan, A., Lenzi, D., Standaert, D., Corwin, J., and Corey, D. (2003). Lighting up the senses: FM1-43 loading of sensory cells through nonselective ion channels. *The Journal of Neuroscience*, 23(10):4054.

[Minnery and Simons, 2003] Minnery, B. and Simons, D. J. (2003). Response properties of whisker-associated trigeminothalamic neurons in rat nucleus principalis. *The Journal of Neurophysiol*, 89(1):40.

[Mitchinson et al., 2004] Mitchinson, B., Gurney, K. N., Redgrave, P., Melhuish, C., Pipe, A. G., Pearson, M., Gilhespy, I., and Prescott, T. J. (2004). Empirically inspired simulated electro-mechanical model of the rat mystacial follicle-sinus complex. *Proceedings of the Royal Society B: Biological Sciences*, 271(1556):2509–16.

[Mukamel et al., 2009] Mukamel, E. a., Nimmerjahn, A., and Schnitzer, M. J. (2009). Automated analysis of cellular signals from large-scale calcium imaging data. *Neuron*, 63(6):747–60.

[Müller and Mestres, 2002] Müller, M. and Mestres, P. (2002). Vagal innervation of the rat intestinal apparatus. A new quantitative approach on the basis of the tracer-fluorescence-intensity. *European Journal of Anatomy*, 6(2):83–94.

[Munger and Rice, 1986] Munger, B. L. and Rice, F. L. (1986). Successive waves of differentiation of cutaneous afferents in rat mystacial skin. *The Journal of Comparative Neurology*, 414:404–414.

[Neimark et al., 2003] Neimark, M., Andermann, M., Hopfield, J., and Moore, C. (2003). Vibrissa resonance as a transduction mechanism for tactile encoding. *The Journal of Neuroscience*, 23(16):6499.

[Ng et al., 2007] Ng, L. L., Pathak, S. D., Kuan, C., Lau, C., Dong, H.-W., Sodt, A., Dang, C., Avants, B., Yushkevich, P., Gee, J. C., Haynor, D., Lein, E. S., Jones, A. R., and Hawrylycz, M. J. (2007). Neuroinformatics for genome-wide 3D gene expression mapping in the mouse brain. *IEEE/ACM Transactions on Computational Biology and Bioinformatics*, 4(3):382–93.

[Nguyen et al., 2009] Nguyen, Q.-T., Dolnick, E., Driscoll, J., and Kleinfeld, D. (2009). Mpscope 2.0: A computer system for two-photon laser scanning microscopy with concurrent plasma-mediated ablation and electrophysiology. In Frostig, R., editor, *Methods for In Vivo Optical Imaging*, pages 117–42. CRC Press, 2 edition.

[Nguyen and Kleinfeld, 2005] Nguyen, Q.-t. and Kleinfeld, D. (2005). Positive feedback in a brainstem tactile sensorimotor loop. *Neuron*, 45(3):447–457.

[Nguyen et al., 2006] Nguyen, Q.-t., Tsai, P. S., and Kleinfeld, D. (2006). MPScope: a versatile software suite for multiphoton microscopy. *The Journal of Neuroscience Methods*, 156(1-2):351–359.

[Nicolelis et al., 1995] Nicolelis, M. A., Baccala, L., Lin, R., and Chapin, J. (1995). Sensorimotor encoding by synchronous neural ensemble activity at multiple levels of the somatosensory system. *Science*, 268(5215):1353.

[Nikolenko et al., 2007] Nikolenko, V., Poskanzer, K. E., and Yuste, R. (2007). Two-photon photostimulation and imaging of neural circuits. *Nature Methods*, 4(11):943–50.

[Nimmerjahn et al., 2004] Nimmerjahn, A., Kirchhoff, F., Kerr, J. N. D., and Helmchen, F. (2004). Sulforhodamine 101 as a specific marker of astroglia in the neocortex in vivo. *Nature Methods*, 1(1):31–7.

[Ohki et al., 2005] Ohki, K., Chung, S., Ch'ng, Y. H., Kara, P., and Reid, R. C. (2005). Functional imaging with cellular resolution reveals precise micro-architecture in visual cortex. *Nature*, 433(7026):597–603.

[Olszewski, 1950] Olszewski, J. (1950). On the anatomical and functional organization of the spinal trigeminal nucleus. *The Journal of Comparative Neurology*, 92(3):401–413.

[Orban et al., 1992] Orban, P. C., Chui, D., and Marth, J. D. (1992). Tissue- and site-specific DNA recombination in transgenic mice. *Proceedings of the National Academy of Sciences of the United States of America*, 89(August):6861–6865.

[Ozden et al., 2008] Ozden, I., Lee, H. M., Sullivan, M. R., and Wang, S. S.-H. (2008). Identification and clustering of event patterns from in vivo multiphoton optical recordings of neuronal ensembles. *Journal of Neurophysiology*, 100(1):495–503.

[Panneton and Martin, 1983] Panneton, W. M. and Martin, G. F. (1983). Brainstem projections to the facial nucleus of the opossum. A study using axonal transport techniques. *Brain Research*, 267(1):19–33.

[Patrizi and Munger, 1966] Patrizi, G. and Munger, B. (1966). The ultrastructure and innervation of rat vibrissae. *The Journal of Comparative Neurology*, 126(3):423–435.

[Pellegrini et al., 1995] Pellegrini, J. J., Horn, A. K. E., and Evinger, C. (1995). The trigeminally evoked blink reflex: I. Neuronal circuits. *Experimental Brain Research*, 107:166–180.

[Polleux et al., 2007] Polleux, F., Ince-Dunn, G., and Ghosh, A. (2007). Transcriptional regulation of vertebrate axon guidance and synapse formation. *Nature Reviews Neuroscience*, 8(5):331–40.

[Potvin, 1996] Potvin, J.-Y. (1996). Genetic Algorithms for the traveling salesman problem. *Annals of Operations Research*, 63:337–370.

[Powers, 1973] Powers, W. T. (1973). Feedback: beyond behaviorism. *Science*, 179(4071):351–6.

[Price et al., 2012] Price, D. J., Clegg, J., Duocastella, X. O., Willshaw, D., and Pratt, T. (2012). The importance of combinatorial gene expression in early Mammalian thalamic patterning and thalamocortical axonal guidance. *Frontiers in Neuroscience*, 6(March):37.

[Ramon y Cajal, 1905] Ramon y Cajal, S. (1905). Chapter XXXI: The trigeminal or Vth cranial nerve. In *Histology of the Nervous System of Man and Vertebrates*, pages 704–729. Oxford University Press.

[Ratzlaff and Grinvald, 1991] Ratzlaff, E. H. and Grinvald, A. (1991). A tandem-lens epifluorescence macroscope: hundred-fold brightness advantage for wide-field imaging. *Journal of Neuroscience Methods*, 36(2-3):127–37.

[Rau et al., 2006] Rau, K., Quinto-Su, P., Hellman, A., and Venugopalan, V. (2006). Pulsed laser microbeam-induced cell lysis: time-resolved imaging and analysis of hydrodynamic effects. *Biophysical journal*, 91(1):317–329.

[Ressler et al., 2002] Ressler, K. J., Paschall, G., Zhou, X.-l., and Davis, M. (2002). Regulation of Synaptic Plasticity Genes during Consolidation of Fear Conditioning. *The Journal of Neuroscience*, 22(18):7892–7902.

[Rice, 1993] Rice, F. L. (1993). Structure, vascularization, and innervation of the mystacial pad of the rat as revealed by the lectin Griffonia simplicifolia. *The Journal of Comparative Neurology*, 337(3):386–399.

[Rice et al., 1997] Rice, F. L., Fundin, B., Arvidsson, J., Aldskogius, H. k., and Johansson, O. (1997). Comprehensive immunofluorescence and lectin binding analysis of vibrissal follicle sinus complex innervation in the mystacial pad of the rat. *The Journal of Comparative Neurology*, 385(2):149–184.

[Rice et al., 1993] Rice, F. L., Kinnman, E., Aldskogius, H., Johansson, O., and Arvidsson, J. (1993). The innervation of the mystacial pad of the rat as revealed by PGP 9.5 immunofluorescence. *The Journal of Comparative Neurology*, 337(3):366–385.

[Rice et al., 1986] Rice, F. L., Mance, A., and Munger, B. (1986). A comparative light microscopic analysis of the sensory innervation of the mystacial pad. I. Innervation of vibrissal follicle-sinus complexes. *The Journal of Comparative Neurology*, 252(2):154–174.

[Richardson et al., 2010] Richardson, L., Venkataraman, S., Stevenson, P., Yang, Y., Burton, N., Rao, J., Fisher, M., Baldock, R. a., Davidson, D. R., and Christiansen, J. H. (2010). EMAGE mouse embryo spatial gene expression database: 2010 update. *Nucleic Acids Research*, 38(Database issue):D703–9.

[Roberts et al., 1988] Roberts, W. M., Howard, J., and Hudspeth, A. J. (1988). Hair cells: Transduction, tuning, and transmission in the inner ear. *Annual Review of Cell Biology*, 4:63–92.

[Rochefort et al., 2009] Rochefort, N. L., Garaschuk, O., Milos, R.-I., Narushima, M., Marandi, N., Pichler, B., Kovalchuk, Y., and Konnerth, A. (2009). Sparsification of neuronal activity in the visual cortex at eye-opening. *Proceedings of the National Academy of Sciences of the United States of America*, 106(35):15049–54.

[Rosenblatt, 1957] Rosenblatt, F. (1957). The perceptron, a perceiving and recognizing automaton. *Cornell Aeronautical Laboratory Report*.

[Rothschild et al., 2010] Rothschild, G., Nelken, I., and Mizrahi, A. (2010). Functional organization and population dynamics in the mouse primary auditory cortex. *Nature Neuroscience*, 13(3):353–60.

[Sachdev et al., 2003] Sachdev, R. N. S., Berg, R., Champney, G., Kleinfeld, D., and Ebner, F. (2003). Unilateral vibrissa contact: changes in amplitude but not timing of rhythmic whisking. *Somatosensory & Motor Research*, 20(2):163–169.

[Sasaki et al., 2008] Sasaki, T., Takahashi, N., Matsuki, N., and Ikegaya, Y. (2008). Fast and accurate detection of action potentials from somatic calcium fluctuations. *Journal of Neurophysiology*, 100(3):1668–76.

[Schaffer et al., 2006] Schaffer, C. B., Friedman, B., Nishimura, N., Schroeder, L. F., Tsai, P. S., Ebner, F. F., Lyden, P. D., and Kleinfeld, D. (2006). Two-photon imaging of cortical surface microvessels reveals a robust redistribution in blood flow after vascular occlusion. *PLoS Biology*, 4(2):e22.

[Schapire et al., 1998] Schapire, R. E., Freund, Y., Bartlett, P., and Lee, W. S. (1998). Boosting the margin: a new explanation for the effectiveness of voting methods. *The Annals of Statistics*, 26(5):1651–1686.

[Schicatano et al., 1997] Schicatano, E. J., Basso, M. A., and Evinger, C. (1997). Animal Model Explains the Origins of the Cranial Dystonia Benign Essential Blepharospasm. *The Journal of Neurophysiology*, 77:2842–2846.

[Schinkel et al., 2008] Schinkel, H., Jacobs, P., Schillberg, S., and Wehner, M. (2008). Infrared picosecond laser for perforation of single plant cells. *Biotechnology and bioengineering*, 99(1):244–248.

[Schmued and Fallon, 1986] Schmued, L. C. and Fallon, J. H. (1986). Fluoro-Gold : a new fluorescent retrograde axonal tracer with numerous unique properties. *Brain Research*, 377:147–154.

[Schroeder et al., 2010] Schroeder, C., Wilson, D., Radman, T., Scharfman, H., and Lakatos, P. (2010). Dynamics of active sensing and perceptual selection. *Current Opinion in Neurobiology*, 20(2):172–176.

[Shatz and Christensen, 2008] Shatz, L. and Christensen, C. (2008). The frequency response of rat vibrissae to sound. *The Journal of the Acoustical Society of America*, 123:2918.

[Shih et al., 2009] Shih, A. Y., Friedman, B., Drew, P. J., Tsai, P. S., Lyden, P. D., and Kleinfeld, D. (2009). Active dilation of penetrating arterioles restores red blood cell flux to penumbral neocortex after focal stroke. *Journal of Cerebral Blood Flow & Metabolism*, 29(4):738–51.

[Shimogori et al., 2004] Shimogori, T., Banuchi, V., Ng, H. Y., Strauss, J. B., and Grove, E. a. (2004). Embryonic signaling centers expressing BMP, WNT and FGF proteins interact to pattern the cerebral cortex. *Development*, 131(22):5639–47.

[Shortland et al., 1995] Shortland, P. J., Demaro, J. A., and Jacquin, M. F. (1995). Trigeminal Structure-Function Relationships: A Reevaluation Based on Long-Range Staining of a Large Sample of Brainstem AP Fibers. *Somatosensory & Motor Research*, 12(3-4):249–275.

[Shuler et al., 2002] Shuler, M. G., Krupa, D. J., and Nicolelis, M. a. L. (2002). Integration of bilateral whisker stimuli in rats: role of the whisker barrel cortices. *Cerebral Cortex*, 12(1):86–97.

[Sigler et al., 2009] Sigler, A., Mohajerani, M. H., and Murphy, T. H. (2009). Imaging rapid redistribution of sensory-evoked depolarization through existing cortical pathways. *Proceedings of the National Academy of Sciences of the United States of America*, 106(28):11759–11764.

[Skinner, 1938] Skinner, B. F. (1938). *The behavior of organisms*. Palleton-Century-Crofts, New York.

[Squire et al., 2008] Squire, L. R., Berg, D., Bloom, F. E., du Lac, S., Ghosh, A., and Spitzer, N. C. (2008). *Fundamental neuroscience*. Elsevier / Academic Press.

[Stepien et al., 2010] Stepien, A. E., Tripodi, M., and Arber, S. (2010). Monosynaptic rabies virus reveals premotor network organization and synaptic specificity of cholinergic partition cells. *Neuron*, 68(3):456–72.

[Stosiek et al., 2003] Stosiek, C., Garaschuk, O., Holthoff, K., and Konnerth, A. (2003). In vivo two-photon calcium imaging of neuronal networks. *Proceedings of the National Academy of Sciences of the United States of America*, 100(12):7319–24.

[Stüttgen et al., 2008] Stüttgen, M., Kullmann, S., and Schwarz, C. (2008). Responses of rat trigeminal ganglion neurons to longitudinal whisker stimulation. *The Journal of Neurophysiology*, 100(4):1879.

[Szwed and Ahissar, 2006] Szwed, M. and Ahissar, E. (2006). Mapping the Gates. Focus on "Relationship Between Physiological Response Type (RA and SA) and Vibrissal Receptive Field of Neurons Within the Rat Trigeminal Ganglion". *The Journal of Neurophysiology*, 95(5):2729.

[Szwed et al., 2003] Szwed, M., Bagdasarian, K., and Ahissar, E. (2003). Encoding of vibrissal active touch. *Neuron*, 40(3):621–630.

[Takeuchi et al., 1979] Takeuchi, Y., Nakano, K., Uemura, M., Matsuda, K., Matsushima, R., and Mizuno, N. (1979). Mesencephalic facial nucleus peroxidase and pontine afferent fiber system to the in the cat : a study using the horseradish and silver impregnation techniques. *Experimental Neurology*, 342:330–342.

[Tamayo et al., 1999] Tamayo, P., Slonim, D., Mesirov, J., Zhu, Q., Kitareewan, S., Dmitrovsky, E., Lander, E. S., and Golub, T. R. (1999). Interpreting patterns of gene expression with self-organizing maps : Methods and application to hematopoietic differentiation. *Proceedings of the National Academy of Sciences of the United States of America*, 96(March):2907–2912.

[Thompson et al., 2008] Thompson, C. L., Pathak, S. D., Jeromin, A., Ng, L. L., MacPherson, C. R., Mortrud, M. T., Cusick, A., Riley, Z. L., Sunkin, S. M., Bernard, A., Puchalski, R. B., Gage, F. H., Jones, A. R., Bajic, V. B., Hawrylycz, M. J., and Lein, E. S. (2008). Genomic anatomy of the hippocampus. *Neuron*, 60(6):1010–21.

[Tibshirani, 1996] Tibshirani, R. (1996). Regression Shrinkage and Selection via the Lasso. *Journal of the Royal Statistical Society. Series B (Methodological)*, 58(1):267–288.

[Torvik, 1956] Torvik, A. (1956). Afferent connections to the sensory trigeminal nuclei, the nucleus of the solitary tract and adjacent structures. An experimental study in the rat. *The Journal of Comparative Neurology*, 106(1):51–141.

[Travers and Norgren, 1983] Travers, J. B. and Norgren, R. (1983). Afferent projections to the oral motor nuclei in the rat. *The Journal of Comparative Neurology*, 220(3):280–98.

[Tsai et al., 2009] Tsai, P. S., Kaufhold, J., Blinder, P., Friedman, B., Drew, P., Karten, H., Lyden, P., and Kleinfeld, D. (2009). Correlations of neuronal and microvascular densities in murine cortex revealed by direct counting and colocalization of nuclei and vessels. *The Journal of Neuroscience*, 29(46):14553.

[Ugolini, 2010] Ugolini, G. (2010). Advances in viral transneuronal tracing. *The Journal of Neuroscience Methods*, 194(1):2–20.

[van Ham and Yeo, 1996] van Ham, J. J. and Yeo, C. H. (1996). Trigeminal inputs to eyeblink motoneurons in the rabbit. *Experimental Neurology*, 142(2):244–57.

[Venkatachalam and Montell, 2007] Venkatachalam, K. and Montell, C. (2007). TRP channels. *Annual Review of Biochemistry*, 76:387–417.

[Visel et al., 2004] Visel, A., Thaller, C., and Eichele, G. (2004). GenePaint.org: an atlas of gene expression patterns in the mouse embryo. *Nucleic Acids Research*, 32(Database issue):D552–6.

[Vogelstein et al., 2010] Vogelstein, J. T., Packer, A. M., Machado, T. a., Sippy, T., Babadi, B., Yuste, R., and Paninski, L. (2010). Fast nonnegative deconvolution for spike train inference from population calcium imaging. *Journal of Neurophysiology*, 104(6):3691–704.

[Vucinić and Sejnowski, 2007] Vucinić, D. and Sejnowski, T. J. (2007). A compact multiphoton 3D imaging system for recording fast neuronal activity. *PloS One*, 2(8):e699.

[Waite and Jacquin, 1992] Waite, P. M. E. and Jacquin, M. F. (1992). Dual innervation of the rat vibrissa: responses of trigeminal ganglion cells projecting through deep or superficial nerves. *The Journal of Comparative Neurology*, 322(2):233–245.

[Wall et al., 2010] Wall, N. R., Wickersham, I. R., Cetin, A., De La Parra, M., and Callaway, E. M. (2010). Monosynaptic circuit tracing in vivo through Cre-dependent targeting and complementation of modified rabies virus. *Proceedings of the National Academy of Sciences of the United States of America*, 107(50):21848–53.

[Wickersham et al., 2007] Wickersham, I. R., Finke, S., Conzelmann, K.-K., and Callaway, E. M. (2007). Retrograde neuronal tracing with a deletion-mutant rabies virus. *Nature Methods*, 4(1):47–9.

[Winkelmann and Breathnach, 1973] Winkelmann, R. and Breathnach, A. (1973). The Merkel cell. *Journal of Investigative Dermatology*, 60(1):2–15.

[Wolf et al., 2011] Wolf, L., Goldberg, C., Manor, N., Sharan, R., and Ruppin, E. (2011). Gene expression in the rodent brain is associated with its regional connectivity. *PLoS Computational Biology*, 7(5):e1002040.

[Wu et al., 2009] Wu, T. T., Chen, Y. F., Hastie, T., Sobel, E., and Lange, K. (2009). Genome-wide association analysis by lasso penalized logistic regression. *Bioinformatics*, 25(6):714–21.

[Yarmolinsky et al., 2009] Yarmolinsky, D., Zuker, C., and Ryba, N. (2009). Common sense about taste: from mammals to insects. *Cell*, 139(2):234–244.

[Yoshihara, 2002] Yoshihara, Y. (2002). Visualizing selective neural pathways with WGA transgene: combination of neuroanatomy with gene technology. *Neuroscience research*, 44(2):133–40.

[Zhang et al., 2004] Zhang, S., Ma, C., and Chalfie, M. (2004). Combinatorial marking of cells and organelles with reconstituted fluorescent proteins. *Cell*, 119:137–44.

[Zou and Hastie, 2005] Zou, H. and Hastie, T. (2005). Regularization and variable selection via the elastic net. *Journal of the Royal Statistical Society: Series B (Statistical Methodology)*, 67(2):301–320.

[Zucker and Welker, 1969] Zucker, E. and Welker, W. (1969). Coding of somatic sensory input by vibrissae neurons in the rat's trigeminal ganglion. *Brain Research*, 12(1):138–156.